Universidad de Concepción
Dirección de Postgrado
Facultad de Ciencias Químicas
Programa Doctorado en Ciencias Geológicas

Evidencia morfo-estratigráfica de los predecesores del terremoto del Maule del 2010, Isla Santa María, centro-sur de Chile.

(Morpho-stratigraphic evidence of the 2010 Maule earthquake predecessors, Isla Santa María, south-central Chile)

Tesis para optar al grado de Doctor en Ciencias Geológicas

DIEGO JOSÉ AEDO ORTIZ
CONCEPCIÓN-CHILE
2024

Profesor Guía: Marco Cisternas Vega
Instituto de Geografía
Pontificia Universidad Católica de Valparaíso

Profesor Co-Guía: Joaquín Cortés Aranda
Dpto. de Ciencias de la Tierra, Facultad de Ciencias Químicas
Universidad de Concepción

AGRADECIMIENTOS

En primer lugar agradezco a Dios y a mi familia sin quienes nada habría sido posible.

A la Universidad de Concepción, al Núcleo Milenio CYCLO "El Ciclo Sísmico a lo largo de las Zonas de Subducción" de la Iniciativa Científica Milenio (ICM) del gobierno chileno y a la Agencia Nacional de Investigación y Desarrollo (ANID) a través del Fondo Nacional de Desarrollo Científico y Tecnológico de Chile 1190258, 1240681 y la beca 21190535, por el apoyo académico, logístico y financiero.

A mi profesor guía Marco Cisternas y a Daniel Melnick cuya experiencia y orientación fueron vitales para la realización de esta tesis y para crecer como profesional y científico. A los profesores del Departamento de Ciencias de la Tierra (Udec), especialmente a Joaquín Cortes por su constante apoyo. A María Esperanza Aravena por su enorme colaboración.

A mis amigos, especialmente Juano, Matías y Pancho, que han sido siempre un pilar en mi crecimiento personal. A mis compañeros de doctorado de la cabina 4, especialmente a Diego, Bladimir, Fernanda, Adrián y Andrés, que me acompañaron y regalaron su valiosa amistad durante estos años de doctorado. A Daniela Uribe y Grupo Centro por su ayuda y su atención.

A mis coautores Patricio Winckler, César Esparza, Dominik Brill, Bladimir Saldaña por sus valiosos comentarios y sugerencias que contribuyeron a la calidad de los artículos publicados. A Jasper Moernaut, Cristian Araya, Matías Carvajal y al equipo del Laboratorio Geotsunami PUCV por sus útiles discusiones durante la preparación de los artículos. A Pedro Matos-Llavona y los revisores de los artículos científicos. También a Bladimir Saldaña, Dominik Brill, Vicente Sepúlveda, Cristian Araya y Diego Cárdenas por ayudarme y participar de las campañas de campo. A la Sra. Ruth, Don Eric y su familia por su hospitalidad y generosidad durante el trabajo en la Isla Santa María.

A todas aquellas personas que de una u otra forma colaboraron en la realización de esta tesis doctoral, de corazón, ¡muchas gracias!

RESUMEN

Comprender el comportamiento sísmico de márgenes de subducción es indispensable para desarrollar modelos probabilísticos que permitan estimar la ocurrencia de futuros eventos. Para esto es necesario contar con registros multi-milenarios que indiquen la recurrencia sísmica en el largo término. En esta tesis se reconstruyó la historia paleosísmica del segmento del Maule a través del análisis de la planicie de cordones litorales arenosos en la Isla Santa María, localizada en el extremo sur del área de ruptura del terremoto del Chile de 2010 (Mw 8.8). Para esto, se analizó la respuesta de la costa de la isla al ciclo sísmico; que produce levantamiento cosísmico y hundimiento intersísmico, monitoreando la principal playa de la isla durante las últimas ocho décadas (entre 1941 a 2021). Las observaciones muestran que la progradación costera y posterior construcción de cordones litorales, fue continua y no respondió sólo al levantamiento cosísmico asociado a terremotos previos, sino también al lento hundimiento intersísmico. De este modo, se interpreta que los 24 cordones litorales estudiados han registrado cambios en el nivel de la costa asociados a ciclos sísmicos completos, lo que permite reconstruir la recurrencia sísmica de los últimos 4500 años. Durante este periodo, los intervalos de recurrencia han sido variables, sugiriendo un comportamiento débilmente periódico con al menos tres etapas con comportamiento característico: La Etapa I, entre 4400 y 3000 años antes del presente, exhibe una recurrencia de 214 ± 75 años; la Etapa II, entre 2900 y 1800 años antes del presente, muestra una recurrencia de 65 ± 22 años; y la Etapa III, entre 1700 y 600 años antes del presente, una de 243 ± 55 años. Comparando estos resultados con la recurrencia cuasi-periódica del segmento tectónico adyacente de Valdivia, se propone que, a pesar de que ambos segmentos comparten características tectónicas similares, la dinámica de acreción frontal de sedimentos, las “splay faults” y la deformación de la placa superior del segmento del Maule podrían controlar el tamaño y la periodicidad de sus terremotos.

ABSTRACT

Understanding the seismic behavior of subduction margins is essential to develop probabilistic models to estimate the occurrence of future earthquakes. This requires multi-millennial records that provide long-term seismic recurrence. In this thesis, the paleoseismic history of the Maule segment was reconstructed through the analysis of the sandy coastal ridge plain on Santa María Island, located at the southern end of the rupture area of the 2010 Chile earthquake (Mw 8.8). The response of the island's coastline to the seismic cycle, which produces seismic uplift and interseismic subsidence, was analyzed by monitoring the main beach of the island during the last eight decades (between 1941 and 2021). The observations show that coastal progradation and construction of beach ridges was continuous and did not respond only to seismic uplift associated with previous earthquakes, but also to slow interseismic subsidence. Thus, it is interpreted that the 24 beach ridges studied have registered changes in coastal level associated with complete seismic cycles, which allows reconstructing the seismic recurrence of the last 4500 years. Over this period, recurrence intervals have been variable, suggesting a weakly periodic behavior with at least three stages with distinctive behavior: Stage I, between 4400 and 3000 years before present, exhibits a recurrence of 214 ± 75 years; Stage II, between 2900 and 1800 years before present, shows a recurrence of 65 ± 22 years; and Stage III, between 1700 and 600 years before present, one of 243 ± 55 years. Comparing these results with the quasi-periodic recurrence of the adjacent Valdivia tectonic segment, it is proposed that, although both segments have similar tectonic characteristics, the dynamics of frontal sediment accretion, splay faults and upper plate deformation of the Maule segment would control the size and periodicity of their earthquakes.

ÍNDICE DE CONTENIDOS

ÍNDICE DE FIGURAS

ÍNDICE DE TABLAS

CAPÍTULO I. Introducción general

1.1. Introducción y formulación del problema

Uno de los mayores desafíos que enfrentan las ciencias de la Tierra es determinar la ocurrencia, ubicación y magnitud de futuros terremotos. Eventos sísmicos devastadores e imprevistos en los últimos 20 años, como el terremoto de Sumatra-Andamán en 2004 (Mw 9.2), Chile en 2010 (Mw 8.8), y Japón en 2011 (Mw 9.2) demuestran la necesidad de comprender la variabilidad temporal y espacial de la recurrencia de dichos fenómenos (Goldfinger *et al.*, 2013; Salditch *et al.*, 2020). Para ello, el análisis de archivos históricos y sobre todo paleosísmicos ha resultado esencial para estudiar la periodicidad de dichos fenómenos y ha revelado comportamientos complejos. Generalmente las regiones propensas a la ocurrencia de grandes terremotos (Mw > 8.5) exhiben un comportamiento de recurrencia periódico atribuible al ciclo sísmico, el cual involucra la acumulación de energía intersísmica entre placas, seguida por su liberación a través del desplazamiento cosísmico (Moernaut, 2020). Sin embargo, otras zonas muestran patrones más complejos cuando se estudian a escala de miles de años, siendo cuasi o débilmente periódico y con agrupamientos temporales de terremotos de tamaño variable separados por intervalos menos activos ("superciclos"; Sieh *et al.*, 2008; Goldfinger *et al.*, 2013). Esto conlleva a una estimación deficiente de la amenaza que presentan los eventos más relevantes en una región, con eventuales consecuencias para la sociedad. Por ejemplo, la subestimación del riesgo sísmico puede resultar en daños y un número elevado de víctimas por una planificación inadecuada, mientras que una sobreestimación podría llevar a medidas de mitigación innecesariamente costosas (Stein *et al.*, 2012).

Para conocer la periodicidad sísmica en un área determinada, es esencial contar con registros que se extiendan por miles de años, abordando múltiples ciclos sísmicos. En este contexto, la paleosismología ha desempeñado un papel crucial en la construcción de la historia sísmica, por ejemplo mediante la estratigrafía costera (e.g. Atwater *et al.*, 2005; Cisternas *et al.*, 2005; Rubin *et al.*, 2017), turbiditas (e.g. Goldfinger *et al.*, 2012; Goldfinger *et al.*, 2017;

Moernaut *et al.*, 2018) y corales (e.g. Sieh *et al.*, 2008). Para lograr interpretar un patrón de recurrencia de calidad, que contemple tasas medias, variabilidad y patrones de periodicidad, se necesitan datos paleosísmológicos que idealmente consideran un gran número de eventos, datación precisa e información sobre el tamaño relativo de los terremotos. Un ejemplo de este topo de registros es el del centro-sur de Chile, en el área de ruptura del terremoto de Valdivia de 1960, en donde se ha combinado el estudio de turbiditas lacustres, depósitos de tsunamis en marismas y lagos costeros obteniendo un registro de casi 5 mil años (Cisternas *et al.*, 2005; Kempf *et al.*, 2017; Moernaut *et al.*, 2018). Esto demuestra la necesidad de contar con varios sitios de investigación y distintas metodologías para mejorar y extender los datos.

Los estudios paleosismológicos costeros consideran que los terremotos causan cambios observables y medibles en la geomorfología y estratigrafía, debido a tsunamis (e.g., Liew *et al.*, 2010; Vargas *et al.*, 2011; Tappin *et al.*, 2012) o a los cambios verticales abruptos durante la liberación de la energía cosísmica (e.g., Plafker & Savage, 1970; Plafker, 1972; Meilianda *et al.*, 2010; Vargas *et al.*, 2011). Algunos de los primeros reportes escritos de este último fenómeno fueron hechos en Chile en la primera mitad del siglo XIX por María Graham, Robert FitzRoy y Charles Darwin en Chile (FitzRoy, 1839; Kölbl-Ebert, 1999). Estudios recientes han reportado cambios costeros abruptos luego de los terremotos de 2010 en Chile (Martínez *et al.*, 2015; Martínez *et al.*, 2021), 2011 Tohoku (e.g., Tappin *et al.*, 2012), y 2004 Sumatra-Andaman (e.g., Choowong *et al.*, 2009; Liew *et al.*, 2010; Monecke *et al.*, 2015; Monecke *et al.*, 2017). A lo largo de varios ciclos sísmicos, dichos cambios en la morfología costera pueden preservarse de diversas formas, tales como escarpes enterrados (Meyers *et al.*, 1996; Peterson *et al.*, 2010; Cisternas *et al.*, 2017; Pinegina *et al.*, 2020) o cordones litorales (Bookhagen *et al.*, 2006; McSaveney *et al.*, 2006; Pinegina *et al.*, 2013; Monecke *et al.*, 2015). Lamentablemente, existe muy poca información respecto a los efectos costeros generados por el levantamiento cosísmico asociado a terremotos recientes, siendo la mayoría estudios enfocados a los efectos del hundimiento cosísmico.

La presente tesis presenta la reconstrucción de la recurrencia de terremotos en el segmento del Maule a través del análisis de la planicie costera de una isla con una sucesión de 24 cordones litorales en el área de ruptura del terremoto de Chile en 2010 (Mw 8.8). En ella se estudió la evolución morfológica de la costa, a través del análisis de la principal playa y planicie costera adyacente de la Isla Santa María entre 1941 y 2020. Integrando los efectos intersísmicos de las décadas previas al terremoto de 2010, la deformación cosísmica abrupta y la lenta deformación durante la década posterior, con resultados previos (Bookhagen *et al.*, 2006), se propone un modelo conceptual de evolución costera, incluyendo la construcción de la planicie costera con cordones litorales. Utilizando las observaciones asociadas al evento del 2010 como análogo moderno se desarrolló un registro paleosísmico de 4500 años, abarcando 24 intervalos de recurrencia de grandes terremotos de subducción. Finalmente, se integraron los nuevos datos con la información paleosismológica existente de grandes terremotos del segmento adyacente de Valdivia y se discutieron las diferencias de periodicidad sísmica entre ambas zonas relacionándolas con las condiciones tectónicas de cada segmento.

1.2. Área de estudio e historia sísmica

La Isla Santa María (37ºS; 73.5ºW; ISM) se localiza 75 km tierra adentro desde la fosa oceánica (Figura 1.1a, b) y a 15 km sobre la zona sísmica interplaca, conformada por la interfase entre las placas de Nazca y Sudamericana (Melnick *et al.*, 2012c). La isla se encuentra asociada con el Sistema de Fallas Santa María (SFSM), enraizado en el límite de placa a ~ 15 km (Figura 1.1c; Melnick *et al.*, 2006b). Geológicamente, la isla está compuesta por una base sedimentaria bien consolidada del Eoceno-Mioceno y cubierta por depósitos del Pleistoceno y Holoceno menos consolidados (Figura 1.1d; Melnick *et al.*, 2006b). La isla está compuesta por una unidad inclinada conformada por dichas litologías, con alturas de 40 a 80 m, y una planicie arenosa holocena en la zona este por debajo de los 10 m (Figura 1.1d). Se ha propuesto que dicha planicie, que incluye dunas activas, humedales y cordones litorales, se ha originado producto de los repetidos levantamientos cosísmicos asociados a los grandes terremotos interplaca de los últimos milenios (Bookhagen *et al.*, 2006; Melnick *et al.*, 2006b). Por otra parte, el

levantamiento neto de la isla se atribuye principalmente a procesos tectónicos, ya que el rebote isostático postglacial en esta latitud se limita a la Cordillera Principal, situada a 200 km al oeste de la isla (Rabassa & Clapperton, 1990; Melnick *et al.*, 2006b).

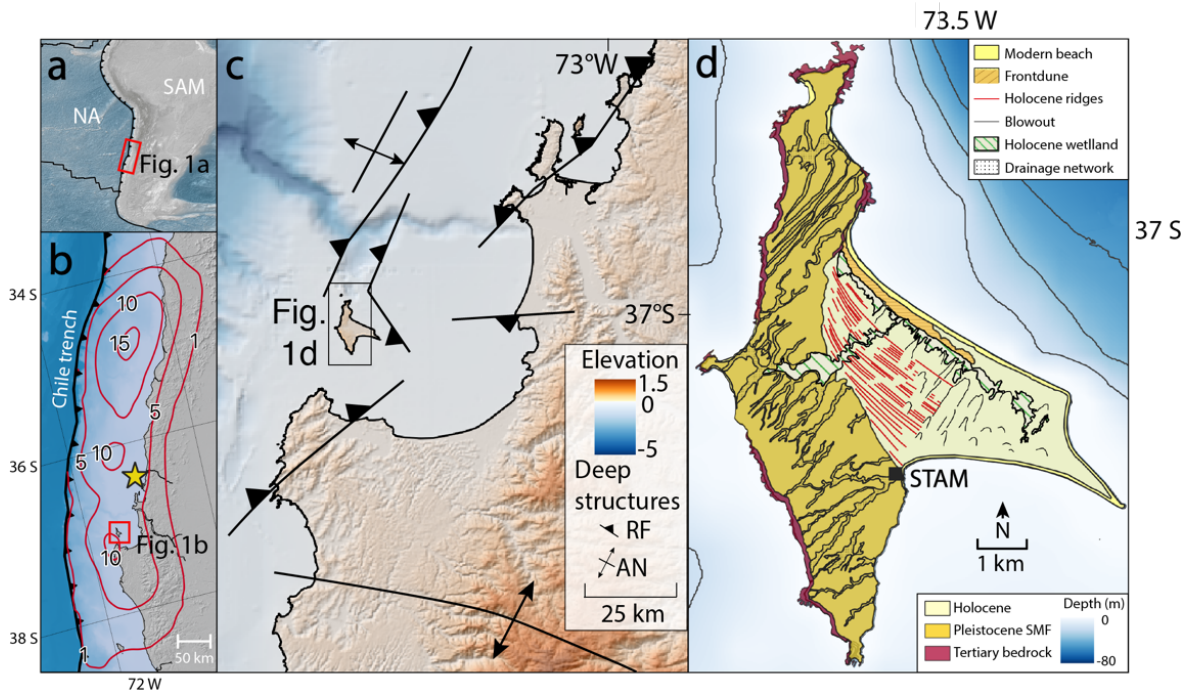

Figura 1.1. Contexto tectónico y geológico. a) Placas tectónicas de Nazca (NA) y Sudamericana (SAM). b) Localización de la Isla Santa María (ISM) en Chile central. La estrella amarilla muestra el epicentro del terremoto del Maule de 2010; contornos indican el desplazamiento cosísmico cada 5 m (Moreno *et al.*, 2012). c) Mapa del Sistema de Fallas Santa María (SMFS) asociados a ISM (Melnick *et al.*, 2012c; Jara-Muñoz *et al.*, 2017). RF: Falla Inversa, y AN: Anticlinal. d) Mapa geológico y geomorfológico de la ISM (modificado de Melnick *et al.*, 2006b). Isobatas cada 20 m (Jara-Muñoz *et al.*, 2017).

ISM se encuentra el segmento sismo-tectónico del Maule en el cual se han producido grandes terremotos históricos en 1570, 1657, 1751, 1835 y 2010 (Lomnitz, 1970; Moreno *et al.*, 2012), con intervalos de recurrencia, consistentes con el registro geológico de cambios costeros cosísmicos e inundaciones por tsunami, cada 84-175 años durante los últimos 6 siglos (Dura *et al.*, 2017). Durante el último terremoto de 2010, ISM experimentó levantamiento cosísmico de 1.6 a 2.2 m y la activación de fallas secundarias sugiriendo deslizamiento tanto del contacto entre placas como en el SFSM (Melnick *et al.*, 2012a; Melnick *et al.*, 2012c). El terremoto de

1835 (Mw > 8,5), elevó la isla entre 2.4 y 3 m (Darwin, 1839). Entre los terremotos de 1835 y 2010, ISM se hundió aproximadamente 1.6 m a un ritmo de 11.3 ± 4 mm/año (Wesson *et al.*, 2015). Esta tasa de larga escala es similar a la tasa intersísmica medida por GPS entre 2004 y 2010, y aproximadamente la mitad de la tasa media de subsidencia postsísmica 2010-2023 de 25 mm/año (Aedo *et al.*, 2023). De este modo, el ciclo sísmico en ISM incluye levantamientos cosísmicos de escala métrica seguidos de una rápida subsidencia postsísmica-intersísmica.

1.3. Hipótesis

Considerando los antecedentes expuestos se propone la siguiente hipótesis:

La deformación en la Isla Santa María, resultante del levantamiento cosísmico abrupto y el hundimiento intersísmico gradual, produce registros morfoestratigráficos en la planicie costera que son útiles para la reconstrucción paleosismológica del segmento del Maule.

1.4. Objetivos

1.4.1. Objetivo General

Reconstruir la historia paleosísmica de la Isla Santa María a través de los rasgos morfoestratigráficos de la planicie costera utilizando los efectos del terremoto del 2010 como análogo moderno.

1.4.2. Objetivos Específicos

1. Caracterizar la costa moderna, identificando y cuantificando los cambios topográficos y geomorfológicos relacionados al ciclo sísmico y al terremoto del 2010.
2. Analizar morfométrica y estratigráficamente la secuencia de cordones litorales de la planicie costera.
3. Relacionar los cambios geomorfológicos asociados al ciclo sísmico y al terremoto del 2010 con el origen de los cordones litorales y la construcción de la planicie costera.
4. Reconstruir la evolución temporal de la planicie costera con un modelo de edades basado en edades absolutas y criterios geomorfológicos.
5. Estimar la edad de cada cordón litoral e interpretar patrones de recurrencia asociados con el ciclo sísmico.

1.5. Organización de los resultados

Los resultados del presente trabajo están desarrollados en cuatro capítulos. En el primero de ellos se introduce el tema de investigación, se expone la formulación del problema y el contexto geológico general del área de estudio. Con dicha información se plantea la hipótesis y los objetivos del trabajo, así como un resumen de las principales metodologías utilizadas para el desarrollo y cumplimiento de dichos objetivos. A continuación, en los capítulos 2 y 3 se presentan dos artículos científicos enviados a revistas indexadas (WoS), donde se desarrollan los principales resultados de la tesis según los objetivos expuestos en el apartado anterior.

Primero se abordaron los efectos locales previos y posteriores al terremoto del 2010 y luego con dicho análogo moderno se desarrollaron los objetivos finales de la tesis que apuntan a la identificación de la recurrencia de terremotos. El capítulo 2 consta de un artículo publicado en la revista *Earth Surface Processes and Landforms* en el cual se muestra un monitoreo de 8 décadas, entre 1941 y 2021, del sistema costero moderno de ISM para comprender su evolución geomorfológica durante el período intersísmico, cosísmico del terremoto de 2010 y postsísmico

de la década posterior. Este estudio permitió describir los cambios sedimentarios y topográficos de la costa de la isla asociados al ciclo sísmico y proponer un modelo de construcción de la planicie de cordones litorales. En el capítulo 3, correspondiente a un segundo artículo enviado a la revista *Proceedings of the National Academy of Sciences*, se presenta un registro paleosismológico de 4500 años que incluye 24 intervalos de recurrencia de grandes terremotos de subducción en el segmento del Maule. Esto a partir de la datación y morfometría de los cordones litorales de la planicie contando con el análisis del análogo moderno caracterizado en el capítulo anterior. Luego en el artículo se integran dichos datos en el contexto tectónico del centro-sur de Chile estableciendo una comparación con el comportamiento sísmico del segmento vecino de Valdivia y discutiendo sobre las diferentes condiciones tectónicas de cada segmento. En el capítulo 4 se presenta una síntesis y discusión general donde se integran los principales resultados obtenidos en los artículos desarrollados y finalmente en el capítulo 5 se destacan las conclusiones de la presente tesis de doctorado.

1.6. Metodología

Para el desarrollo de los objetivos planteados, se describen brevemente a continuación las distintas metodologías empleadas. Los detalles específicos se abordan en el cuerpo de los siguientes dos capítulos.

1.6.1. Trabajo de campo

Se visitó el área de estudio en cuatro oportunidades, en donde se llevó a cabo la obtención de imágenes aéreas con drones Sensefly Ebee y Mavic 2 Pro para realizar el trabajo de fotogrametría. También se obtuvieron datos geofísicos con Radar de Penetración Terrestre, utilizado los equipos MALA Pro-Ex y GSSI UtilityScan y datos topográficos usando un equipo GNSS Trimble R8S RTK referenciado al datum SIRGAS utilizando la estación GNSS permanente STAM (Figura 1.1d). Se realizaron excavaciones con pala en la planicie costera de cordones litorales para describir la estratigrafía, validar y apoyar los datos geofísicos. Por

último, se recolectaron muestras de material datable con radiocarbono y muestras de arena de los distintos cordones litorales para datarlos por medio de luminiscencia IRSL.

1.6.2. Adquisición y modelamiento de datos de viento y oleaje

Se analizaron datos climáticos de viento obtenidos a través del modelo Climate Forecast System Reanalysis (CFSR) para el periodo 1985-2018 (Saha *et al.*, 2010) y se apoyaron con datos adicionales proporcionados por el Consorcio Eólico S.A (https://eolico.cl). También se trabajó con datos climáticos de oleaje modelados con el software Wavewatch III (Tolman *et al.*, 2014) y Stwave (Smith, 2001).

1.6.3. Análisis de imágenes aéreas y satelitales

Se analizaron fotografías aéreas desde 1941 hasta 2021, junto con imágenes satelitales Landsat 5,7 & 8 and Sentinel-2, para determinar los cambios horizontales de la línea de costa. Para esto se utilizó la herramienta de python CoastSat (Vos *et al.*, 2019b) y la extensión Digital Analysis System 4.4 (DSAS) de ArcGIS (Thieler *et al.*, 2009). Se realizó la medición de la posición de la línea de costa considerando el nivel de la marea en que fueron tomadas las imágenes por medio del modelo global de mareas TPXO8-atlas (Egbert & Erofeeva, 2002). Finalmente, se modelaron las tasas de cambio de la línea de costa usando un método linear de trayectoria basado en Bevis and Brown (2014) y Melnick *et al.* (2017).

1.6.4. Radar de Penetración Terrestre (GPR)

Los datos geofísicos fueron obtenidos mediante los equipos de GPR MALA Pro-Ex con una antena blindada de 250 MHz y GSSI UtilityScan con una antena de 350 MHz. En ambos casos se aplicó un intervalo de muestreo de 0,02-0,03 m. Para realizar la corrección topográfica se utilizaron los datos topográficos obtenidos por medio de un equipo GNSS Trimble R8S RTK referenciado al datum SIRGAS utilizando la estación GNSS permanente STAM (Figura 1.1d).

Los datos GPR fueron procesados mediante los softwares GSSI RADAN 7 y MatGPR R3.1 de Matlab® (Tzanis, 2010a). Para ello, se siguió una rutina de procesamiento estándar que incluye desaturación (dewow), corrección de tiempo cero, eliminación de fondo horizontal, funciones de ganancia y filtrado de paso de banda (GSSI, 2017). La interpretación fue guiada por observaciones directas de la estratigrafía en fosas excavadas para su comparación con los reflectores obtenidos mediante el GPR.

1.6.5. Reconstrucción fotogramétrica y análisis de Modelos de Elevación Digital

Las fotos adquiridas por medio de drones fueron procesadas con los softwares Agisoft Metashape v.1.5.4, Pix4Dmapper v.4 y Lastools. Se obtiuvieron mosaicos ortofotográficos y Modelos Digitales de Elevación (MDE) referenciados al datum SIRGAS mediante controles GNSS en tierra. Para el primer artículo se compararon los modelos obtenidos en marzo de 2010, febrero de 2016 y marzo de 2021, y se determinaron los cambios topográficos de la costa. Est se logró calculando un MDE de Diferencia (DoD) utilizando el paquete de código abierto Python Sandpyper (Pucino *et al.*, 2021). Para el segundo artículo se utilizó el MDE de 2016 de 15 cm de resolución que abarcó toda la planicie costera. Con este MDE se delimitaron los cordones litorales, se trazaron perfiles topográficos, y se calcularon sus parámetros morfométricos (relieve, ancho, asimetría y pendiente). Además calculamos el basculamiento de los cordones y de la planicie para compararlos con el basculamiento de la isla ocurrido durante el terremoto de 2010 (Melnick *et al.*, 2012c).

1.6.6. Datación con radiocarbono y luminiscencia

Desde las paredes limpias y rectas de excavaciones en los cordones litorales se colectaron, mediante tubos de PVC, 16 muestras de arena para análisis de luminiscencia (IRSL). Paralelamente se obtuvieron 4 muestras de restos orgánicos de poliquetos enterrado para datarlos con radiocarbono. Las muestras de luminiscencia se analizaron en el Laboratorio de

Luminiscencia de Colonia y las de radiocarbono en el laboratorio AMSDirect. Calibramos estas últimas utilizando el software OxCal versión 4.4 (Bronk Ramsey, 2021).

1.6.7. Modelo bayesiano de edades

Las edades IRSL de las arenas y las edades radiocarbónicas de los poliquetos permitieron calcular los intervalos de edad durante la construcción de los cordones litorales. Para esto, se desarrolló un modelo bayesiano de edad en OxCal considerando la interpretación del modelo conceptual deducido del análogo moderno. De este modo, se infirieron intervalos de recurrencia para los últimos 4500 años. Con ellos se analizó la mejor distribución probabilística y se calcularon los coeficientes de variación (CoV), "burstiness" (B) y coeficiente de memoria (M; Goh & Barabási, 2008). Finalmente, se calcularon tasas de cambio de la línea de costa, basculamiento y levantamiento de la planicie costera.

CAPÍTULO II. Decadal coastal evolution spanning the 2010 Maule earthquake at Isla Santa Maria, Chile: Framing Darwin's accounts of uplift over a seismic cycle

Aedo, D., Cisternas, M., Melnick, D., Esparza, C., Winckler, P. & Saldaña, B. (2023) Decadal coastal evolution spanning the 2010 Maule earthquake at Isla Santa Maria, Chile: Framing Darwin's accounts of uplift over a seismic cycle. *Earth Surface Processes and Landforms*, 48(12), 2319–2333.
Available from: https://doi.org/10.1002/esp.5615

Abstract

Charles Darwin and Robert FitzRoy documented coseismic coastal uplift associated with the great 1835 Chile earthquake (M>8.5) at Isla Santa María. In 2010, another similar earthquake (Mw 8.8) uplifted the island, ending the seismic cycle. The 2-m uplift in 2010 caused major geomorphic and sedimentologic changes to the island's sandy beaches. Understanding the processes governing these changes requires pre- and post-earthquake measurements to differentiate the effects of abrupt coseismic uplift from seasonal, annual, and decadal-scale signals. Here, we combine spatial analysis of aerial imagery, field geophysics, wind and wave models to quantify geomorphic changes between 1941 and 2021 along the main beach. During the late interseismic phase (1941-2010), a ridge-runnel system was formed and then buried by a frontal dune. Because of uplift in 2010, the shoreline prograded ~20 m, the uplifted berm was abandoned, and a new seaward berm was built. In the following decade, the abandoned berm was eroded by widening of the backshore as the shoreline and dune advanced seaward. Over the surveyed eight decades, the shoreline prograded continuously, increasing from <1 m/yr to up to 3-5 m/yr after the earthquake. We infer that these changes were caused by a sedimentary disequilibrium driven by variations in relative sea level, moving formerly passive sands from eroding cliffs and marine depths into the coastal sedimentary system, thus promoting long and cross-shore sediment transport and, utterly, accretion. Our results have implications for studying beach evolution along tectonically-active coasts associated with drastic changes in relative sea level.

2.1. Introduction

Sandy beaches are dynamic environments driven by the interaction of coastal morphology, sediment transport processes, and changes in relative sea level over a wide range of time scales. Seasonal, annual, and decadal changes are due to wave climate and wind direction, while centennial to millennial changes is due to processes that modify the sediment budget conditions, such as relative sea-level changes, coastal erosion, littoral drift, onshore-

offshore transport, and climate change (Davies, 1974; Ranasinghe, 2016). Low-regularity natural events can also cause major changes in the coastal zone morphology, such as the role of extreme oceanographic forcing (Masselink *et al.*, 2016; Barnard *et al.*, 2017; Harley *et al.*, 2017), local storm erosion (e.g., Winckler *et al.*, 2017) as well as tsunamis waves (e.g., Liew *et al.*, 2010; Vargas *et al.*, 2011; Tappin *et al.*, 2012). The availability of robust long-term decadal data and the use of novel techniques to characterize these processes are essential for understanding coastal response.

Sudden coseismic uplift and subsidence during great earthquakes have produced dramatic coastal changes (e.g., Plafker & Savage, 1970; Plafker, 1972; Meilianda *et al.*, 2010; Vargas *et al.*, 2011). The first accounts of sudden coastal coseismic uplift were made by Maria Graham following the 1822 Quintero earthquake in central Chile (Kölbl-Ebert, 1999), and by Robert FitzRoy and Charles Darwin after the 1835 Concepción earthquake in south-central Chile. FitzRoy and Darwin quantified coastal uplift at six sites surrounding the Arauco and Talcahuano Bays by leveling the elevation of dead mussels still attached to the emerged rocky shore (FitzRoy, 1839); following their footsteps, Melnick *et al.* (2012a) also used mussels to quantify coastal uplift in the same region during the 2010 earthquake. At Isla Santa María, FitzRoy and Darwin measured uplift of 2.4, 2.7, and 3.0 m at three sites located in the southern, central, and northern parts of the island, respectively. The observations of metric-scale uplift following the 1835 earthquake laid the foundation of Darwin's tectonic theories relating seismicity to the rise of mountain belts (Darwin, 1846; Wesson, 2017). In addition, FitzRoy and the officers of the HMS Beagle surveyed the topography of Isla Santa Maria and bathymetry of its surroundings producing a map that was used by Wesson *et al.* (2015) to quantify vertical deformation through the complete 1835-2010 seismic cycle.

Rapid coastal changes after coseismic subsidence were observed after the 2010 Chile (Martínez *et al.*, 2015; Martínez *et al.*, 2021), 2011 Tohoku (e.g., Tappin *et al.*, 2012), and 2004 Sumatra-Andaman (e.g., Choowong *et al.*, 2009; Liew *et al.*, 2010; Monecke *et al.*, 2015; Monecke *et al.*, 2017) great earthquakes. These studies showed that, after coseismic subsidence,

the shoreline typically receded by tens to hundreds of meters. Afterward, the beach may rapidly recover in the subsequent years and even grow back to its original position in some cases (Choowong *et al.*, 2009). In the case of uplift, the beach prograde immediately; however, only a few studies have focused on monitoring this response. Some examples, mostly short-term monitoring, were reported after the 2004 Sumatra-Andaman (Rajendran *et al.*, 2007), 2010 Chile (Martínez *et al.*, 2015 and Jaramillo *et al.*, 2012) and 2016 New Zealand (MacDonald *et al.*, 2021; Dickson *et al.*, 2022).

Over several earthquake cycles, seismically modified coastal morphologies have been preserved. For example, Goff and Sugawara (2014) suggested a shaking-driven origin of beach ridges morphologies in eastern Japan by a series of immediate and delayed after-effects created by a cascade of geomorphological processes. Buried scarps were correlated with coseismic subsidence at Cascadia's Columbia littoral cell (Meyers *et al.*, 1996; Peterson *et al.*, 2010), Avachinsky Bay (Pinegina *et al.*, 2020) and Chile (Cisternas *et al.*, 2017). In Aceh, Indonesia's coast, Monecke *et al.* (2015) described the build-up of a high-elevation ridge in response to coseismic subsidence after the 2004 Sumatra-Andaman earthquake. In contrast, stair-step beach ridges stranded by coseismic uplift have been inferred in New Zealand (McSaveney *et al.*, 2006), Chile (Bookhagen *et al.*, 2006), and Kamchatka Peninsula (Pinegina *et al.*, 2013). However, limited modern analogies are available to show how deformation caused by the seismic cycle drives the construction of beach ridge morphologies. This is especially so in places where uplift occurs.

Long-term coastal monitoring over decades spanning a great earthquake, would help to understand how their associated sudden land-level changes affect beach dynamics and morphology. Satellite and old aerial imagery provide a useful resource to assess long-term coastal changes based on high-resolution shoreline position measurements (Luijendijk *et al.*, 2018; Mentaschi *et al.*, 2018; Vos *et al.*, 2019a; Vos *et al.*, 2019b). The use of unmanned aerial systems (drones) and the modeling of digital data have been useful to assess changes in sand volume and beach morphology (Gonçalves & Henriques, 2015; Casella *et al.*, 2020; Pucino *et*

al., 2021). Here, we combined aerial and spatial imagery analysis with topographic data, geophysical field surveys, with wind and wave models to study the shoreline evolution at Isla Santa Maria between 1941 and 2020 spanning the 2010 Maule earthquake (Mw 8.8). We integrated our results with interpretations of a paleoseismic study made at the island (Bookhagen *et al.*, 2006).

2.2. Study area

Isla Santa María (37ºS; 73.5ºW; ISM) is located 75 km landward of the Chile trench (Figure 2.1a, b) and 15 km above the interplate seismogenic zone juxtaposing the Nazca and South American plates (Melnick *et al.*, 2012a). The geology includes a well-lithified Eocene-Miocene sedimentary bedrock unconformably overlaid by poorly-consolidated marine and continental Pleistocene and Holocene deposits (Melnick *et al.*, 2006b). Geomorphologically, ISM may be divided into two units: a tilted upper surface of 40 to 80 m high and a Holocene sandy plain at elevations below 10 m (Figure 2.1c, d). This plain includes active dunes, wetlands, and a sequence of parallel beach ridges that have been attributed to coseismic uplift during multiple megathrust earthquakes (Bookhagen *et al.*, 2006; Melnick *et al.*, 2006b). Net uplift of the island has been explained mainly by tectonic processes because the post-glacial isostatic rebound at its latitude is limited to the Main Cordillera, located 200 km west of the island. (Rabassa & Clapperton, 1990; Melnick *et al.*, 2006b).

During the 2010 earthquake, ISM was uplifted between 1.6 ± 0.1 and 2.2 ± 0.2 m. This range was estimated soon after the earthquake from measurements of uplifted intertidal mussels, campaign GPS observations, and resurveying a geodetic benchmark (Figure 2.1c; Melnick *et al.*, 2012a; Melnick *et al.*, 2012c). During the 10 years that followed the Maule earthquake, the continuous GPS station STAM recorded 35 cm of subsidence; between 2010 and 2012 at ~50 mm/yr with a decreasing logarithmic trend followed by a linear trend at 25 mm/yr (inset in Figure 2.1c). The 2010 earthquake was preceded by the 1835 earthquake (M>8.5), which uplifted the island 2.4 to 3 meters (Darwin, 1839; King, 1839; Wesson *et al.*, 2015). Using these

reports and historical nautical charts Wesson *et al.* (2015) estimated that between the 1835 and 2010 earthquakes, the island subsided about 1.6 m at a rate of 11.3 ± 4 mm/yr. The authors attributed this subsidence to interseismic locking and proposed that 0.15 to 0.3 m of the 1835 coseismic uplift was preserved as a crustal permanent deformation. This permanent deformation, saving ~10–20% of coseismic uplift should be sufficient to explain the island's uplift rate of ~1.5 mm/yr during the Holocene (Bookhagen *et al.*, 2006) and Pleistocene (Jara-Muñoz & Melnick, 2015). To monitor the effects generated by these level changes on the island's coast, we studied all the island's sandy beaches, focusing on beach Tres Cuevas (TCUE), which is the largest and borders the beach ridge plain (Figure 2.1).

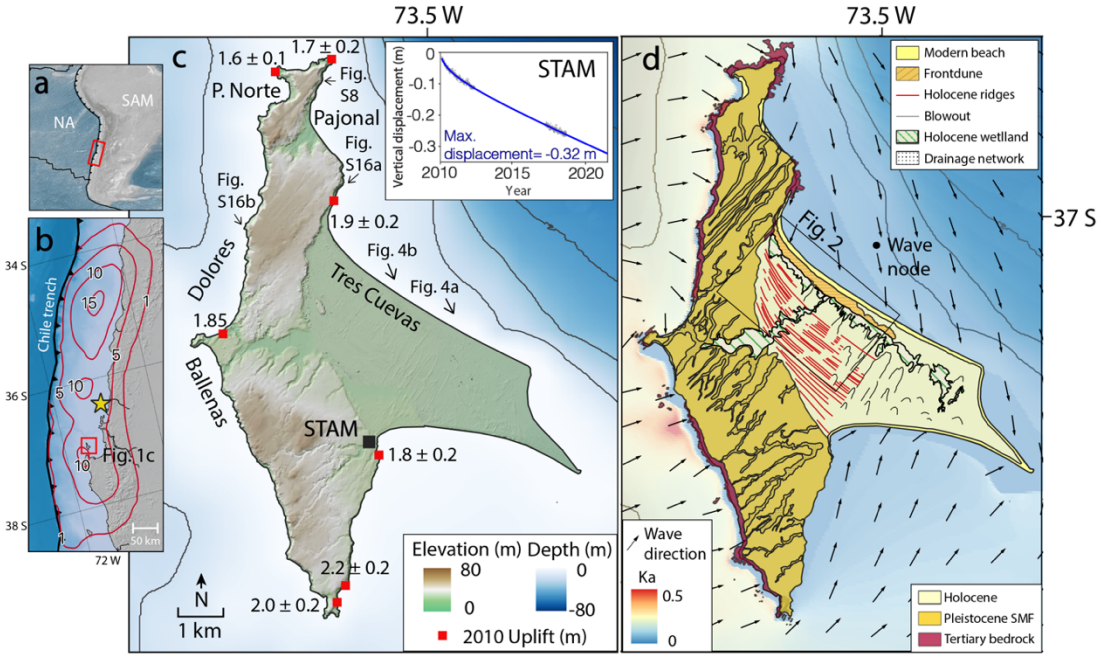

Figure 2.1. a) Tectonic setting of the Nazca (NA) - South America (SAM) margin. b) Location of Isla Santa María along the coast of central Chile. Yellow star shows the epicenter of the 2010 Maule earthquake; 5-m coseismic slip contours in meters (Moreno *et al.*, 2012). c) Shaded relief digital elevation model (5 m resolution, derived from photogrammetric restitution of aerial photos) and bathymetry (20 m resolution from Jara-Muñoz *et al.*, 2017). Coseismic uplift estimates are indicated by red squares (Melnick *et al.*, 2012c). Inset shows vertical displacement time series at continuous GPS site STAM (installed after the 2010 earthquake). Grey dots show daily positions and the blue line linear trajectory model Bevis & Brown, 2014; Melnick *et al.*, 2017 with an estimated total amount of subsidence between 2010 and 2021. d) Geologic and geomorphic map of Isla Santa María (modified from Melnick *et al.*, 2006b)with prevailing wave direction and agitation coefficient (Ka).

2.3. Material and methods

2.3.1. Wind and wave data

Wind climate was characterized using readily available modeled data from the Climate Forecast System Reanalysis (CFSR) for the period 1985-2018 (Saha *et al.*, 2010). CFSR hourly offshore surface winds at a node located 150 km westward from ISM were compared against local measured surface winds (2013-2015 monthly means) provided by Consorcio Eólico S.A (https://eolico.cl), showing good agreement. From CFSR data, a wind rose was built and used to quantitatively describe the wind regime in TCUE.

Wave climate in TCUE was modeled herein using a combination of a Pacific-wide model implemented in WAVEWATCH III (Tolman *et al.*, 2014) and the nearshore transformation model STWAVE (Smith, 2001); methodological details are included in the Supplementary Material. From the combination of both models, statistics of wave height and direction characterizing offshore wave conditions and a nearshore node located immediately off the coast of TCUE site were generated. Figure 2.1 presents the modal wave patterns expressed in terms of an agitation coefficient (Ka) defined as the ratio between nearshore and offshore wave heights (Ka>1 represents an amplification and Ka<1 a reduction). Figure S1 additionally includes wave roses offshore and at the nearshore node, as obtained from the time series included in Figure S2.

2.3.2. Field and GPR surveys

GPR data were collected using a MALA Pro-Ex system with a 250-MHz shielded antenna and a GSSI UtilityScan system with a 350-MHz antenna at a sampling interval of 0.02-0.03 m. Topography for GPR transect was surveyed using a Trimble R8S differential GPS, synchronized during data acquisition to the STAM reference station (location in Figure 2.1c); locally we used interpolated heights from drone digital elevation data. GPR processing was completed with the GSSI RADAN 7 software and Matlab® package MatGPR R3.1 (Tzanis,

2010a). We followed a standard processing routine with default settings which include desaturation (dewow), time zero correction, horizontal background removal, gain functions, bandpass filtering, and topography correction. The data visualization was supported by different excavations to calibrate and compare the signals with the sediments.

2.3.3. Spatial imagery and shoreline change time series

Eighteen georeferenced aerial photos and 1169 orthorectified satellite images covering from 1941 to 2021 were used to quantify horizontal shoreline change (Table 1). The publicly available optical satellite data was extracted using the Python toolkit CoastSat (Vos *et al.*, 2019b). Landsat 5,7 & 8 and Sentinel-2 images were pre-processed to remove cloudy pixels and enhance spatial resolution, then we removed duplicates and images with inaccurate georeferencing (threshold at 10m) to result in 839 images that were analyzed. Using the CoastSat algorithm, the images were classified into four classes (sand, water, white water, and others), and then the sand/water boundary was extracted using the Modified Normalized Difference Water Index (MNDWI). As the satellite imagery record starts in the 80s, we extended the time sequence backward by using older georeferenced aerial photos (shorelines position in Figure S3). We digitized the wet/dry line, which is assumed to be a good approximation of the high-water line (Moore, 2000; Pajak & Leatherman, 2002; Monecke *et al.*, 2015). Shoreline positions were referenced to the last image collected days before the 27 February 2010 earthquake. Perpendicular transects crossing the shorelines were digitalized with a horizontal interval of 50 m (Figure 2.2). The horizontal change in the shoreline position was quantified by fitting a least-squares regression line to all shoreline points for each transect using Digital Analysis System 4.4 (DSAS), an extension of Esri's ArcGIS software (Thieler *et al.*, 2009). Along each transect, the distance between subsequent shorelines was calculated and median and interquartile ranges were used as representative values. To measure changes in the width of the dune system, we visually traced the dune foot line from every image. This line was assumed to represent the most seaward limit of the dune, defined morphologically as an abrupt topographic change in the base of the dune (Sallenger, 2000). The rate of change was calculated using the

same methodology as for the shorelines. The backshore width was represented in this study as the distance between the shoreline and the foot of the dune for each year.

Table 2.1. Spatial imagery used in this work with estimated uncertainties. RMSE: Root Mean Square Error.

Images (sensor)	Collection	Date of acquisition (yyyy/mm)	Number of images	Resolution (m)	Geoaccuracy (m)	Runup (m)	RMSE (m)
Landsat 5 (TM)	LANDSAT/LT 05/ C01/T1_TO	1985/03-2011/04	103	30	7.03	2.77	10.68
Landsat 7 (ETM)	DSAT/LE07/ C01/T1_RT_T O	1999/09-2021/02	242	15	6.95	2.77	10.58
Landsat 8 (OLI)	LANDSAT/LC 08/ C01/T1_RT_T OA	2013/03-2021/04	121	15	6.26	2.77	9.68
Sentinel 2A/2B (MSI)	COPERNICUS/ S2	2015/09-2021/04	373	10	1.00	2.77	4.16
Air photos	IGM/SAF/Dron e	1941/01-2021/03	18	0.25-1.69	3.67	2.77	6.50

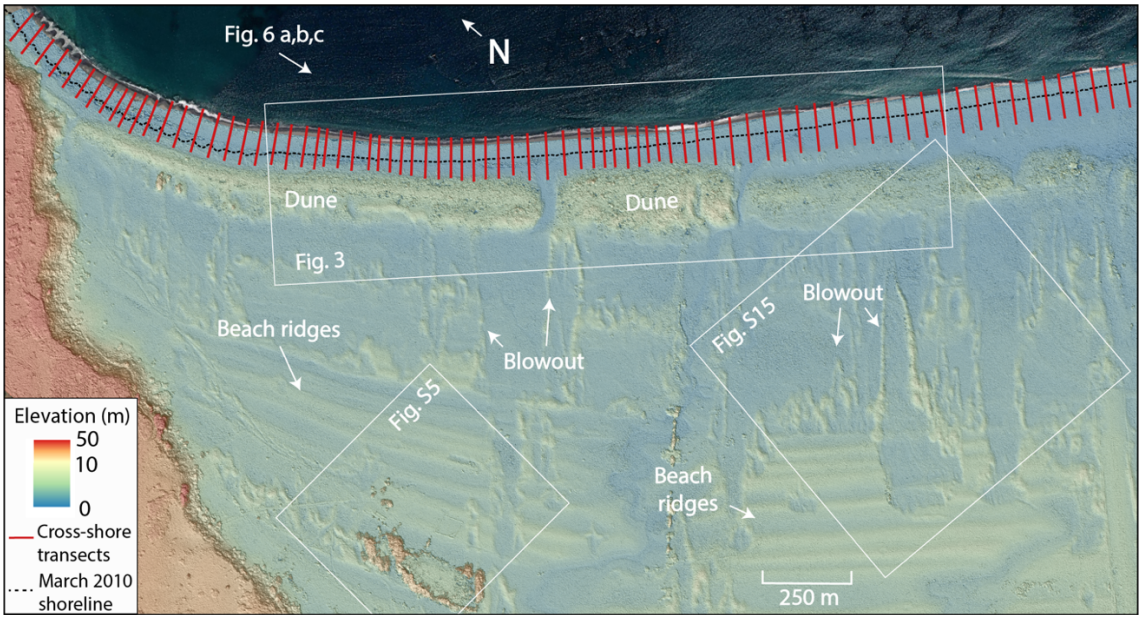

Figure 2.2. Topography of Isla María Coastal Plain (30 cm resolution, derived from photogrammetric restitution of 2016 drone photos) with all transects used and the 02/2010 shoreline as reference. Note the ridges sequence and the high topography of the frontal dune.

A tidal correction was applied using water levels calculated with the global tidal model TPXO8-atlas (Egbert & Erofeeva, 2002) and a beach face slope of $m = 0.08$ (tidal range ~1.8 m) estimated from field measurements and Digital Elevation Model calculation (Figure S4) to relate each shoreline was translated to a reference elevation above mean sea level as:

$$\Delta x = \frac{z_{ref} - z_{wl}}{m}$$

where Δx is the cross-shore horizontal shift along the shore-normal transects, z_{ref} is the reference elevation, z_{wl} is the local water level at the time of image acquisition, and m is the characteristic beach face slope. The horizontal positioning error of each shoreline was calculated as a result of the georeferencing offset and the shoreline variation due to wave run-up R (maximum elevation of shoreline oscillations caused by waves) calculated from modeled wave data using the relationship of Stockdon *et al.* (2006) Table 1). Georeferencing was cross-checked by comparing the position of stable and conspicuous ground control points (GCPs) in all images, including a landing strip, buildings, and fences, among others. All points were within less than 7.03 m of each other. The largest error was the variable run-up (average R=0.25 m) leading to an error of 2.77 m in the horizontal shoreline position. The sum of geoaccuracy and run-up errors (Root-Mean-Square, RMS) of individual shoreline positions is less than 10.68 m (Table 1). This value, which is within the expected error in shoreline detection, is mainly controlled by the effect of wave runup on the water level. It usually causes large horizontal translation of the waterline and shoreline position (Vos *et al.*, 2019a; Vos *et al.*, 2019b).

The shoreline position was modeled at 5 sites using a linear trajectory method based on Bevis and Brown (2014) and Melnick *et al.* (2017) to model $x(t)$, the shoreline position time series along a coast-normal profile as:

$$x(t) = A\,(t - t_R) + B\left(t - t_{eq}\right) + C\,\sin\left(\frac{2\pi}{\tau}\,t\right) + D\,\cos\left(\frac{2\pi}{\tau}\,t\right) + E\,\log\left(1 + \Delta t - t_{eq}/T\right)$$

where A is the coefficient of a linear function, t_R is a reference time here defined as t_0, the start of the time series, B is the coefficient of a Heaviside jump to simulate a static coseismic offset during the 2010 Maule earthquake (t_{eq}), C and D are the coefficients of a truncated Fourier Series to account for seasonal variations (we used $\tau = 1$ year for annual periods), and E is the coefficient of the transient post-seismic logarithmic component. We define $\Delta t = 0$ for $t < t_{eq}$, and otherwise $\Delta t = t - t_{eq}$. T is a constant determining the timescale of the logarithmic transient. We used a value of $T = 0.1$ based on the study of Melnick *et al.* (2017) using GNSS data after the 2010 earthquake. We used the Matlab® function *lscov* to perform the least-squares inversion in the presence of covariance accounting for the shoreline positioning uncertainties.

2.3.4. Photogrammetric Reconstruction and DEM Analysis

Aerial photos from March 2010 (1:20,000, collected by Servicio Aerogotogramétrico; SAF), and Mavic 2 Pro Drone flights conducted over the study area (Figure 2.2) in February 2016 and March 2021 were used. Photos were processed with Agisoft Metashape to obtain orthophoto mosaics and Digital Elevation Models (DEMs). The quality assessment was conducted by positioning seven GCPs using a Trimble RTK dGPS mounted on a pole (Figure S5). The dGPS was also mounted on a backpack to acquire continuous points at a frequency of 1 Hz collecting 421 independent control points (ICPs). The points surveyed referred to the time series of the STAM continuous GPS base station (Figure 2.1c). This approach was also used in an additional area of the beach to double-check the 2021 elevation model (with 6 GCPs and 547 ICPs; Figure S5). Matlab® scripts modified from Casella *et al.* (2020), were used to compare the ICPs elevation values with the DEMs at the same points to estimate the models quality.

Elevation changes were calculated based on DEMs of Difference (DoDs) and we considered the error of each DEM to calculate limit of detection thresholds for each DoD using the open-source Python package Sandpyper (Pucino *et al.*, 2021). These thresholds were calculated as the subtraction of the different DEMs over a shared area (same location used to estimate the model quality) and were defined as the expected error in the DoD inherent to DEM

noise (Figure S6). We evaluated the statistical distribution of error values, and a series of statistical parameters were calculated (Table S1). The normalized median absolute deviation was used due to the non-normality of the data (Wang *et al.*, 2015). Finally, because the models were leveled referenced to the island's position in 2021, the elevation of the 2010 and 2016 DEMs was corrected to their corresponding level by adding 0.29 m and 0.10 m, respectively, to account for the subsidence estimated from the STAM station trajectory model (inset of Figure 2.1c). Geomorphological and volumetric changes were evaluated for the 2016-2010, 2021-2016, and 2021-2010 time periods.

2.4. Results

2.4.1. Decadal changes in coastal landforms

The 1941 photo, the oldest available for TCUE beach, showed a shoreline parallel, narrow, and elongated trough, on the intertidal zone (Figure 2.3a). The zone between the trough and the surf exhibited a parallel, emerged ridge. In the central part of the studied beach, a rip channel cut through the ridge discharging the water trapped in the trough into the sea. Because the ridge and trough fit the classical description of “ridge and runnel beach” proposed by King and Williams (1949), we will henceforth use this term to refer to this feature. Likely, high waves during high tide overtop the ridge and flood the runnel, as evidenced by the wet sand shown in the photo (Figure S7). Landward of the runnel and far from the influence of the waves, a narrow longitudinal eolian accumulation of sand is observed, including blowouts oriented to the island’s predominant winds (Figure S1). The longitudinal accumulation is not developed enough to form a frontal dune (Figure 2.3a; Figure S7).

Between 1941 and one week before the 2010 earthquake the shoreline, and its frontal beach berm, advanced. Significantly, the ridge and runnel were buried by eolian sand that formed a wide frontal dune (Figure 2.3b). The abrupt 2010 coseismic uplift caused the abandonment of the beach berm. Soon after, this uplifted berm was eroded and a new beach

profile was formed, as seen in the inset of Figure 2.4a. The most remarkable post-uplift change was the rapid advance of the beach. A very wide backshore resulted from the deposition of a large amount of sand (Figure 2.4b). This large sediment mobilization is also observed in other areas of the island where uplifted rocky platforms have been completely covered by sand and transformed into new beaches (Figure S8).

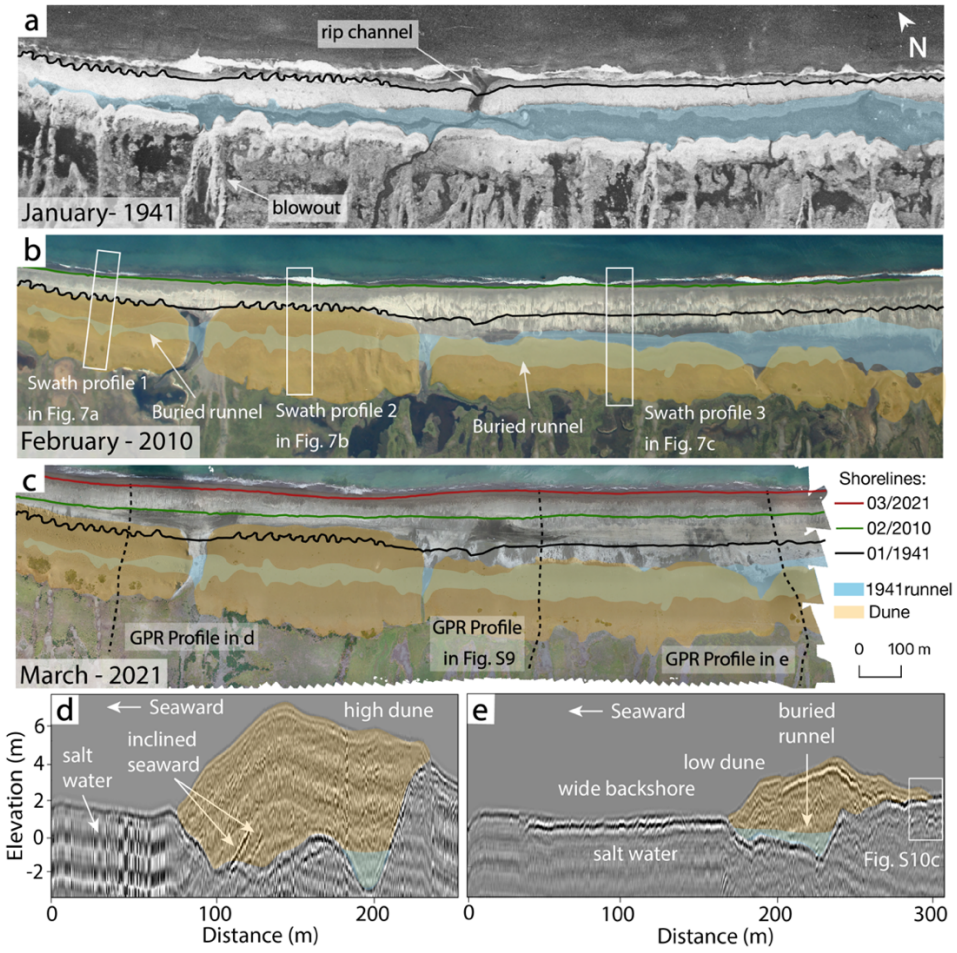

Figure 2.3. Vertical air photos from 1944, 2010, and 2021 showing geomorphic changes at Tres Cuevas beach. a) decades before the earthquake (Tide: -0.4 m).; b) one week before the earthquake (Tide: 0.3 m).; and c) 11 years after the coseismic uplift during the 2010 earthquake (Tide: -0.2 m). Note differences in sandy beach width and the burial of the 1941 morphologies by the growth of the frontal dune. An uninterpreted version of these photos is in Figure S7. d, e) GPR beach profiles showing the difference in backshore width along the beach, dune elevation, progradation signals, and buried sediments. Sources: IGM, SAF, and drone flight by D. Aedo

2.4.2. Ground Penetrating Radar Images

Post-2010 profiles across the beach showed different behaviors alongshore (Figure 2.3d, 2.3e). While the northernmost part of the beach exhibited a short backshore (< 100 m) and a high frontal dune (> 6 m), the southern part showed a wider backshore (> 150 m) and a smaller dune (3-4 m). In agreement with the evolution inferred from imagery (Figures 2.3a, 2.3b, and 2.3c), GPR profiles were able to recognize the dune-buried ridge and runnel system observed in the 1941 photo (Figures 2.3d, 2.3e, and S9). Field excavations revealed the GPR signals to represent dark beach sand with high content of heavy minerals under a layer of marine shells and eolian sediment burying them (Figure S10a-d). Excavations on the backshore of the modern shoreline showed the same black and shelly sand as seaward, 6º-sloping layers (Figure S10e), similar to the slope at the active shoreface, which ranges between 6 and 9º.

Figure 2.4. Oblique aerial photos showing changes in the shoreline associated with coseismic uplift in 2010. a) 13 days after the earthquake (Tide: -0.4 m) and b) 11 years after the earthquake (Tide: -0.2 m).

2.4.3. Time-series analysis revealing TCUE shoreline migration

Figure 2.5 summarizes the pre- and post-earthquake rates of shoreline changes on studied beaches inferred from 1941-2021 imagery, as well as the TCUE time series of horizontal coastline position. Before 2010 uplift, TCUE prograded at an average low rate of 0.6 m/yr (Figure 2.5a). Following the earthquake, the accretion rate in TCUE accelerated to an average of 3.4 m/yr. (Figure 2.5b). Although these rates in cross-shore transects (Figures S11a and S11b) showed no clear trend before 2010, in post-earthquake time they exhibited an accelerated progradation, from 3 to 5 m/yr, in the northern transects, and a slower rate between 1.5 to 3 m/yr, in the south (Figure S11e).

TCUE is sheltered to the predominant swells which (Figure S1), as a consequence of wave refraction and diffraction in the northern part of the island, have significant wave heights below 1.5 m near the surf zone (Figure S2), values that are much smaller than the offshore wave heights. The 2010 uplift did not significantly affect these parameters at the beach (<0.02 m). The trajectory model of TCUE shoreline position since 2000 reproduced well the summer/winter interseasonal variation of the beach position as well as the slow secular coastal progradation before coseismic uplift (Figure 2.5c). Immediately after the earthquake, the model accounted for a sudden beach advance of 18 ± 10 m, followed by a steady progradation at a higher pace that gradually decreased over the following decade. The complete time series since 1941 is shown in the inset of Figure 2.5c. A comparison of summer images at TCUE revealed a mean shoreline advance of 51 ± 13 m between 1941 and 2010. After that, until 2021, the coast advanced 63 ± 7 m on average. Thus, the TCUE shoreline progradation was larger in the decade after the earthquake than in the seven decades before.

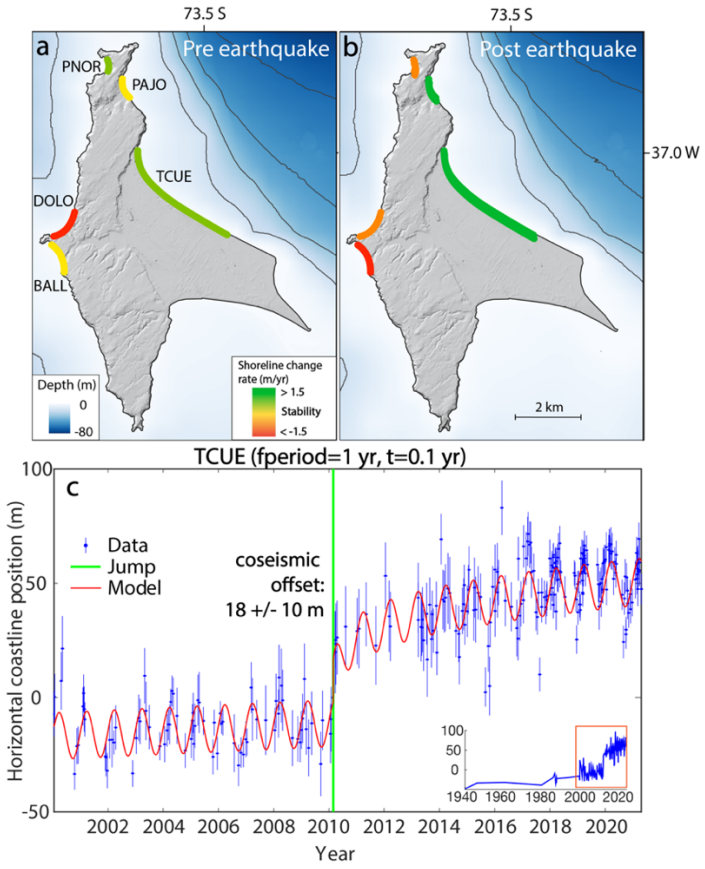

Figure 2.5. a,b) Shoreline rate changes before and after the 2010 earthquake in the island beaches, classified according to categories defined by Martínez *et al.* (2021): high erosion in red (>1.5 m/yr), stability in yellow (between -0.2 and +0.2 m/yr) and high accretion in green (>+1.5 m/yr). PNOR: Puerto Norte, DOLO: Dolores, BALL: Ballenas, PAJO: Pajonal. c) Trajectory model of Tres Cuevas horizontal shoreline position change showing the 2010 earthquake abrupt advance, the progradation rate change, and the stational variation. See methods section for details on the model. The shoreline position is referenced to the 2010 pre-earthquake (zero = 19/02/2010). Inset in the lower right shows the complete time series since 1941. Trajectory model of sites PNOR, PAJO, DOLO, and BALL are shown in Figure S13.

The monitoring of the dune toe showed seaward advancement both before and after the 2010 uplift (Figure S11c-d). The prior sequence showed a low rate of advance at an average of 0.7 m/yr, except in the beach middle, where the rate was between 1.2 to 1.8 m/yr. After the coseismic uplift, the dune front advanced rapidly at an average rate of 2.8 m/yr, similar to even larger than the rate of shoreline advance itself. In northern and middle parts of the beach, maximum rates of about 3-4 m/yr were reached (Figure S11f). In comparison, the TCUE

backshore was narrower in the years before the 2010 uplift (<50 m in 2007). Between 2014 and 2019 the extension of the backshore ranged between 57 m and 78 m. As total, between 2010 and 2021 the backshore prograded more than 50 m (Figure S11f).

2.4.4. Time-series analysis at other beaches

Before 2010 uplift, the E-facing Pajonal beach and WSW-facing Ballenas beach were relatively stable, while the WNW-facing Dolores beach receded at a rate lower than 1 m/yr (Figure 2.5a). Puerto Norte, oriented to the W, prograded at rates lower than 1 m/yr (Figure 2.5a). All beaches changed in the years following the 2010 uplift, showing eroding and prograding patterns on the western and eastern coasts, respectively. The beaches of Puerto Norte, Dolores, and Ballenas, which are exposed to predominant swells (Figure S1), receded at rates between 1 - 1.5 m/yr whereas sheltered Pajonal accreted at rates between 1.5 - 3 m/yr, similar to TCUE. As on the main study site, all these beaches also showed interseasonal variation and an abrupt co-seismic advance with similar values of 14 ± 3 m for Puerto Norte, 17 ± 7 m for Pajonal, 22 ± 3 m for Dolores, and an exceptionally high advance of 75 ± 1 m for Ballenas (complete trajectory models are included in Figure S13).

2.4.5. Topography

In general, our DEMs obtained from imagery in TCUE presented good resolution and low associated vertical RMSE errors. They ranged between 56 cm for 2010 imagery and 21 cm for 2021 (full accuracy results in Figure S5). Oblique views of TCUE using the Digital Surface Models (Figures 2.6 a-c) showed the same morphological features as the aerial photographs in Figure 2.4, including an uplifted and abandoned berm, a wide backshore zone, and a frontal dune at the back. LoD threshold values used to calculate the DoD ranged between 55 cm and 18 (Supplementary Table 1). The 2016-2010 DoD showed that almost the whole area suffered erosion between those years. The 2021-2016 DoD (Figure 2.6e) showed little change in the backshore, erosion in the dune back, and again sediment accretion on both the beach front and

the dune backshore. Finally, the 2021-2010 DoD (Figure 2.6d) showed that erosion predominated in this period, focused on the backshore and at the dune back. There was a large accretion of sediments on the beachfront due to the advance of the shoreline and accumulation on the dune front. The measured values for the study area (Figure 2.6f) showed a total erosion volume of 1.2 x 10^5 ± 3.7 x 10^4 m^3 (296 ± 91 m^3/m) between 2021 and 2010.

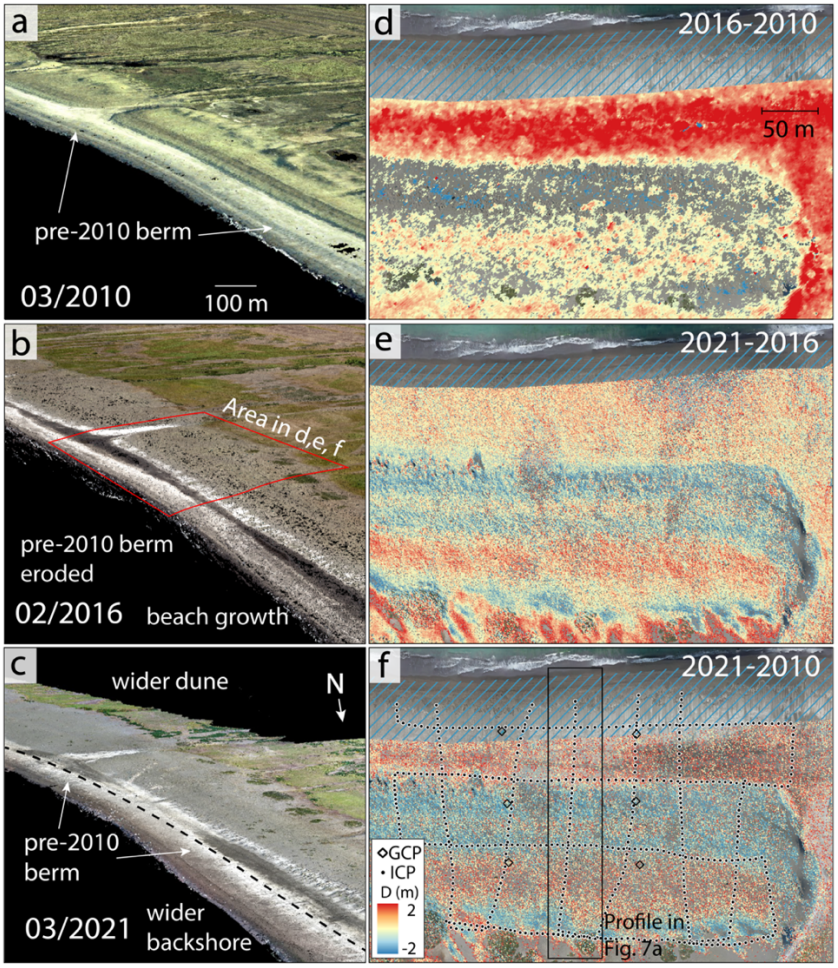

Figure 2.6. a, b, c) Digital Surface Models of the Tres Cuevas beach created using air photos for 2010 (SAF) and drone surveys for 2016 and 2021. d, e, f) DEM of Difference showing the elevation changes after the 2010 earthquake. Inset in each figure shows the mobilized sand volume above mean sea level as estimated using pairs of digital elevation models. f) shows the position of the GCP (Ground Control Point) and ICP (Independent Control Points) used to measure the topography accuracy (further details may be found in Figure S5). D: Vertical difference in meters.

Post-2010 evolution of the beach profiles showed marked erosion of the pre-earthquake berm (Figure 2.7). Balance of transported sand, between the years 2010, 2016, and 2021, are shown in the insets of Figure 2.7. In the total sum of sediment, the loss due to erosion is balanced by the accumulation of sand due to beach and dune progradation. In SP1, north of the beach, the sediment balance was positive after 11 years after the coseismic uplift. This was only observed in this profile because in SP2 and SP3, center and south of the beach, the erosion between 2016 and 2010 was predominant and produced a total sediment loss balance between 2021 and 2010.

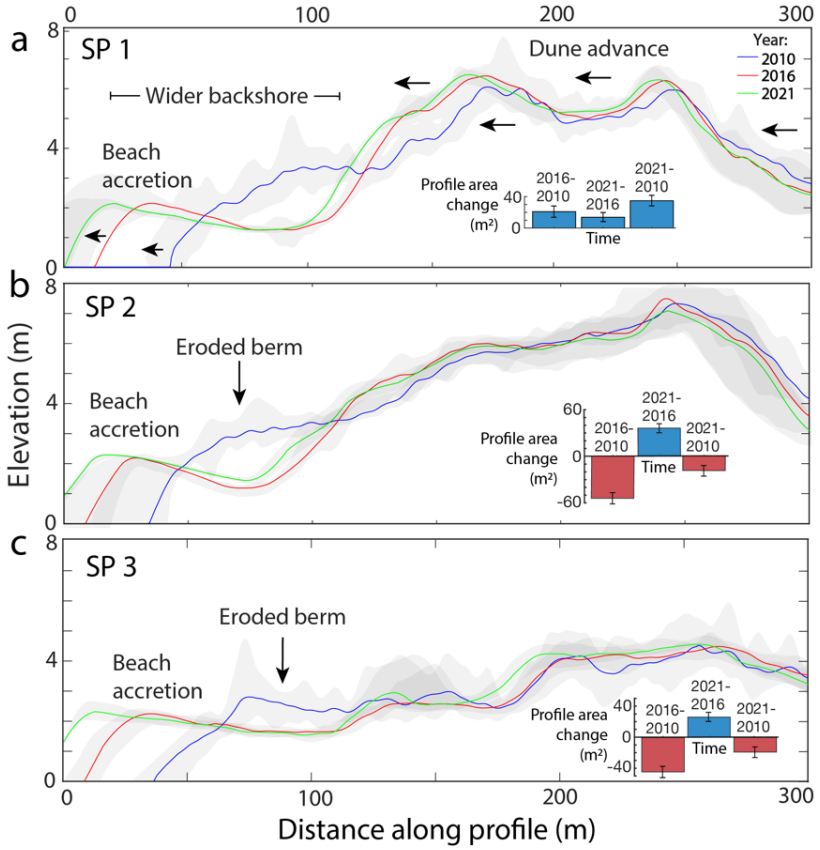

Figure 2.7. a, b, c) Swath Profiles (SP) of Tres Cuevas beach showing the morphological changes. Location of profiles in Fig. 3b. Note erosion of the uplifted berm. Insets show bar plots of area change calculated by differencing the respective profiles; blue represents positive change (sand accumulation) and red negative change (erosion).

2.5. Discussion

A strong erosional trend has been observed in sandy beaches along the Chilean coast during the last four decades (Martínez *et al.*, 2021). Changes in wave climate and relative mean sea level, a reduction in sediment supply from rivers, and local anthropogenic effects have been proposed to explain this widespread observation along nearly 2000 km of the tectonically-active Chilean coast. In contrast, TCUE beach and the coastal plain behind have prograded continuously during the late Holocene (Bookhagen *et al.*, 2006; Melnick *et al.*, 2006b), as well as during the last eight decades under scrutiny. Its protection from predominant winds and waves (Figures 2.1d and S1), which combined enhance sediment accumulation, could explain this trend. TCUE even differs from the other beaches of the same island that follow a rather erosive trend (Figure 2.5 and S13).

2.5.1 Pre-2010 beach progradation

The morphological changes experienced by TCUE during the seven decades before 2010 are represented in a conceptual model (Figure 2.8). The early interseismic phase shows a low dune probably because the aeolian sand supplied from the SW is not retained by the existing accommodation space and fast removal by coastal erosion processes (Figure 2.8a). In fact, the accommodation space during the interseismic phase was decreasing continuously as a result of relative sea-level rise induced by tectonic subsidence at 10 mm/yr (Melnick *et al.*, 2012c; Wesson *et al.*, 2015). The most significant change during the pre-earthquake phase at TCUE is the development of a large frontal dune that buried the former beach, including its conspicuous ridge and runnel system. As a consequence, the backshore zone narrowed dramatically, despite the beach accretion (Figures 2.8b, S11g, and S14). Development of outsized dunes on coastal plains has been related to low progradation, which allows more time for higher topography construction (Bristow & Pucillo, 2006; Brooke *et al.*, 2008). The pre-earthquake dune development at TCUE could respond to a positive balance of eolian sediment input from the

southwest, which in turn would depend on other processes, including changes in relative sea level, waves, and sudden sediment inputs triggered by earthquakes.

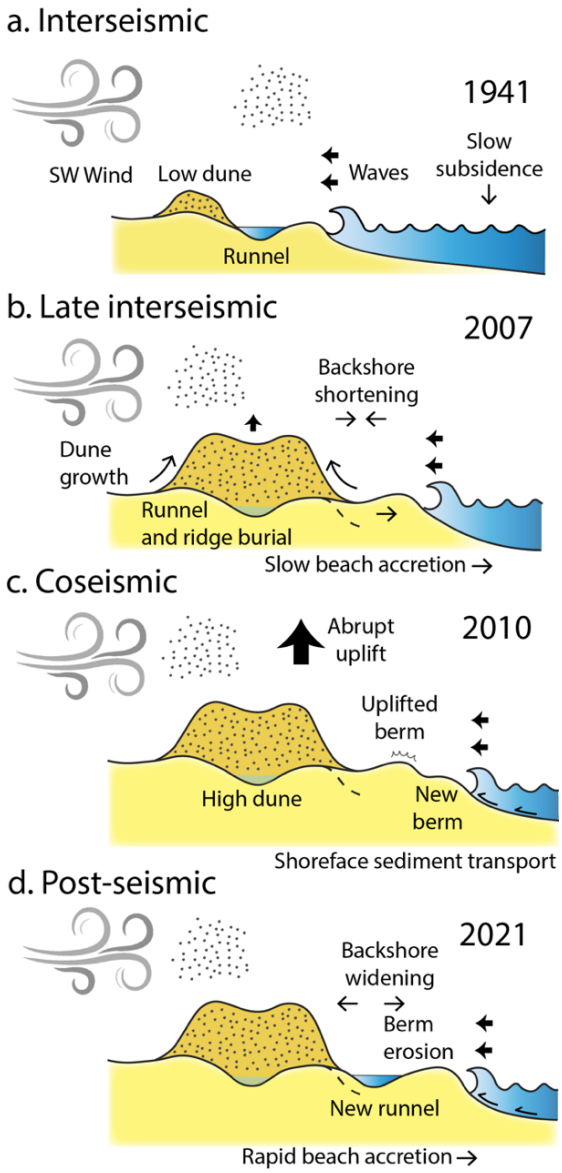

Figure 2.8. Schematic representation of the 8-decades chronology of the Tres Cuevas beach in Isla Santa Maria. The proposed coastal evolution shows a constant beach progradation accelerated by the 2010 coseismic uplift, the encounter between the prevailing wind and the waves arriving on the beach, and a frontal dune that buries the coastal morphologies of decades before the earthquake.

ISM experienced interseismic subsidence, at an average rate of 10 mm/year between 1835 and 2010, causing a fast relative sea-level rise (Wesson *et al.*, 2015). Sea-level rise often leads to coastal erosion (Bruun, 1962), which eventually delivers significant volumes of sediment to the beach (Hesp, 2013; Hesp *et al.*, 2022; Brooke *et al.*, 2015). In South Australia, a new transgressive eolian sand sheet, and eventually a dune field, was a result of the high onshore sediment supply observed during the 2010s as a consequence of sea-level rise induced by climate change (Hesp *et al.*, 2022). In another example, erosion induced by a 0.5-1.0 m coseismic subsidence during the 2004 Sumatra earthquake supplied sediment to build a particularly high beach ridge two years after the earthquake (Monecke *et al.*, 2015). Because ISM experienced rather fast interseismic subsidence before the 2010 earthquake at 10 mm/yr, sediments provided by coastal erosion from the surrounding cliffs and rock platforms resulted in burial of the ridge and runnel system that was exposed in the 1940s.

The dominant winds at ISM have produced conspicuous aeolian morphologies such as blowouts on the coastal plain (Figure S15). These features, which have been moving rapidly during the studied period, evidence important erosion on the plain and a northeastward transport of sediments towards the TCUE frontal dune. Although the offshore wave regime is characterized by predominant waves from the SW, local waves orthogonally arrive from the NW to TCUE as a consequence of refraction and diffraction on the northern tip of the island (Figure S1). A combination of i) aeolian sand transport driven by the prevailing SW winds and ii) longshore sediment transport from the slow erosion of the northwest cliff could explain the convergence of sand from both the land and sea at the TCUE beach (Figures 2.8a-b). These mechanisms characterizing the sheltered eastern portion of the island likely explain the extended plain backing TCUE, while the exposed western coast is characterized by steep cliffs and narrow pocket beaches (Figure 2.5).

A sudden supply of sediments to the ISM coast during the studied period was likely yielded by landslides triggered by the 21 May 1960 earthquake (Mw 8.1). No vertical deformation was reported at ISM by Plafker and Savage (1970) while Ojeda *et al.* (2020) suggest

only a few centimeters uplift. This event occurred only ~50 km south of ISM and generated landslides along the island's coastal cliffs according to eyewitnesses (similar to the 2010 earthquake; Melnick *et al.*, 2012c; Figure S16). Because the sediments composing the ISM cliffs have similar sedimentological characteristics to those of the modern TCUE beach and dune (Jara-Muñoz and Melnick, 2015), the 1960 landslides likely produced positive, although punctual, changes in the sedimentary budget of the TCUE beach. The predominant longshore currents (Figure S1) would favor the transport of sediments from the eroded northwestern cliffs towards the TCUE plain (Figure S16a).

2.5.2. Beach Response to the 2010 Uplift

The immediate consequence of the ~2 m coseismic uplift at ISM was the widening of the TCUE beach, abandonment of its former berm, and construction of a new seaward berm (Figure 2.8c). Furthermore, there was an abrupt advance of the shoreline of all the studied beaches with values in the order of tens of meters (Figures 2.5b and S10). A particular case is Ballenas beach, which accreted by ~75 m (Figure S13d) as a consequence of the uplift, after which it recovered the erosional trend before the 2010 earthquake. However, the new beach began to erode rapidly after 2010. The changes experienced by TCUE beach following 2010, including the erosion of the raised and abandoned berm, and the formation of a wide plain containing a new ridge and runnel system (Figure 2.8d), were probably the result of a positive sedimentary budget. This increase in available sediment has likely been controlled by RSL fall, rapid sediment mobilization, and the sudden availability of new waterborne sediment inputs.

A sudden lowering of the relative sea level creates a shallower shore face which alters the equilibrium dune-beach-berm profile (*i.e.* disequilibrium overfit case) resulting in a sediment overload and cross-shore sand transport (Anthony & Aagaard, 2020). This process may in turn result in sediment accretion and shoreline progradation by the inverse mechanism proposed by Bruun (1962). Conversely, where the relative sea level has risen due to coseismic subsidence, strong coastal erosion occurs (e.g., Peterson *et al.*, 2000; Pinegina *et al.*, 2020). At

ISM, coseismic uplift had caused a shoreface disequilibrium that in turn triggered a rapid transport of sand to the beach (Figure 2.8c). This could explain the rapid accretion of sediments at TCUE, which is sheltered from the dominant winds and waves (Figure S8). Although tsunamis are another important process that mobilizes sediment for coastal changes (Monecke *et al.*, 2015), neither the post-1960 and post-2010 earthquake images nor our field survey shortly after the 2010 event suggest a significant impact by both tsunamis at TCUE. The 2010 tsunami impacted mostly the western shores of ISM and generated only a minor swell along the eastern coastline, owing to more sheltered conditions. The effect of tsunamis along TCUE is therefore most likely minor compared to the sediment imbalance caused by coseismic uplift.

After the uplift in 2010, the TCUE beach sediments began to be vigorously mobilized. Between 2010 and 2016 a large volume of sand was eroded from the uplifted and abandoned pre-earthquake berm (Figure 2.6). Most of the resulting mobilized sediment probably contributed to the horizontal progradation of the beach although the volume balance between 2010 and 2021 was still negative (Results in 4.5). The total volume of sand lost due to erosion of the uplifted beach and berm has not been yet recovered. This negative balance is evidenced in SP2 and SP3 (Figures 2.7b-c). SP1 (Figure 2.7a) shows a somewhat different behavior in the northwestern part of the beach since, despite the initial erosion of the uplifted berm, beach accretion, and dune advancement have resulted in a positive sand balance. Possibly in this area, the dune advanced further due to the wind shadow resulting from the closer position of the cliff to the beach. Therefore, we propose that analogous processes as those inferred during relative sea-level rise (Hesp, 2013; Hesp *et al.*, 2022; Brooke *et al.*, 2015) have affected the beach during the decade after the 2010 earthquake as a result of 32 cm of land subsidence (Inset in Figure 2.1c), which fueled the coastal system with a large volume of available sediment for beach accretion.

As proposed, landslides triggered by the 2010 shaking could have contributed significant amounts of sediment to the littoral system. Coastal accretion has been liked to seismic-driven mechanisms (e.g., strong ground motion causing landslides and, utterly, fluvial transport). For

example, Moseley (1991) charted a new beach ridge on the arid Peruvian coast after the 1970 earthquake (Mw 7.7). The shaking triggered inland landslides that mobilized sediments into the catchments, which were then transported to the coast during the rainy season of the 1972-1973 El Niño event. Similar processes occurred at Sendai Plain in Japan, following the 2011 Tohoku earthquake, and in New Zealand, as a consequence of Alpine fault activity (Wells & Goff, 2007; Goff & Sugawara, 2014).

The shaking of the 2010 earthquake produced large landslides in the coastal cliffs surrounding ISM (Melnick et al., 2012b; Figure S16). Considering the proximity of some failed cliffs to the TCUE beach and the predominant longshore currents at the site (Figure 2.1d and S1), it is likely that the landslide sediments eventually became part of the sedimentary budget of the beach (Figure S16a). After the 2010 earthquake the progradation rates in the northwestern part of the beach -closer to the failed cliffs- were higher (Figure S11b). The proximity to the cliff, the direction of the currents, transporting sand toward the beach, as well as the shallower bathymetry making a disequilibrium, overfit likely mobilized sand toward the TCUE beach.

2.5.3. Interpretation of beach ridge plains as records of past earthquake cycles

This study shows a net shoreline progradation at the TCUE beach during eight decades, which includes the uplift caused by the 2010 earthquake (Figures 2.5a-b). This persistent behavior is remarkable, as it occurred during the relatively slow sinking process occurring in the late interseismic period and immediately after the rapid coseismic uplift. We herein hypothesize that this modern analog, and the similar coseismic uplift observed in the 1835 earthquake by Darwin and Fitzroy (Darwin, 1839; FitzRoy, 1839), could suggest that progradation has been persistent during previous seismic cycles, on the scale of thousands of years. Along this line, we propose that the abandoned beach ridges behind TCUE are a consequence of such cycles. Bookhagen *et al.* (2006) interpreted them as berms representing the last storms before sudden coseismic uplift associated with past large earthquakes. In this study, we show that construction of the ridge-swale topography is more complex and likely involves

inter- co- and post-seismic stages. At a short scale, the coseismically uplifted berm was rapidly eroded in the subsequent years (Figures 2.6 and 2.7). Additionally, the intertidal ridge and runnel system, another potential candidate to explain the ridge-swale topography, was buried before the uplift. These findings at TCUE are inconsistent with the conceptual model of Bookhagen *et al.* (2006) because our observations suggest that the berm formed in the last storm before the earthquake would not be preserved in the millennial-scale geomorphological record. However, although we cannot discard that a new berm will form in the following decades, it will no longer represent a record of coseismic uplift but rather of the post- or inter-seismic stages without a clear temporal relation to the timing of the earthquake.

2.6. Conclusions

We observed and quantified morphological changes along sandy beaches at ISM over eight decades spanning the 2010 Chile earthquake. We related the observed changes to the different phases of the seismic cycle, including interseismic subsidence, 2 m of coseismic uplift, and subsequent post-seismic subsidence.

During the interseismic phase before the 2010 earthquake, the shoreline of the main studied TCUE beach prograded slowly and continuously at a rate below 1m/yr. At the same time, an intertidal ridge-runnel system was buried by the seaward advance of a large frontal dune. Both processes likely resulted from a combination of factors, including a gradual sediment supply yielded as a consequence of the interseismic subsidence at ~10 mm/yr, wind ablation and deposition, longshore and cross-shore sediment transport in the surf zone, and sudden sediment inputs from earthquake-triggered landslides.

Over the coseismic phase, the shoreline suddenly advanced seaward about 20 m as the beach was suddenly uplifted 2 m. Consequently, the pre-earthquake beach and berm were separated from the intertidal zone inland. Landslides in nearby cliffs triggered by seismic

shaking during the 2010 earthquake likely supplied sediments to fuel the shoreline progradation. A new seaward beach and berm started to be built soon after the earthquake.

During the following post-seismic decade, the shoreline continued prograding at a faster rate greater than 1 m/yr associated with an advance of the foredune, and widening of the backshore. Interestingly, this progradation has continued to occur despite experiencing very fast subsidence at a rate of ~25 mm/yr as shown by GPS, which is more than twice the rate before the earthquake. This process was caused by the availability of formerly passive marine sands which became available as a consequence of the coseismic uplift, of increased sediment supply from landslides triggered by the 2010 earthquake, and continuous aeolian input. Marine sediments were then transported by wave-driven longshore and cross-shore transport, modeled by variation in relative sea level.

Our results, based on the 2010 modern analog, suggest that the progradation of the Holocene plain of beach ridge-runnel pairs has occurred continuously and is not only associated with the coseismic uplift of previous earthquakes but also with inter- and post-seismic changes in relative sea level. Therefore, the beach ridge records relative sea-level changes during complete seismic cycles including sudden coseismic uplift and slow interseismic subsidence which balance the rate of plain progradation. This conclusion is useful to interpret the record of past earthquakes in Holocene beach-ridge plains, at ISM and other tectonically-active coasts.

CAPÍTULO III. Tectonic control on great earthquake periodicity in south-central Chile.

Aedo, D., Melnick, D., Cisternas, M. & Brill, D. (2024). Tectonic control on great earthquake periodicity in south-central Chile. *Proceedings of the National Academy of Sciences*. Manuscrito enviado.

Abstract

Multi-millennial records of great megathrust earthquakes have highlighted differences in periodicity and recurrence behavior, however the underlying tectonic processes responsible for these differences are poorly understood and are relevant for fault mechanics and hazard models. Here, we present a new paleoseismic record inferred from raised beach ridges in the 2010 Maule earthquake (Mw 8.8) segment in south-central Chile that includes 24 interseismic periods over 4.5 kyr suggesting a weakly-periodic recurrence behavior. In turn, great earthquakes in the adjacent 1960 Valdivia earthquake (Mw 9.5) segment occurred with periodic recurrence over the same period. Both segments have similar amounts of trench sediments as well as rheological and geometrical boundary conditions, but Maule has a wider frontal accretionary wedge and several splay faults rooted in the seismogenic zone whereas Valdivia lacks splay faults and trench sediments are mostly subducted and underplated. These differences may have an impact on upper-plate compliance and megathrust friction, affecting earthquake size and recurrence periodicity.

Significance Statement

The largest earthquakes on Earth have occurred repetitively along subductions megathrust. Geologic archives of past subduction earthquake that extend for several millennia have shown different degrees of occurrence regularity ranging from a perfectly periodic to clustered behavior. We show that over the past 4.5 kyr, great earthquake along the Maule segment in south-central Chile have occurred with periodic and quasi-periodic behavior, while with periodic behavior along the neighboring Valdivia segment. Although most geometric and rheologic boundary conditions are similar among these two adjacent segments, differences in upper-plate compliance and fault friction may explain these differences. Our findings provide insights on how tectonic and geologic factors influence the size and timing of earthquakes, which is important for appropriate seismic hazard assessment.

3.1. Introduction

Paleoseismic records of great megathrust earthquakes including at least 10 events show variable recurrence behaviors, adding a degree of complexity to the assessment of future earthquake probabilities Satake & Atwater, 2007; Stein *et al.*, 2012; Moernaut, 2020). The unexpected 2004 Sumatra-Andaman (Mw 9.2) and 2011 Tohoku-oki (Mw 9.2) giant earthquakes demonstrate the need to include paleoseismic archives for quantifying recurrence behavior and improving forecast accuracy (Goldfinger *et al.*, 2013; Salditch *et al.*, 2020). It has been proposed that several tectonic processes may influence the recurrence behavior of great megathrust earthquakes, such as changes in megathrust geometry (Kopp, 2013); thickness and nature of incoming trench sediments (Olsen *et al.*, 2020); fault-zone permeability and fluid pressure (Moreno *et al.*, 2018); variations in upper-plate geologic structure (Bassett *et al.*, 2016); and lithospheric rheology (Gao & Wang, 2017; Julve *et al.*, 2023). The few megathrust segments that have generated the largest measured (Mw > 8.5) earthquakes are characterized by a time-dependent, periodic recurrence behavior (Moernaut, 2020), whereas most other segments by a weakly-periodic pattern that include temporal clusters of variable-size earthquakes separated by less active intervals in long-term clusters, i.e "supercycles" (Kelsey *et al.*, 2005; Sieh *et al.*, 2008; Goldfinger *et al.*, 2013). The tectonic processes that control these differences have not been fully understood and are important to gain insight into fault mechanics and its implications on seismic-cycle models with emphasis on hazard forecast.

The earthquake recurrence behavior of geologic faults may be expressed in terms of the coefficient of variation (CoV), burstiness (B), and memory coefficient (M) of recurrence intervals (Goh & Barabási, 2008; Kempf & Moernaut, 2021). A perfectly periodic sequence has CoV = 0 and B = −1, while aperiodic behavior has CoV = 1 and B = 0. In subduction zones, CoV ranges between 0.3-1 and B < 0, i.e. between quasi-periodic and weakly-periodic supercycle behavior (Moernaut, 2020; Kempf & Moernaut, 2021). The M coefficient ranges between -1 and 1, positive if short (or long) periods tend to follow short (or long) periods, and negative if short (or long) periods tend to follow long (or short) periods. Long records (>10

megathrust events) reveal features not evident in shorter records, such as clusters of large earthquakes separated by long interseismic periods in Cascadia (Kelsey *et al.*, 2005) and Sumatra (Sieh *et al.*, 2008; Rubin *et al.*, 2017), and frequent smaller earthquakes within the rupture area of occasional giant events in Tohoku (Satake, 2015). Such variability challenges the application of simple, time-independent earthquake recurrence models for hazard assessment. Although the factors responsible for these differences are not fully understood, it has been suggested that recurrence behavior is controlled by seismogenic zone width (Herrendörfer *et al.*, 2015) and superimposed cycles between adjacent megathrust asperities (Rosenau & Oncken, 2009; Philibosian & Meltzner, 2020). Here, we present a 4.5-kyr-long record including 24 paleoseismic and recurrence intervals of great megathrust earthquakes from the Maule segment in south-central Chile. We integrate our new data with a paleoseismic record of great earthquakes from the adjacent Valdivia segment and discuss the role of tectonic boundary conditions on earthquake recurrence behavior.

3.2. Seismotectonic Setting of the south-central Chile margin

South-central Chile includes the Valdivia and Maule seismotectonic segments, which last ruptured during the 1960 (Mw 9.5) and 2010 (Mw 8.8) megathrust earthquakes (fig. 1a), respectively (Moreno *et al.*, 2009; Moreno *et al.*, 2012). Both segments are separated by a persistent barrier, as suggested by historical and paleoseismic data (Ely *et al.*, 2014; Dura *et al.*, 2017; Philibosian & Meltzner, 2020), as well as numerical modeling experiments (Molina *et al.*, 2021). Long paleoseismic records (~5 kyr) from the Valdivia segment suggest giant Mw > 8.6 megathrust earthquakes have occured on average every 292 ± 93 yrs, while great Mw 7.7-8.5 earthquakes every 139 ± 69 yrs; both follow a periodic recurrence behavior with CoV = 0.5 (Kempf *et al.*, 2017; Moernaut *et al.*, 2018). In the Maule segment, great historical megathrust earthquakes occurred in 1570, 1657, 1751, 1835, and 2010 (Lomnitz, 1970), with recurrence intervals consistent with a geologic record of coseismic coastal land-level changes and tsunami inundation every 84-175 yr over the past 6 centuries (Dura *et al.*, 2017). Deformation in the Maule and Valdivia segments has the following differences: the former includes several active

splay faults along the offshore forearc (Geersen *et al.*, 2011; Lieser *et al.*, 2014) and bivergent thrust systems bounding the Main Cordillera, whereas the latter lacks mayor active forearc splay faults and the Main Cordillera is dominating by strike-slip deformation along its axis (Melnick *et al.*, 2009) (fig. 1a). The Chile trench along the Valdivia and Maule segments contains similar amounts of sediments (Contreras-Reyes *et al.*, 2010); however, these sediments are mostly underplated within a thick subduction channel and accreted beneath the continental shelf along the Valdivia segment (Bangs *et al.*, 2020), while at Maule are mostly incorporated to the frontal accretionary wedge. These differences in accretion mode have led to variation in taper angles, interpreted to reflect higher basal friction along the interplate megathrust at Valdivia (Maksymowicz, 2015; Maksymowicz *et al.*, 2021).

Isla Santa María (ISM, fig. 1) is located 75 km from the trench and associated with the Santa Maria splay-fault system, which is rooted in the plate boundary at ~ 15 km (Melnick *et al.*, 2006a). During the 2010 earthquake, ISM was uplifted between 1.6 and 2.2 m, tilted parallel to the margin (fig. 1c), and secondary faults broke the surface suggesting slip on the megathrust as well as along the splay fault (Melnick *et al.*, 2012c). The 1835 earthquake (Mw > 8.5), immediate predecessor of the 2010 event, uplifted the island by 2.4 to 3 m (Darwin, 1839). Between the 1835 and 2010 earthquakes, ISM subsided by about 1.6 m at a rate of 11.3 ± 4 mm/yr (Wesson *et al.*, 2015). This centennial rate is similar to the interseismic rate measured by GPS between 2004 and 2010, and about half the average 2010-2023 postseismic subsidence rate of 25 mm/yr (Aedo *et al.*, 2023). These observations suggest that the seismic cycle at ISM includes metric-scale coseismic uplifts followed by rapid post and interseismic subsidence. A recurrence interval of 180 ± 65 yrs for great earthquakes at ISM was estimated from a sequence of parallel ridges in a coastal plain interpreted as fossil beach berms abandoned as a result of coseismic uplift (Bookhagen *et al.*, 2006). However, a survey of coastal evolution between 1941 and 2021 including the great 2010 earthquake revealed that ridge formation rather occurred throughout post and interseismic periods, and thus represent the time between earthquakes (Aedo *et al.*, 2023). Here, we build upon observations of the 2010 cycle as a modern analog to

construct a new paleoseismic record of megathrust earthquake cycles from the ISM coastal plain.

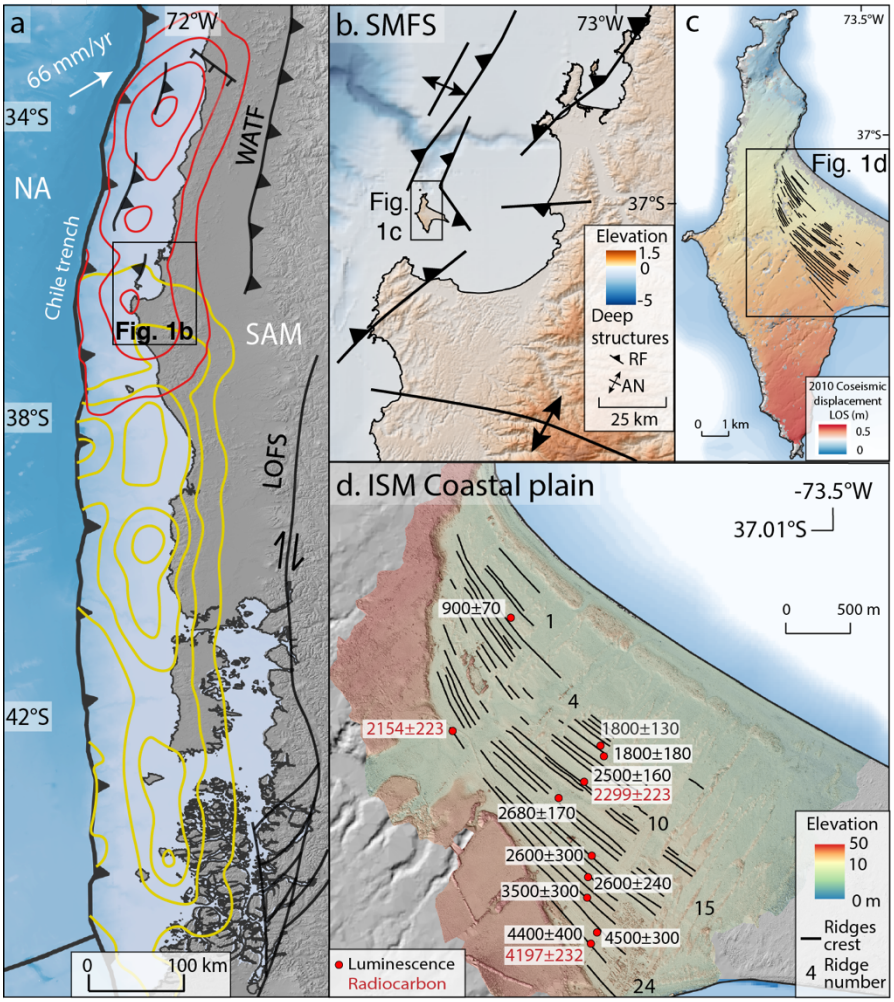

Figure 3.1. Tectonic and geomorphic setting. a) Location of the south-central Chile margin. Red and yellow contours denote cosesimic slip during the 2010 Maule and 1960 Valdivia earthquakes, respectively (Moreno *et al.*, 2009; Moreno *et al.*, 2012). WATF: Western Andean Trust Front; LOFS: Liquiñe-Ofqui Fault System; PIF: Pichilemu Fault (Geersen *et al.*, 2011; Maldonado *et al.*, 2021). b) Map of Santa María Fault System (SMFS) around Isla Santa María (ISM) (Melnick *et al.*, 2012b; Jara-Muñoz *et al.*, 2017). RF: Reverse Fault, and AN: Anticline. c) Deformation at ISM during the 2010 earthquake from unwrapped Advanced Land Observing Satellite interferogram (Melnick *et al.*, 2012b). d) ISM coastal plain topography with mapped ridges and absolute age determinations.

3.3. Results

3.3.1. Coastal plain geomorphology and stratigraphy

The ISM coastal plain consists of a series of parallel pairs of raised beach ridges and swales forming a geomorphic barcode (fig. 1c, d). Using topographic curvature calculated from a 0.15-m DEM (methods), we mapped 24 ridge-swale pairs (fig. 2, fig. S1 and fig. S2) oriented at an average strike of 134° and reaching 6.5 ± 0.2 m elevation (all elevations reported with respect to mean sea level). The ridges and swales are tilted along strike to the NW at an average of 0.025 ± 0.023° and 0.021 ± 0.016°, respectively (figs. S3-S5). Along the modern coast, the beach berm and runnel (active swale) are basically flat (fig. S6) and located at 2.2 ± 0.1 m and 1.3 ± 0.08 m, respectively. We use these elevations as the indicative meaning (Shennan, 2015) of the ridges and swales reference water level. Using the 24 ridge crest elevations, we fitted a plane oriented at the average strike of the ridges obtaining a NW tilt of 0.0344 ± 0.0006° (fig. 2a, residuals in fig. S7). During the 2010 earthquake, the coastal plain was tilted 0.0015 ± 0.0001° (fig. 2b), and if we assume this tilt as characteristic of great earthquakes, 23 ± 2 similar events would be required to equal the coastal plain tilt (fig. 2c). Interestingly, the number of events predicted by this simple relation is equal within uncertainty to the number of ridges mapped in the coastal plain. This equality suggest a causal relation and that the coseismic component expressed as along-strike plain tilt is preserved over many cycles as permanent deformation; in turn, the vertical component of coseismic deformation is partly recovered by post- and interseismic subsidence (Wesson *et al.*, 2015).

We constructed a 2.2 km long composite topographic profile across the coastal plain for geomorphic analysis (see methods, fig. 2d and fig. S8). The profile shows the sequence of 24 ridge-swale pairs with crests ranging in elevation from 2.6 ± 0.1 to 6.5 ± 0.2 m. The average ridge width is 66.4 ± 28.3 m, with significant changes throughout the sequence (fig. 2d). Cross-sections of individual ridges show a mean relief of 0.92 ± 0.41 meters and average seaward skewness of -0.45 ± 0.27 (fig. S9). The seaward and landward slopes of the ridges are within

the same order with 0.031 ± 0.017° and 0.037 ± 0.025°, respectively (fig. S9). These results show some variability within a relatively homogeneous beach ridge sequence.

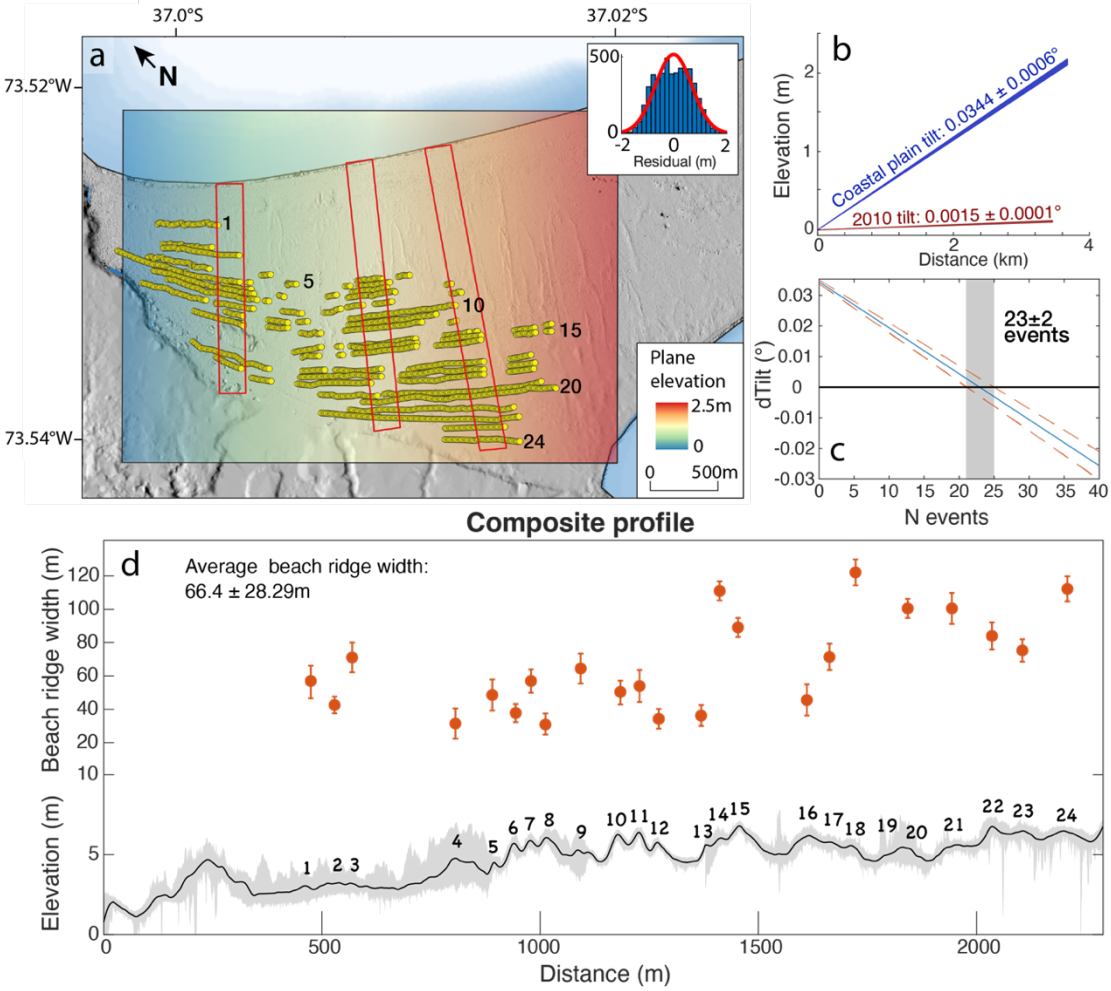

Figure 3.2. Morphometry of the ISM coastal plain. a) Map of fitted plane to ridge crest points. Note dip toward the northwest. Boxes indicate surveyed areas used for the composite topographic profile shown in d. Inset shows histogram of plane fit residuals with normal distribution curve. b) Tilt during the 2010 earthquake and along the coastal plain. c) Number of 2010-like tilt events required to achieve the plain tilt. Note similarity with number of beach ridges. d) Composite topographic profile across the coastal plain indicating ridge numbers and width measurements.

Sub-surface imaging using ground penetrating radar (GPR) profiles across the entire coastal plain shows a relatively homogeneous sequence of seaward-dipping reflectors, which we relate to beach faces formed by progressive coastal aggradation (fig. S10). Beach-face

reflectors as well as along-strike ridge topography are more discontinuous towards the youngest part of the sequence (300-800 m in fig. 2d). We associate these changes are associated with an increased sedimentary activity as the coast migrated seawards, reaching beyond the SW wind-shadow effect of the back cliff. Multiple seaward-dipping 1 to 4 m long high-amplitude reflectors are observed in GPR images throughout the sequence, which excavations reveal as 1 to 5 cm thick layers of fine-grained black sand consisting of heavy minerals (magnetite and titanite) (fig. S11-S14) likely deposited during winter storms. The continuous occurrence of heavy-mineral layers throughout the sequence interbedded in the 4 to 8° dipping reflectors supports the notion of continuous beach progradation forming the coastal plain. Periods of protracted erosion may be discarded as no signs of truncations are observed in GPR or topographic profiles.

We excavated 29 pits to survey stratigraphy and collect samples for age determinations. The stratigraphy is monotonous across the plain and consists of an upper loamy soil horizon with signs of oxidation superposed to clean gray fine to medium volcanic sand (fig. S12-S15). Layers of dark brown sand and heavy minerals were found in 6 pits (fig. S12-S15). Transitions between these layers are usually gradual, except at heavy minerals layers, where transitions are sharp (fig. S15). The similarity in sediment composition of these pits highlights the uniformity of sedimentary processes across the coastal plain.

3.3.2. Beach-ridge chronology

We collected 14 IRSL and 3 radiocarbon ages across the coastal plain (fig. 1d) and tested the IRSL accuracy to date beach ridge abandonment by verifying that 4 ages collected from the front, crest, and back of ridge number 11 overlap within analytical uncertainties down to < 1.3 m depth (fig. S16). The three radiocarbon ages were made from empty calcareous tubes of *polychaetes* worms and two of them are consistent with IRSL ages (fig. S17). We discarded a radiocarbon age that was much younger than expected from its sequential position and therefore may have been contaminated during sampling. To estimate ages of the 24 ridges, we constructed

a Bayesian age model of coastal plain progradation combining 10 IRSL and 2 radiocarbon ages (see methods), which extends between 4399 ± 154 yrs BP (the oldest dated ridge) and 1570 CE (date of first earthquake in the historical record). The agreement index of our model (a measure f the agreement between prior model and observational data expressed in terms of likelihood) is 106.4% suggesting it reproduces the agers well (fig. 3a, b and fig. S18).

The modeled time intervals between successive beach ridges have a bimodal population reproduced by a mixed normal distribution (p-value = 0.49) (fig. 4), and we can reject the hypothesis of a time-independent Poisson distribution (fig. S19a). We identify 3 distinct stages of coastal plain evolution (figs. 3a-c): Stage I, between 4.4 - 3.0 kyr with a 214 ± 75 yr average interval and progradation rates of 0.1 - 0.8 m/yr; Stage II, between 2.9 - 1.8 kyr with a 65 ± 22 yr average interval and progradation rates of 0.3 - 2.1 m/yr; and Stage III, between 1.7 - 0.6 kyr with an average 243 ± 55 yr interval and progradation rates of 0.1 - 1.0 m/yr. The CoV of stages I, II, and III is 0.35, 0.33, and 0.23; and the burstiness is -0.48, -0.50, and -0.63, respectively. The average interval of the entire ridge sequence intervals is 139 ± 94 yrs, with a CoV, burstiness, and memory of 0.68, -0.19, and 0.73, respectively. By combining the ridge intervals with those of the historical earthquakes, the average recurrence time is 135 ± 89 yrs resulting in a CoV, burstiness, and memory of 0.66, -0.21, and 0.84, respectively (fig. 4). CoV and skewness values of recurrence intervals are consistent with estimates from other subduction zones (fig. S19b).

The average uplift rate calculated only using dated ridges estimated by accounting for coastal plain tilt, indicative meaning, and absolute sea level from the ICE-6G model (Peltier *et al.*, 2015), is 0.43 ± 0.15 m/kyr (Table S1 and S2). Our estimate is much lower than a previous study (Bookhagen *et al.*, 2006) because we considered the indicative meaning and absolute sea level. The mean progressive tilt rate of the beach ridge sequence is 0.0083 ± 0.0038°/kyr (or 0.0066 ± 0.0038°/kyr using linear regression weighted by ridge length) (fig. 3d). Our tilt rate is significantly lower than the previous estimate of 0.022 ± 0.002°/kyr (Bookhagen *et al.*, 2006), possibly due to the better accuracy of our topographic data. Swales, in turn, do not show a

congruent tilt progression (fig. S20) probably because of flooding during rainy periods and associated fine-grained sedimentation that smoothed the topography. Average progressive tilt rates for Stages I, II, and III are 0.023 ± 0.015, 0.0046 ± 0.01, and 0.0069 ± 0.002, respectively, suggesting a similar underlying process with higher variability during Stage II (fig. S21).

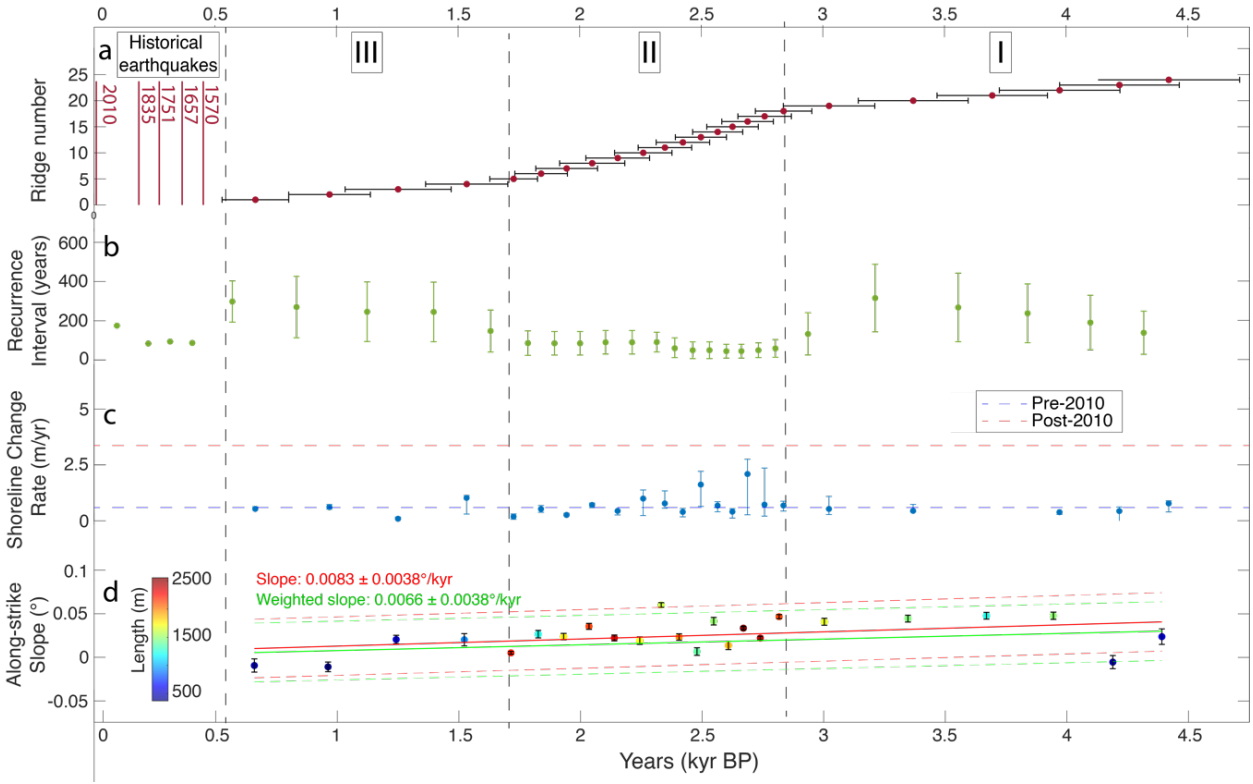

Figure 3.3. Temporal evolution of the beach ridge sequence. a) Mean ridge ages from OxCal age model (see methods) with 1 SD uncertainties. Timing of historical earthquakes indicated by vertical lines. b) Time interval between ridges and historical earthquakes. c) Shoreline change rates for individual ridges. Stippled lines show interseismic rate between 1941 and 2010, and postseismic rate between 2010 and 2021 (Aedo *et al.*, 2023). d) Evolution of along-strike ridge tilt, red and green lines show linear regressions with and without ridge-length weighting.

3.4. Discussion

3.4.1. Great earthquake recurrence record from the ISM coastal plain

We interpret the continuous topographic, stratigraphic, and geochronologic signature of the ISM coastal plain geomorphic barcode as a record of seismic cycles over the past 4.5 kyr, based on the 2010 earthquake cycle modern analog (Aedo *et al.*, 2023). We propose that each ridge-swale pair records an interseismic period between two consecutive great earthquakes, and therefore we interpret the time interval between adjacent ridge-swale pairs as a proxy for earthquake recurrence. GPR profiles showed ridges associated with the most recent historical earthquakes buried below the frontal dune; and aerial images showed that this dune migrated seaward as the coastal plain growths exhuming older ridges (Aedo *et al.*, 2023). Because of the unique setting of this island away from major sources of terrestrial sediment supply such as Andean rivers, relative sea-level changes associated with the seismic cycle and local sand supply from marine depth and sea-cliff erosion have controlled the progressive construction of the ridge-swale plain.

The 4 historical earthquakes that affected the Maule segment between 1570 and 1835 ocurred periodically every 88 ± 5 yrs. Interestingly, this range of recurrence is similar to the interval between paleoearthquakes of Stage II (65 ± 22 yrs). However, Stage II includes 8 intervals with shorter average recurrence of 43 - 62 yrs between 2.3 - 2.9 kyr. These short intervals are characterized by narrow ridges associated with high progradation rates (fig. 2d and fig. 3c) Between the 1835 and 2010 events the recurrence time doubled to 175 years, similar to the intervals of Stage I (214 ± 75 yrs) and Stage III (243 ± 55 yrs). These stages are characterized by wider ridges and lower progradation rates (fig. 2d and fig. 3c), similar to Holocene beach ridge plains in Australia that have been associated with long, multi-centennial build-up times (Bristow & Pucillo, 2006; Brooke *et al.*, 2008). Therefore, changes in recurrence intervals are consistent with variations in beach ridge morphometry suggesting both are controlled by the same underlying process – the seismic cycle. The similarities between recurrence times estimated from our geomorphic barcode record with those from historical events and a 600 yr

long geologic record (Dura *et al.*, 2017), together with the progressive and continuous changes in measured recurrence intervals (rather than stochastic) suggest that these changes are robust. Interestingly, both the historical and paleoseismic recurrence intervals alternate between short (<100 yr) and long (~200 yr) values.

The ISM paleoseismic record suggests weakly-periodic earthquake recurrence intervals, consistent with records from most subduction zones (Moernaut, 2020). In terms of recurrence intervals of great megathrust earthquakes, the Maule segment exhibits supercycle behavior, similar to the multi-millenial record of great earthquakes in Cascadia (Kelsey *et al.*, 2005), as well as other subduction zones such as Sumatra and Tohoku (Sieh *et al.*, 2008; Goldfinger *et al.*, 2013; Satake, 2015; Rubin *et al.*, 2017; Moernaut, 2020). Clustered earthquakes as observed during late Stage II are not common but have been inferred from tsunami and turbidite records in Cascadia (Kelsey *et al.*, 2005; Goldfinger *et al.*, 2013), as well as from corals in Sumatra (Philibosian *et al.*, 2017). Progradation of the ISM coastal plain has occurred at an average rate of 0.6 m/yr (fig. 3c), similar to the interseismic rate measured between 1941 and the 2010 earthquake (Aedo *et al.*, 2023). In turn, between 2.9 and 2.3 kyr (Stage II), progradation rates reached 2.1 m/yr (fig. 3c), similar to the postseismic rate measured during the decade after the 2010 earthquake (Aedo *et al.*, 2023). These high rates may reflect the protracted effect of the last over-imposed postseismic progradation during a cluster of earthquakes separated by very short time intervals, as opposed to the long interseismic intervals observed during Stage I and III (fig. 3a, b).

3.4.2. Possible link between megathrust earthquakes and splay faulting at millennial scale

Slip along the Santa María splay fault was inferred during the 2010 earthquake based on fresh surface ruptures along previously mapped faults (Melnick *et al.*, 2012b). Slip on upper-plate faults was triggered after the Maule earthquake including a Mw 7.0 earthquake (Lieser *et al.*, 2014; Jara-Muñoz *et al.*, 2022). Although splay faulting has been triggered during only a few great megathrust earthquakes, several lines of evidence suggest such secondary faults may

commonly accompany great interplate events (Plafter, 1967; Li *et al.*, 2014; Hollingsworth *et al.*, 2017; Jara-Muñoz *et al.*, 2017; Shyu *et al.*, 2018).

InSAR data showed that ISM was tilted parallel to the margin during the 2010 earthquake (fig. 1c), and we found that the number of beach ridges multiplied by the 2010 tilt angle equals the coastal plain tilt (fig. 2b, 2c). This suggests a similar underlying mechanism over the past 4.5 kyr. ISM tilt has been related to growth of a reverse fault-cored anticline rooted in the megathrust (Melnick *et al.*, 2009), and therefore the relation between coseismic tilt during the 2010 earthquake and coastal plain tilt (fig. 2b) suggests that splay faulting may have accompanied previous earthquakes (fig. S21). Our estimated average uplift rate of 0.43 ± 0.15 mm/yr over the past 4.5 kyr is about 75% lower than estimates over the past 50 kyr (Jara-Muñoz & Melnick, 2015), suggesting changes in the underlying processes, or its rates, at multimillennial timescale. Modeling of uplift rates across the Santa María splay fault system suggests it plays a major role in deformation at ISM and across the Arauco Bay (Jara-Muñoz *et al.*, 2017), and therefore the decrease in uplift rate may be associated with changes in the slip rate of the fault system. These changes may also explain the large variability in tilt rates estimated during Stage II in contrast to rather constant tilt rates during Stage I and III. Our results support the notion that splay fault slip has commonly accompanied past great megathrust earthquakes along the Maule segments.

3.4.3. Tectonic control on megathrust earthquake periodicity in the Maule and Valdivia segments

With a CoV of 0.66 and B of -0.21, the Maule segment is less periodic than its south-neighboring Valdivia segment characterized by a CoV of 0.5 and B of -0.34 (fig. 4) (Moernaut *et al.*, 2018). However, the positive M of 0.73 at Maule indicates that consecutive recurrence intervals tend to be more similar than at Valdivia where $M \sim 0$ suggests different successive intervals. The lower CoV (0.35, 0.33, and 0.23) and B (-0.48, -0.50, and -0.63) values for the three stages at ISM confirm a very periodic recurrence interval within each stage in contrast to the overall weakly-periodic behavior for the entire sequence. Therefore, changes in the tectonic

boundary conditions of the Maule segment at the timescale of 1 to 2 kyr are apparently responsible for its less periodic recurrence behavior with respect to Valdivia.

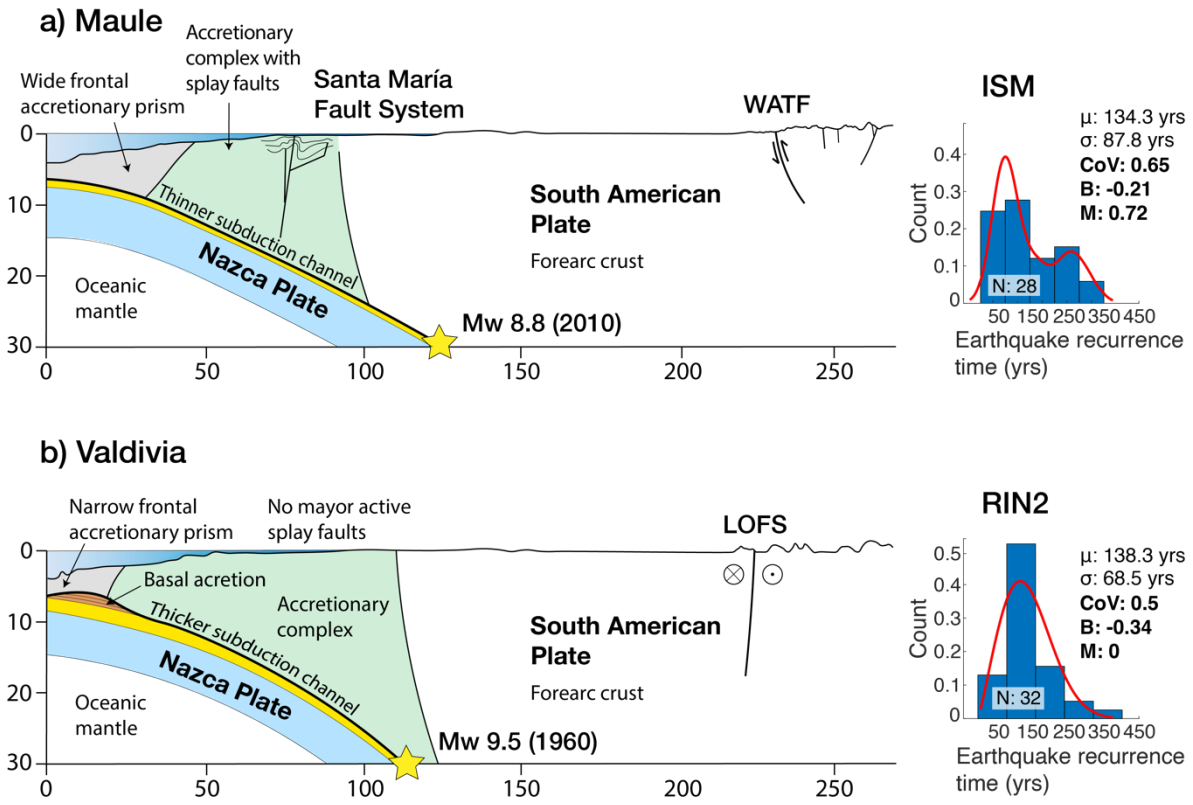

Figure 3.4. Seismotectonic characteristics of the Maule (a) and Valdivia (b) segments. Accretionary wedge and subduction channel geometries based on (Contreras-Reyes *et al.*, 2010; Geersen *et al.*, 2011; Melnick *et al.*, 2012b; Jara-Muñoz *et al.*, 2017; Bangs *et al.*, 2020; Maldonado *et al.*, 2021). RIN2 paleoseismic record from (Moernaut *et al.*, 2018). Differences in frontal accretionary wedge size, subduction channel thickness, and presence of splay faults may influence megathrust friction and upper-plate compliance, respectively, affecting great earthquakes recurrence periodicity.

While most of the geometric (convergence rate, megathrust dip, and strike, incoming plate relief) and rheologic (thermal regime, lithospheric thickness, forearc density, and composition) boundary conditions are relatively similar in both segments, they also exhibit some tectonic differences. Although the trench along both segments is filled with about 2 km of sediments, these are mostly underplated along a thick subduction channel and basally accreted below the continental shelf at Valdivia (Bangs *et al.*, 2020), while mostly frontally accreted at Maule

(Contreras-Reyes *et al.*, 2010). These accretionary differences result in different taper angles, which because the continental framework is similar at both segments, has been interpreted as higher effective basal friction at Valdivia (Maksymowicz, 2015; Maksymowicz *et al.*, 2021). Higher friction implies the megathrust may sustain higher stresses (Sallarès & Ranero, 2019) allowing for the longer interseismic periods and larger earthquake magnitudes at Valdivia with respect to Maule. However, differences in basal friction are expected to act over $>10^5$ yr timescales and therefore not responsible for the 1-2 kyr change in earthquake recurrence behavior observed at ISM.

Upper-plate deformation is another difference between the Maule and Valdivia segments. The Maule forearc is characterized by widespread active splay faulting below the shelf-slope transition (Geersen *et al.*, 2011), within the continental shelf (Bernhardt *et al.*, 2015; Jara-Muñoz *et al.*, 2017) and along the coastline (Maldonado *et al.*, 2021; Jara-Muñoz *et al.*, 2022). In turn, faults along the Valdivia offshore forearc are sealed by Plio-Quaternary sediments and thus no longer active (Echaurren *et al.*, 2022). The differences in upper-plain strain between these segments are further underscored by the deformation style along the Main Cordillera, which is characterized by bivergent foothill thrust fronts along Maule, while at Valdivia deformation is localized along a strike-slip fault system that straddles the axial volcanic arc (fig. 1a and fig. 4b). Margin-normal upper-plate strain is higher at Maule and accounted for by several contractional structures extending across the offshore forearc (Maldonado *et al.*, 2021). At Valdivia, in turn, margin-normal strain is lower and plate convergence is mostly accounted for by great earthquakes, which may therefore reach larger magnitudes than at Maule.

Widespread splay faulting results in a less compliant upper plate, and if splay faulting frequently accompanies megathrust earthquakes at Maule, then interseismic strain is released both by megathrust and splay fault slip. Therefore, we propose that differences in upper-plate strain and megathrust friction between the Maule and Valdivia segments may explain the variation in recurrence rate and behavior. Because splay faults have complex geometries, their activation may interfere with the megathrust seismic cycle ultimately conditioning the

centennial-scale changes in recurrence intervals observed at ISM over the past 4.5 kyr. Our study highlights the possible influence of margin-scale tectonic features on the recurrence behavior of great earthquakes as revealed by comparisons of long (>10 events) paleoseismic records, with implications on their use for estimating the probability of forthcoming earthquakes.

3.5. Materials and Methods

3.5.1. Ground-penetrating radar surveys

We surveyed three 1650, 2110, and 2578 m long GPR profiles across the ISM coastal plain using a MALA Pro-Ex control unit with a 250-MHz antenna (fig. S10). To search for suitable sites for excavations and sample collection we used a GSSI UtilityScan instrument and 350-MHz antenna (fig. S12-S14). We surveyed topography with a Trimble R8S RTK GNSS instrument and referred points to the SIRGAS datum using the STAM permanent GNSS station (location in fig. 1c). We processed GPR data and visualized the results using the GSSI RADAN 7 software and the MatGPR R3.1 package for Matlab® (Tzanis, 2010b). We followed a standard processing routine (GSSI, 2017), including dewow filtering, zero-time correction, horizontal background removal, gain adjustments, bandpass filtering, and topographic corrections. The interpretation of GPR images was validated with detailed stratigraphic leveling in five 1.2-1.8 m-deep pits (fig. 5C, fig. S12-S14 and 13 in fig. S15)

3.5.2. Morphometric analysis using high-resolution topography

We collected 474 vertical aerial photos using a Sensefly Ebee drone in February 2016 and used the Pix4Dmapper v.4 software to obtain an orthophoto mosaic and point cloud with an average density of 43.3 points/m^2. Using the Lastools software, we produced a gridded DEM with 0.15 m resolution, which we referenced to the SIRGAS datum using ground control points collected with a Trimble R8 RTK GNSS instrument (fig. S22a). The difference between DEM and RTK elevations follows a normal distribution with no artificial trends or distortions (fig

S22b-d). We calculated the contour curvature of the DEM (second numerical derivative of elevation) to automatically delimitate crests and valleys of ridges and swales using the topotoolbox-2 curvature function (Schmidt *et al.*, 2003; Schwanghart & Scherler, 2014), which we classified to obtain 5139 equidistant points at 10-m spacing. Using the elevation of these points, we calculated for each ridge and swale the strike and along-strike tilt with 95% confidence intervals. Using the elevation of all ridges and swales we fitted a 17 km^2 planar surface and compared its tilt and strike with those of the ridges and swales. We evaluated the fit quality using the X^2 criteria at 95% confidence to determine that residuals are not significantly different from a Gaussian distribution. We compared the coastal plain tilt with the coseismic tilt during the 2010 Maule earthquake obtained from an ALOS (Advanced Land Observing Satellite) interferogram (Melnick *et al.*, 2012b). Finally, we calculated the number of 2010 earthquake-like events necessary for the difference between the total plain tilt and the 2010 tilt to be zero. We also calculated the along-strike topography of the modern beach to search for tilt and calculated the Indicative Meaning (IM) of modern ridges and swales reference water level (Shennan, 2015).

Because ridges are locally covered by dune fields and eroded by a single stream that drains the island's highlands (fig. S11), we analyzed the across-strike topography using a composite profile that integrates the three long profiles surveyed with GPR and RTK (fig. 2a, d). These three profiles were merged by fitting their topography using a dynamic time-warping function (Wang, 2023). Using the composite profile, we calculated the morphometric parameters of each ridge including relief, width, skewness, and seaward and landward slopes (fig. S9).

3.5.3. Bayesian age modeling

We collected a total of 14 sediment samples from the ridges for luminescence dating and 3 samples of empty calcareous tubes of *polychaetes* worms from ridges 11, 17 and 24 for radiocarbon dating (details in SI Text). We used 10 IRSL and 2 radiocarbon ages in a Bayesian

model of coastal plain progradation, which considered a *Sequence* where each of the 24 ridges corresponds to a different *Phase* (interseismic time) separated by a *Boundary* (coseismic time) obtaining the time *Interval* (recurrence) of these 24 *Phases* (Bronk Ramsey, 2009). We excluded the radiocarbon date of the ridge 17, because the calibrated value is X years younger than the preceding ridges, an effect that may have resulted from contamination, and that is not consistent with the sequential order from the other 12 ages (fig. S17 and Table S5). We considered the 68.3% (1-sigma) range for the modeled ages (OxCal code may be found in the Supplementary Text) and the median with the interquartile range for the intervals. We evaluated the time-independence of recurrence intervals using a Poissonian recurrence model and calculated the best distribution of recurrence times (Williams *et al.*, 2017; Novack-Gottshall & Wang, 2019; Moernaut, 2020). We also calculated the coefficient of variation (CoV), burstiness (B), and memory coefficient (M) (Goh & Barabási, 2008).

We used the modeled ages to analyze the tilt variation of each ridge over time by fitting a linear regression and a weighted linear regression line to the data to calculate the trend. The same calculation was performed for each Stage separately, excluding the oldest ridges shorter than 500 m. We then calculated the shoreline change rate on the assumption that each ridge approximates a paleo shoreline and compared with modern pre- and post-2010 progradation rates (Aedo *et al.*, 2023). Finally, for ridges with absolute ages, we calculated averaged uplift rates by subtracting ridge elevation, coastal plain tilting, absolute sea level from the ICE-6G model (Peltier *et al.*, 2015), and indicative meaning using modern berm elevation (Table S6 and S7).

CAPÍTULO IV. Síntesis y discusión

La presente tesis reconstruye la historia paleosísmica de la planicie costera de cordones litorales en ISM. Esto, mediante el estudio de los efectos que el terremoto del 2010 (Mw 8.8), entendido como análogo moderno, tuvo en la geomorfología costera de la isla y cómo tales efectos se relacionan con la construcción de los cordones. En la sección 4.1 se expone la respuesta de la costa al abrupto levantamiento del 2010 y posterior hundimiento asociado. Para esto, se realizó un monitoreo que abarcó las últimas ocho décadas, incluyendo el evento de 2010. Luego, la sección 4.2 aborda la relación del ciclo sísmico con la conservación del registro morfológico que observamos en la isla. Con dicho conocimiento como base, en la sección 4.3 se discute la información paleosismológica que puede extraerse de la serie de cordones litorales, proponiendo un comportamiento sísmico particular para el segmento del Maule durante los últimos 4500 años. En la sección 4.4 se contextualiza dicho comportamiento dentro del margen chileno discutiendo las diferencias con el segmento vecino de Valdivia. Finalmente, en la sección 4.5 se ofrecen algunas implicancias y perspectivas de la presente tesis.

4.1. Respuesta costera al ciclo sísmico

A pesar que durante las últimas cuatro décadas observa que la mayoría de las playas arenosas del centro-sur de Chile han experimentado una tendencia erosiva debido a factores climáticos, sedimentarios y antrópicos (Martínez *et al.*, 2021), la costa estudiada en ISM ha progradado continuamente. Un proceso que se observa durante todo el Holoceno tardío (Bookhagen *et al.*, 2006; ver Capítulo 3). Esto, probablemente responde a que dicha costa presenta una orientación NE protegida de los vientos y olas predominantes. El monitoreo de las últimas ocho décadas expuesto con detalle en el Capítulo 2 (Figura 2.8) y publicado en Aedo *et al.* (2023) muestra básicamente las siguientes respuestas de aquella costa según la fase sísmica:

Período intersísmico: Durante las siete décadas anteriores al terremoto del 2010 ingresa gran cantidad de sedimento al sistema costero, provocando cambios geomorfológicos evidentes.

Hacia 1941 la costa presenta una zona intermareal de “beach ridge” y “runnel” que durante las décadas posteriores son sepultados bajo una gran duna frontal. Esto ocurre junto con la lenta progradación de la costa a tasas inferiores a 1m/año. El desarrollo de dunas de gran tamaño se ha relacionado previamente con tasas bajas de progradación, las que otorgan más tiempo disponible para la construcción de topografía más alta (Bristow & Pucillo, 2006; Brooke *et al.*, 2008). Estos procesos en ISM son probablemente el resultado de la combinación de los siguientes factores:

- El aporte gradual de sedimento como consecuencia de la erosión costera asociada a la subsidencia intersísmica de ~10 mm/año.
- La movilización y depositación eólica de arenas provenientes de la planicie costera.
- El transporte de sedimentos a lo largo y a lo ancho de la costa en la zona de oleaje.
- Aportes repentinos de sedimentos procedentes de deslizamientos subaéreos de los acantilados del noroeste.

En el presente trabajo se propone que la morfología original de “beach ridge” y “runnel” observada en los registros fotográficos de 1941, y que luego es enterrada bajo la duna frontal, corresponde a la base del registro de “ridges” (o cordón litoral) y “swales” que se observa en la planicie costera de ISM.

Período cosísmico: En el capítulo 2 se reporta que el levantamiento cosísmico de 1.6 a 2.2 m de ISM en el terremoto de 2010 provocó que la berma de playa se levantara y quedara sobre la zona intermareal. Además, se produjo un avance repentino de la línea de costa de aproximadamente 20 metros y la rápida construcción de una nueva berma. Tanto el repentino alzamiento de la zona submareal como los deslizamientos subaéreos observados en los acantilados cercanos aportaron los sedimentos necesarios para este rápido proceso.

Período post-sísmico: El efecto inmediato después del terremoto de 2010 fue la erosión de la antigua berma de playa, alzada luego del levantamiento cosísmico. Durante la década posterior, la tasa de progradación de la costa se acelera a más de 2 m/año, lo que significó un

rápido avance de la playa, de la duna y además el ensanchamiento de la costa. Estos efectos son causados principalmente por:

- El transporte de arenas marinas, anteriormente pasivas, que pasaron a estar disponibles al trabajo de las olas y corrientes luego del repentino alzamiento cosísmico.
- Sedimentos procedentes de deslizamientos subaéreos gatillados por el sacudimiento del sísmico.
- Movilización y depositación de arenas por transporte eólico.

Este proceso de progradación se ha mantenido a pesar que ISM se ha estado hundiendo a una tasa de ~25 mm/año, superior a la de antes del terremoto, de acuerdo a la estación GNSS permanente STAM.

Pocos estudios geomorfoloógicos han analizado y monitoroeado detalladamente la respuesta de la costa a la deformación provocada por terremotos. La mayoría de ellos se enfocan en costas que se han hundido cosísmicamente. Por ejemplo, luego del terremoto de Chile en 2010 (Martínez *et al.*, 2015; Martínez *et al.*, 2021), de Tohoku en 2011 (Tappin *et al.*, 2012) y de Sumatra-Andaman en 2004 (Choowong *et al.*, 2009; Liew *et al.*, 2010; Monecke *et al.*, 2017). En los pocos casos que se ha estudiado el efecto del levantamiento, en Sumatra-Andamán (Rajendran *et al.*, 2007), Chile (Jaramillo *et al.*, 2012; Martínez *et al.*, 2015) y Nueva Zelanda (MacDonald *et al.*, 2021), la evidencia es limitada y el monitoreo abarca periodos más cortos que una década. De este modo, los resultados presentados contribuyen a mejorar la comprensión de los procesos costeros asociados tanto al ciclo sísmico, como al levantamiento cosísmico de escala métrica. Además, al tratarse de un monitoreo de largo plazo (décadas) proporciona una descripción robusta de dichos procesos.

4.2. Cordones litorales como registro de ciclos sísmicos pasados

Previamente, Bookhagen *et al.* (2006) interpretó los cordones litorales de ISM como bermas abandonadas que representan las últimas tormentas antes del levantamiento cosísmico asociado a grandes terremotos pasados. Sin embargo, los resultados de esta tesis (ver Capítulo

2) muestran que la berma levantada cosísmicamente en 2010 fue rápidamente erosionada en los años posteriores al terremoto. De este modo, se propone un modelo conceptual diferente para explicar la construcción de los cordones litorales de ISM. Su construcción habría sido continua a través del Holoceno tardía y estaría controlada tanto por el levantamiento cosísmico, de terremotos pasados, como también por la lenta subsidencia intersísmica. Los datos de GPR y el análisis de la estratigrafía respaldan esta interpretación al mostrar sólo señales de progradación a través de la planicie sin evidencia conspicua de truncamiento estratigráfico (Capítulo 3). Así, se descartan períodos de erosión prolongada.

Considerando que la morfología de "beach ridge" y "runnel" fue progresivamente sepultada desde al menos 1941, es decir durante la última etapa del período intersísmico 1835-2010, se interpreta que dicha morfología se desarrolla y conserva como un ridge (o cordón litoral) y un "swale", durante el periodo entre grandes terremotos. A diferencia de lo propuesto por Bookhagen *et al.* (2006), en que cada cordón es un registro de levantamiento cosísmico, en este trabajo se propone que cada secuencia "ridge/swale" es producto de un ciclo sísmico completo, abarcando el co- y el intersísmico. De este modo, el intervalo temporal entre la construcción de cada secuencia adyacente correspondería a un proxy de la recurrencia de terremotos. Debido a la localización de ISM, alejada de las principales fuentes de sedimentos continentales, se propone que los cambios relativos del nivel del mar, asociados al ciclo sísmico, y el suministro local de arena desde la playa sumergida, junto a los sedimentos producidos por la erosión de los acantilados activos han controlado la construcción progresiva de los cordones litorales de la planicie de ISM.

4.3. Periodicidad de grandes terremotos en la Isla Santa María

Se propone, en base a los efectos asociados al terremoto de 2010, que la topografía, estratigrafía y geocronología de las secuencias de "ridge-swale" de ISM corresponde a un proxy de los ciclos sísmicos de los últimos 4500 años (Capítulo 3). Durante ese período se observa

que la temporalidad de cada ciclo ha variado. Es posible identificar al menos tres etapas con distintos rangos de intervalos de recurrencia:

- *Etapa I (4400 – 3000 años BP):* Recurrencia de 214 ± 75 años
- *Etapa II (2900 – 1800 años BP):* Recurrencia de 65 ± 22 años
- *Etapa III (1700 – 600 años BP):* Recurrencia de 243 ± 55 años

Esta variabilidad en el tiempo de recurrencia sísmica se observa también en el corto registro histórico de terremotos de este segmento. Entre 1570 y 1835 los terremotos ocurrieron periódicamente cada 88 ± 5 años en 1570, 1657, 1751 y 1835, mientras que entre 1835 y el evento de 2010 el rango temporal se duplicó a 175 años. El primer rango de recurrencia es muy similar a la Etapa II (65 ± 22 años), sin embargo entre 2900 y 2300 incluye 8 intervalos con una recurrencia media más corta, de 43 a 62 años. Las Etapa I (214 ± 75 años) y III (243 ± 55 años) se caracterizan por rangos de recurrencia más largos, incluso mayores al último ciclo símico 1835-2010. La magnitud de estos intervalos, comparables al registro histórico y geológico (Dura *et al.*, 2017) , junto con su variabilidad progresiva y continua (no estocástica) respaldan esta interpretación. Se destaca que tanto la recurrencia histórica como nuestros datos alternan entre valores cortos (<100 años) y largos (~200 años).

Debido a que los intervalos de recurrencia no son constantes a lo largo del tiempo en ISM, se sugiere que el segmento del Maule presenta un comportamiento sísmico débilmente periódico con cambios a escala de siglos. Variabilidad en el rango de tiempo entre terremotos también ha sido reportada en otras zonas de subducción como Cascadia, Sumatra y Tohoku (Kelsey *et al.*, 2005; Sieh *et al.*, 2008; Goldfinger *et al.*, 2013; Satake, 2015; Rubin *et al.*, 2017; Moernaut, 2020). La Etapa II es notable pues presenta una agrupación temporal de eventos (“clustered earthquakes”), fenómeno que también ha sido reportado en las zonas de Cascadia (Kelsey *et al.*, 2005; Goldfinger *et al.*, 2013) y Sumatra (Philibosian *et al.*, 2017).

4.4. Recurrencia sísmica en los segmentos del Maule y Valdivia

El comportamiento sísmico del segmento del Maule difiere de la recurrencia más constante y periódica del segmento de Valdivia. Esto se traducen en valores diferentes de Coeficiente de Variación (CoV), "Burstiness" (B) y Memoria (M) entre ambas zonas (Capítulo 3). En resumen, el análisis de las distintas etapas sísmicas inferidas en ISM confirman un comportamiento débilmente periódico general para toda la secuencia de 4500 años. Sin embargo, dentro de cada etapa reconocida la recurrencia tiende a ser más períodica. Por el contrario, el segmento de Valdivia se caracteriza por una recurrencia más estable, en que grandes terremotos (Mw > 8.6) ocurren en promedio cada 292 ± 93 años, mientras que terremotos menores (Mw 7.7-8.5) cada 139 ± 69 años (Cisternas *et al.*, 2005; Kempf *et al.*, 2017; Moernaut *et al.*, 2018).

Las diferencias en la recurrencia sísmica entre los segmentos del Maule y Valdivia podrían ser explicados por aspectos secundarios de la subducción más que por la geometría y reología general que es similar en ambos segmentos. Estas factores corresponden principalmente a la dinámica de los sedimentos, tanto subductados acrecionados, la fricción basal entre placas y la deformación de la placa superior por fallas corticales (ver Capítulo 3). El Maule está caracterizado por la acreción frontal de sedimentos, fallamiento inverso en la cordillera principal, como la "West Andean Thrust Fault", fallas costeras activas y "splay faults". En cambio el segmento de Valdivia cuenta con una mayor cantidad de sedimentos que son acrecionados basalmente y se observa fallamiento de rumbo en el arco volcánico (Sistema de Fallas Liquiñe-Ofqui) y fallas selladas e inactivas en el antearco (Echaurren *et al.*, 2022). En la presente tesis se propone que tales diferencias explicarían las diferencias en los periodos de recurrencia reportados para el segmento de Valdivia (Cisternas *et al.*, 2005; Kempf *et al.*, 2017; Moernaut *et al.*, 2018) y para el Maule (este trabajo).

4.5. Implicancias y perspectivas

En este trabajo se destaca la importancia del monitoreo a escala de décadas en los ambientes costeros de márgenes activos. Se ha demostrado en el Capítulo 2 que no sólo la abrupta deformación cosísmica genera cambios en la geomorfología, sino que también a lo largo del período intersísmico y postsísmico existen procesos sedimentarios importantes que determinan la evolución de dichos sistemas. El trabajo realizado en ISM muestra además cómo a través de la comprensión de los procesos costeros asociados al ciclo sísmico es posible interpretar rasgos geomorfológicos y estratigráficos que registran la ocurrencia de grandes terremotos pasados a escala de miles de años.

Considerando los presentes resultados y los distintos estudios a escala global, se desprende la necesidad de contar con registros paleosismológicos de largo término, que cuenten con geocronologías robustas, pues la variabilidad en la recurrencia de terremotos es alta en los márgenes de subducción. Registros milenarios, con más de 10 eventos pueden dar cuenta de un comportamiento periódico de terremotos como ha sido el caso de la zona de Valdivia, o más bien patrones de recurrencia débilmente periódicos como es el caso del Maule. Se enfatiza también la necesidad de profundizar acerca del posible control de las características secundarias del margen tectónico sobre la recurrencia de grandes terremotos. Además del estudio de las geomorfologías costeras basculadas como proxies de la activación de “splay faults”, que eventualmente acompañan a frandes terremotos de subducción (Capítulo 3). Finalmente, se recomienda que trabajos futuros, en zonas costeras tectónicamente activas, estudien los sistemas con cordones litorales holocenos como indicadores de la deformación tectónica y paleosismológica.

CAPÍTULO V. Conclusiones

- El monitoreo durante ocho décadas de la costa en ISM reveló cambios morfológicos significativos relacionados con cada una de las distintas fases del ciclo sísmico, incluyendo siete décadas de subsidencia intersísmica (~11 mm/año), el levantamiento cosísmico abrupto de 1.8 metros en 2010 y una década de subsidencia postsísmica (~25 mm/año).

- Durante la fase intersísmica anterior al terremoto de 2010, la costa registró un avance gradual (< 1 m/año). Durante este periodo, el sistema intermareal compuesto por “beach ridge” y “runnel” quedó sepultado por una duna frontal. Por otra parte, la fase cosísmica resultó en un rápido avance y elevación de la playa. Tras el terremoto, rápidamente se forma una nueva berma y la costa continúa avanzando a tasas mayores (~3 m/año), a pesar de la subsidencia.

- La progradación y construcción de la planicie costera con 24 cordones litorales se ha producido continuamente durante la deformación asociada al levantamiento cosísmico y al hundimiento intersísmico. Por lo tanto, estos cordones litorales y "swales" son el resultado de cambios en el nivel relativo del mar durante ciclos sísmicos completos y representan un registro continuo de los ciclos sísmicos durante los últimos 4500 años.

- Se identificaron tres etapas: La Etapa I (4400 - 3000 años antes del presente), con una recurrencia de 214 ± 75 años, la Etapa II (2900 - 1800 años antes del presente), con una recurrencia de 65 ± 22 años, y por último, la Etapa III (1700 - 600 años antes del presente), con una recurrencia de 243 ± 55 años. Las variaciones en estos intervalos de recurrencia, y en el registro histórico, alternan entre valores cortos (<100 años) y largos (~200 años), sugiriendo patrones dinámicos en la duración de los ciclos sísmicos del segmento del Maule.

- Los intervalos de recurrencia en ISM muestran un comportamiento débilmente periódico en el Maule, en contraste con la recurrencia más constante del segmento vecino de Valdivia. Las diferencias en la deformación de la placa superior, la acreción de sedimentos y la fricción entre placas pueden explicar la variación en la tasa de recurrencia y el comportamiento sísmico.

- Este estudio subraya la importancia del monitoreo costero a largo plazo en márgenes tectónicos activos, ya que la comprensión de los efectos asociados al ciclo sísmico permite interpretar los rasgos geomorfológicos y estratigráficos que potencialmente registran grandes terremotos pasados. Los resultados enfatizan la necesidad de registros paleosismológicos extensos para estimar la recurrencia y probabilidad de grandes terremotos y contribuir al desarrollo de modelos más precisos en el futuro.

REFERENCIAS

Aedo, D., Cisternas, M., Melnick, D., Esparza, C., Winckler, P., & Saldaña, B. (2023). Decadal coastal evolution spanning the 2010 Maule earthquake at Isla Santa Maria, Chile: Framing Darwin's accounts of uplift over a seismic cycle. *Earth Surface Processes and Landforms*, *48*(12), 2319-2333. https://doi.org/https://doi.org/10.1002/esp.5615

Anthony, E. J., & Aagaard, T. (2020). The lower shoreface: Morphodynamics and sediment connectivity with the upper shoreface and beach. *Earth-Science Reviews*, *210*, 103334. https://doi.org/https://doi.org/10.1016/j.earscirev.2020.103334

Ardhuin, F., Rogers, E., Babanin, A. V., Filipot, J.-F., Magne, R., Roland, A., van der Westhuysen, A., Queffeulou, P., Lefevre, J.-M., Aouf, L., & Collard, F. (2010). Semiempirical Dissipation Source Functions for Ocean Waves. Part I: Definition, Calibration, and Validation. *Journal of Physical Oceanography*, *40*(9), 1917-1941. https://doi.org/10.1175/2010JPO4324.1

Atwater, B. F., Satoko, M.-R., Kenji, S., Yoshinobu, T., Kazue, U., & Yamaguchi, D. K. (2005). *The Orphan Tsunami of 1700 Japanese Clues to a Parent Earthquake in North America* (2 ed.). University of Washington Press. http://www.jstor.org/stable/j.ctvcwnbrv

Bangs, N. L., Morgan, J. K., Tréhu, A. M., Contreras-Reyes, E., Arnulf, A. F., Han, S., Olsen, K. M., & Zhang, E. (2020). Basal Accretion Along the South Central Chilean Margin and Its Relationship to Great Earthquakes. *Journal of Geophysical Research: Solid Earth*, *125*(11), e2020JB019861. https://doi.org/https://doi.org/10.1029/2020JB019861

Barnard, P. L., Hoover, D., Hubbard, D. M., Snyder, A., Ludka, B. C., Allan, J., Kaminsky, G. M., Ruggiero, P., Gallien, T. W., Gabel, L., McCandless, D., Weiner, H. M., Cohn, N., Anderson, D. L., & Serafin, K. A. (2017). Extreme oceanographic forcing and coastal response due to the 2015–2016 El Niño. *Nature Communications*, *8*(1), 14365. https://doi.org/10.1038/ncomms14365

Bassett, D., Sandwell, D. T., Fialko, Y., & Watts, A. B. (2016). Upper-plate controls on co-seismic slip in the 2011 magnitude 9.0 Tohoku-oki earthquake. *Nature*, *531*(7592), 92-96. https://doi.org/10.1038/nature16945

Bernhardt, A., Melnick, D., Jara-Muñoz, J., Argandoña, B., González, J., & Strecker, M. R. (2015). Controls on submarine canyon activity during sea-level highstands: The Biobío canyon system offshore Chile. *Geosphere*, *11*(4), 1226-1255. https://doi.org/10.1130/ges01063.1

Bevis, M., & Brown, A. (2014). Trajectory models and reference frames for crustal motion geodesy. *Journal of Geodesy*, *88*(3), 283-311. https://doi.org/10.1007/s00190-013-0685-5

Beya, J., Álvarez, M., Gallardo, A., Hidalgo, H., & Winckler, P. (2017). Generation and validation of the Chilean Wave Atlas database. *Ocean Modelling*, *116*. https://doi.org/10.1016/j.ocemod.2017.06.004

Bookhagen, B., Echtler, H. P., Melnick, D., Strecker, M. R., & Spencer, J. Q. G. (2006). Using uplifted Holocene beach berms for paleoseismic analysis on the Santa María Island, south-central Chile [https://doi.org/10.1029/2006GL026734]. *Geophysical Research Letters*, *33*(15). https://doi.org/https://doi.org/10.1029/2006GL026734

Brill, D., & Cisternas, M. (2020). Testing quartz and feldspar luminescence dating to determine earthquake and tsunami recurrence in the area of the giant 1960 Chile earthquake. *Quaternary Geochronology*, *58*, 101080. https://doi.org/https://doi.org/10.1016/j.quageo.2020.101080

Brill, D., May, S. M., Shah-Hosseini, M., Rufer, D., Schmidt, C., & Engel, M. (2017). Luminescence dating of cyclone-induced washover fans at Point Lefroy (NW Australia). *Quaternary Geochronology*, *41*, 134-150. https://doi.org/https://doi.org/10.1016/j.quageo.2017.03.004

Bristow, C. S., & Pucillo, K. (2006). Quantifying rates of coastal progradation from sediment volume using GPR and OSL: the Holocene fill of Guichen Bay, south-east South Australia [https://doi.org/10.1111/j.1365-3091.2006.00792.x]. *Sedimentology*, *53*(4), 769-788. https://doi.org/https://doi.org/10.1111/j.1365-3091.2006.00792.x

Bronk Ramsey, C. (2009). Bayesian Analysis of Radiocarbon Dates. *Radiocarbon*, *51*(1), 337-360. https://doi.org/10.1017/S0033822200033865

Bronk Ramsey, C. (2021). *OxCal Project, Version 4.4.4*. https://c14.arch.ox.ac.uk/oxcal/

Brooke, B., Ryan, D., Pietsch, T., Olley, J., Douglas, G., Packett, R., Radke, L., & Flood, P. (2008). Influence of climate fluctuations and changes in catchment land use on Late Holocene and modern beach-ridge sedimentation on a tropical macrotidal coast: Keppel Bay, Queensland, Australia. *Marine Geology*, *251*(3), 195-208. https://doi.org/https://doi.org/10.1016/j.margeo.2008.02.013

Brooke, B. P., Pietsch, T. J., Olley, J. M., Sloss, C. R., & Cox, M. E. (2015). A preliminary OSL chronology for coastal dunes on Moreton island, Queensland, Australia – Marginal deposits of A large-scale quaternary shelf sediment system. *Continental Shelf Research*, *105*, 79-94. https://doi.org/https://doi.org/10.1016/j.csr.2015.06.002

Bruun, P. (1962). Sea-Level Rise as a Cause of Shore Erosion. *Journal of the Waterways and Harbors Division*, *88*(1), 117-130. https://doi.org/doi:10.1061/JWHEAU.0000252

Casella, E., Drechsel, J., Winter, C., Benninghoff, M., & Rovere, A. (2020). Accuracy of sand beach topography surveying by drones and photogrammetry. *Geo-Marine Letters*, *40*(2), 255-268. https://doi.org/10.1007/s00367-020-00638-8

Choowong, M., Phantuwongraj, S., Charoentitirat, T., Chutakositkanon, V., Yumuang, S., & Charusiri, P. (2009). Beach recovery after 2004 Indian Ocean tsunami from Phang-nga, Thailand. *Geomorphology*, *104*(3), 134-142. https://doi.org/https://doi.org/10.1016/j.geomorph.2008.08.007

Cisternas, M., Atwater, B. F., Torrejón, F., Sawai, Y., Machuca, G., Lagos, M., Eipert, A., Youlton, C., Salgado, I., Kamataki, T., Shishikura, M., Rajendran, C. P., Malik, J. K., Rizal, Y., & Husni, M. (2005). Predecessors of the giant 1960 Chile earthquake. *Nature*, *437*(7057), 404-407. https://doi.org/10.1038/nature03943

Cisternas, M., Mizobe, C., Wesson, R., Ely, L., Muñoz, A., Dura, T., Valdebenito, G., & Melnick, D. (2017). *Beach Ridges, Buried Erosional Scarps and Overhanging Soils Evidence Recurring Past Co-seismic Subsidence Midway Along the Area of the Giant 1960 Chile Earthquake*. https://doi.org/10.1130/abs/2017AM-302380

Contreras-Reyes, E., Flueh, E. R., & Grevemeyer, I. (2010). Tectonic control on sediment accretion and subduction off south central Chile: Implications for coseismic rupture

processes of the 1960 and 2010 megathrust earthquakes. *Tectonics*, *29*(6). https://doi.org/https://doi.org/10.1029/2010TC002734

Darwin, C. (1839). Narrative of the Surveying Voyages of His Majesty's Ships Adventure and Beagle, Between the Years 1826 and 1836: Journal and Remarks, 1832–1836 Vol. 3. *Henry Colburn*.

Darwin, C. (1846). Geological observations on South America. Being the third part of the geology of the voyage of the Beagle, under the command of Capt. Fitzroy, R.N. during the years 1832 to 1836. *Smith Elder and Co*.

Davies, J. L. (1974). The coastal sediment compartment. *Australian Geographical Studies*, *12*(2), 139-151. https://doi.org/https://doi.org/10.1111/j.1467-8470.1974.tb00270.x

Dickson, M. E., Omidiji, J., Litchfield, N. J., Norton, K. P., Matsumoto, H., Krier-Mariani, R. L., Horton, S. L., Acharya-Chowdhury, L., McLean, A. D., Hurst, M. D., & Stephenson, W. J. (2022). Observations of the incipient and penultimate stages of Holocene marine terrace development. *Earth Surface Processes and Landforms*, *47*(13), 3019-3032. https://doi.org/https://doi.org/10.1002/esp.5440

Dura, T., Horton, B. P., Cisternas, M., Ely, L. L., Hong, I., Nelson, A. R., Wesson, R. L., Pilarczyk, J. E., Parnell, A. C., & Nikitina, D. (2017). Subduction zone slip variability during the last millennium, south-central Chile. *Quaternary Science Reviews*, *175*, 112-137. https://doi.org/https://doi.org/10.1016/j.quascirev.2017.08.023

Durcan, J. A., King, G. E., & Duller, G. A. T. (2015). DRAC: Dose Rate and Age Calculator for trapped charge dating. *Quaternary Geochronology*, *28*, 54-61. https://doi.org/https://doi.org/10.1016/j.quageo.2015.03.012

Echaurren, A., Encinas, A., Sagripanti, L., Gianni, G., Zambrano, P., Duhart, P., & Folguera, A. (2022). Fore-to-retroarc crustal structure of the north Patagonian margin: How is shortening distributed in Andean-type orogens? *Global and Planetary Change*, *209*, 103734. https://doi.org/https://doi.org/10.1016/j.gloplacha.2022.103734

Egbert, G. D., & Erofeeva, S. Y. (2002). Efficient Inverse Modeling of Barotropic Ocean Tides. *Journal of Atmospheric and Oceanic Technology*, *19*(2), 183-204. https://doi.org/10.1175/1520-0426(2002)019<0183:EIMOBO>2.0.CO;2

Ely, L. L., Cisternas, M., Wesson, R. L., & Dura, T. (2014). Five centuries of tsunamis and land-level changes in the overlapping rupture area of the 1960 and 2010 Chilean earthquakes. *Geology*, *42*(11), 995-998. https://doi.org/10.1130/g35830.1

FitzRoy, R. (1839). Narrative of the Surveying Voyages of his Majesty's Ships Adventure and Beagle, Between the Years 1826 and 1836, Proceedings of the Second Expedition, 1831–1836 Vol. 2. *Henry Colburn*.

Galbraith, R. F., Roberts, R. G., Laslett, G. M., Yoshida, H., & Olley, J. M. (1999). Optical dating of single and multiple grains of quartz from Jinmium rock shelter, northern Australia: Part I, experimental design and statistical models. *Archaeometry*, *41*(2), 339-364. https://doi.org/https://doi.org/10.1111/j.1475-4754.1999.tb00987.x

Gao, X., & Wang, K. (2017). Rheological separation of the megathrust seismogenic zone and episodic tremor and slip. *Nature*, *543*(7645), 416-419. https://doi.org/10.1038/nature21389

Geersen, J., Behrmann, J. H., Völker, D., Krastel, S., Ranero, C. R., Diaz-Naveas, J., & Weinrebe, W. (2011). Active tectonics of the South Chilean marine fore arc (35°S–40°S). *Tectonics*, *30*(3). https://doi.org/https://doi.org/10.1029/2010TC002777

Goff, J., & Sugawara, D. (2014). Seismic-driving of sand beach ridge formation in northern Honshu, Japan? *Marine Geology*, *358*, 138-149. https://doi.org/https://doi.org/10.1016/j.margeo.2014.04.005

Goh, K. I., & Barabási, A. L. (2008). Burstiness and memory in complex systems. *Europhysics Letters*, *81*(4), 48002. https://doi.org/10.1209/0295-5075/81/48002

Goldfinger, C., Galer, S., Beeson, J., Hamilton, T., Black, B., Romsos, C., Patton, J., Nelson, C. H., Hausmann, R., & Morey, A. (2017). The importance of site selection, sediment supply, and hydrodynamics: A case study of submarine paleoseismology on the northern Cascadia margin, Washington USA. *Marine Geology*, *384*, 4-46. https://doi.org/https://doi.org/10.1016/j.margeo.2016.06.008

Goldfinger, C., Ikeda, Y., Yeats, R. S., & Ren, J. (2013). Superquakes and Supercycles. *Seismological Research Letters*, *84*(1), 24-32. https://doi.org/10.1785/0220110135

Goldfinger, C., Nelson, C., Morey, A., Johnson, J., Patton, J., Karabanov, E., Gutiérrez-Pastor, J., Eriksson, A., Gràcia, E., Dunhill, G., Enkin, R., Dallimore, A., & Vallier, T. (2012). Turbidite event history—Methods and implications for Holocene paleoseismicity of the Cascadia subduction zone. *USGS professional paper*, *1661-F*, 184 pp.

Gonçalves, J. A., & Henriques, R. (2015). UAV photogrammetry for topographic monitoring of coastal areas. *ISPRS Journal of Photogrammetry and Remote Sensing*, *104*, 101-111. https://doi.org/https://doi.org/10.1016/j.isprsjprs.2015.02.009

GSSI. (2017). RADAN 7 Manual. https://www.geophysical.com/wp-content/uploads/2017/2010/GSSI-RADAN-2017-Manual.pdf. https://www.geophysical.com/wp-content/uploads/2017/10/GSSI-RADAN-7-Manual.pdf

Harley, M. D., Turner, I. L., Kinsela, M. A., Middleton, J. H., Mumford, P. J., Splinter, K. D., Phillips, M. S., Simmons, J. A., Hanslow, D. J., & Short, A. D. (2017). Extreme coastal erosion enhanced by anomalous extratropical storm wave direction. *Scientific Reports*, *7*(1), 6033. https://doi.org/10.1038/s41598-017-05792-1

Hasselmann, S., & Hasselmann, K. (1985). Computations and Parameterizations of the Nonlinear Energy Transfer in a Gravity-Wave Spectrum. Part I: A New Method for Efficient Computations of the Exact Nonlinear Transfer Integral. *Journal of Physical Oceanography*, *15*(11), 1369-1377. https://doi.org/10.1175/1520-0485(1985)015<1369:CAPOTN>2.0.CO;2

Heaton, T. J., Köhler, P., Butzin, M., Bard, E., Reimer, R. W., Austin, W. E. N., Bronk Ramsey, C., Grootes, P. M., Hughen, K. A., Kromer, B., Reimer, P. J., Adkins, J., Burke, A., Cook, M. S., Olsen, J., & Skinner, L. C. (2020). Marine20—The Marine Radiocarbon Age Calibration Curve (0–55,000 cal BP). *Radiocarbon*, *62*(4), 779-820. https://doi.org/10.1017/RDC.2020.68

Herrendörfer, R., van Dinther, Y., Gerya, T., & Dalguer, L. A. (2015). Earthquake supercycle in subduction zones controlled by the width of the seismogenic zone. *Nature Geoscience*, *8*(6), 471-474. https://doi.org/10.1038/ngeo2427

Hesp, P. A. (2013). Conceptual models of the evolution of transgressive dune field systems. *Geomorphology*, *199*, 138-149. https://doi.org/https://doi.org/10.1016/j.geomorph.2013.05.014

Hesp, P. A., DaSilva, M., Miot da Silva, G., Bruce, D., & Keane, R. (2022). Review and direct evidence of transgressive aeolian sand sheet and dunefield initiation [https://doi.org/10.1002/esp.5400]. *Earth Surface Processes and Landforms*, *47*(11), 2660-2675. https://doi.org/https://doi.org/10.1002/esp.5400

Hollingsworth, J., Ye, L., & Avouac, J.-P. (2017). Dynamically triggered slip on a splay fault in the Mw 7.8, 2016 Kaikoura (New Zealand) earthquake. *Geophysical Research Letters*, *44*(8), 3517-3525. https://doi.org/https://doi.org/10.1002/2016GL072228

Huntley, D. J., & Baril, M. R. (1997). The K content of the K-feldspars being measured in optical dating or in thermoluminescence dating.

Huntley, D. J., & Lamothe, M. (2001). Ubiquity of anomalous fading in K-feldspars and the measurement and correction for it in optical dating. *Canadian Journal of Earth Sciences*, *38*(7), 1093-1106. https://doi.org/10.1139/e01-013

Ingram, B. L., & Southon, J. R. (1996). Reservoir Ages in Eastern Pacific Coastal and Estuarine Waters. *Radiocarbon*, *38*(3), 573-582. https://doi.org/10.1017/S0033822200030101

Jara-Muñoz, J., & Melnick, D. (2015). Unraveling Sea-Level Variations and Tectonic Uplift in Wave-Built Marine Terraces, Santa María Island, Chile. *Quaternary Research*, *83*(1), 216-228. https://doi.org/10.1016/j.yqres.2014.10.002

Jara-Muñoz, J., Melnick, D., Li, S., Socquet, A., Cortés-Aranda, J., Brill, D., & Strecker, M. (2022). The cryptic seismic potential of the Pichilemu blind fault in Chile revealed by off-fault geomorphology. *Nature Communications*, *13*. https://doi.org/10.1038/s41467-022-30754-1

Jara-Muñoz, J., Melnick, D., Zambrano, P., Rietbrock, A., González, J., Argandoña, B., & Strecker, M. R. (2017). Quantifying offshore fore-arc deformation and splay-fault slip using drowned Pleistocene shorelines, Arauco Bay, Chile [https://doi.org/10.1002/2016JB013339]. *Journal of Geophysical Research: Solid Earth*, *122*(6), 4529-4558. https://doi.org/https://doi.org/10.1002/2016JB013339

Jaramillo, E., Dugan, J. E., Hubbard, D. M., Melnick, D., Manzano, M., Duarte, C., Campos, C., & Sanchez, R. (2012). Ecological Implications of Extreme Events: Footprints of the 2010 Earthquake along the Chilean Coast. *PLOS ONE*, *7*(5), e35348. https://doi.org/10.1371/journal.pone.0035348

Julve, J., Barbot, S., Moreno, M., Tassara, A., Araya, R., Catalán, N., Crempien, J., & Becerra, V. (2023). *Size and timing of giant Chilean earthquake controlled by rock composition and forearc structure*. https://doi.org/10.21203/rs.3.rs-2503201/v1

Kelsey, H. M., Nelson, A. R., Hemphill-Haley, E., & Witter, R. C. (2005). Tsunami history of an Oregon coastal lake reveals a 4600 yr record of great earthquakes on the Cascadia subduction zone. *GSA Bulletin*, *117*(7-8), 1009-1032. https://doi.org/10.1130/b25452.1

Kempf, P., & Moernaut, J. (2021). Age Uncertainty in Recurrence Analysis of Paleoseismic Records. *Journal of Geophysical Research: Solid Earth*, *126*(8), e2021JB021996. https://doi.org/https://doi.org/10.1029/2021JB021996

Kempf, P., Moernaut, J., Van Daele, M., Vandoorne, W., Pino, M., Urrutia, R., & De Batist, M. (2017). Coastal lake sediments reveal 5500 years of tsunami history in south central Chile. *Quaternary Science Reviews*, *161*, 99-116. https://doi.org/https://doi.org/10.1016/j.quascirev.2017.02.018

King, C. A. M., & Williams, W. W. (1949). The Formation and Movement of Sand Bars by Wave Action. *The Geographical Journal*, *113*, 70-85. https://doi.org/10.2307/1788907

King, P. P. (1839). *Narrative of the Surveying Voyages of His Majesty's Ships Adventure and Beagle: Between the Years 1826 and 1836* (Vol. 3). H. Colburn.

Kölbl-Ebert, M. (1999). Observing orogeny — Maria Graham's account of the earthquake in Chile in 1822. *International Union of Geological Sciences*, *22*(1), 36-40. https://doi.org/10.18814/epiiugs/1999/v22i1/006

Kopp, H. (2013). Invited review paper: The control of subduction zone structural complexity and geometry on margin segmentation and seismicity. *Tectonophysics*, *589*, 1-16. https://doi.org/https://doi.org/10.1016/j.tecto.2012.12.037

Kreutzer, S., Burow, C., Dietze, M., Fuchs, M. C., Schmidt, C., Fischer, M., Friedrich, J., Mercier, N., Philippe, A., Riedesel, S., Autzen, M., Mittelstrass, D., Gray, H. J., &

Galharret, J.-M. (2023). *Luminescence: Comprehensive Luminescence Dating Data Analysis*. https://CRAN.R-project.org/package=Luminescence

Kreutzer, S., Schmidt, C., DeWitt, R., & Fuchs, M. (2014). The a-value of polymineral fine grain samples measured with the post-IR IRSL protocol. *Radiation Measurements*, *69*, 18-29. https://doi.org/https://doi.org/10.1016/j.radmeas.2014.04.027

Li, S., Moreno, M., Rosenau, M., Melnick, D., & Oncken, O. (2014). Splay fault triggering by great subduction earthquakes inferred from finite element models. *Geophysical Research Letters*, *41*(2), 385-391. https://doi.org/https://doi.org/10.1002/2013GL058598

Lieser, K., Grevemeyer, I., Lange, D., Flueh, E., Tilmann, F., & Contreras-Reyes, E. (2014). Splay fault activity revealed by aftershocks of the 2010 Mw 8.8 Maule earthquake, central Chile. *Geology*, *42*(9), 823-826. https://doi.org/10.1130/g35848.1

Liew, S. C., Gupta, A., Wong, P. P., & Kwoh, L. K. (2010). Recovery from a large tsunami mapped over time: The Aceh coast, Sumatra. *Geomorphology*, *114*(4), 520-529. https://doi.org/https://doi.org/10.1016/j.geomorph.2009.08.010

Lomnitz, C. (1970). Major earthquakes and tsunamis in Chile during the period 1535 to 1955 [Article]. *Geologische Rundschau*, *59*(3), 938-960. https://doi.org/10.1007/BF02042278

Luijendijk, A., Hagenaars, G., Ranasinghe, R., Baart, F., Donchyts, G., & Aarninkhof, S. (2018). The State of the World's Beaches. *Scientific Reports*, *8*(1), 6641. https://doi.org/10.1038/s41598-018-24630-6

MacDonald, K. E., Hart, D. E., & Pitman, S. J. (2021). Geomorphic responses of uplifted mixed sand and gravel beaches: combining short-term observations from Kaikōura, New Zealand with longer-term evidence. *New Zealand Journal of Geology and Geophysics*, 1-16. https://doi.org/10.1080/00288306.2021.1994425

Madsen, A., Buylaert, J.-P., & Murray, A. (2011). Luminescence dating of young coastal deposits from New Zealand using feldspar. *Geochronometria*, *38*(4), 379-390. https://doi.org/doi:10.2478/s13386-011-0042-5

Maksymowicz, A. (2015). The geometry of the Chilean continental wedge: Tectonic segmentation of subduction processes off Chile. *Tectonophysics*, *659*, 183-196. https://doi.org/https://doi.org/10.1016/j.tecto.2015.08.007

Maksymowicz, A., Contreras-Reyes, E., Díaz, D., Comte, D., Bangs, N., Tréhu, A. M., Vera, E., Hervé, F., & Rietbrock, A. (2021). Deep Structure of the Continental Plate in the South-Central Chilean Margin: Metamorphic Wedge and Implications for Megathrust Earthquakes. *Journal of Geophysical Research: Solid Earth*, *126*(7), e2021JB021879. https://doi.org/https://doi.org/10.1029/2021JB021879

Maldonado, V., Contreras, M., & Melnick, D. (2021). A comprehensive database of active and potentially-active continental faults in Chile at 1:25,000 scale. *Scientific Data*, *8*(1), 20. https://doi.org/10.1038/s41597-021-00802-4

Martínez, C., Grez, P. W., Martín, R. A., Acuña, C. E., Torres, I., & Contreras-López, M. (2021). Coastal erosion in sandy beaches along a tectonically active coast: The Chile study case. *Progress in Physical Geography: Earth and Environment*, *46*(2), 250-271. https://doi.org/10.1177/03091333211057194

Martínez, C., Rojas, D., Quezada, M., Quezada, J., & Oliva, R. (2015). Post-earthquake coastal evolution and recovery of an embayed beach in central-southern Chile. *Geomorphology*, *250*, 321-333. https://doi.org/https://doi.org/10.1016/j.geomorph.2015.09.015

Massel, S. R. (1996). *Ocean Surface Waves: Their Physics and Prediction*. https://doi.org/10.1142/2285

Masselink, G., Castelle, B., Scott, T., Dodet, G., Suanez, S., Jackson, D., & Floc'h, F. (2016). Extreme wave activity during 2013/2014 winter and morphological impacts along the Atlantic coast of Europe. *Geophysical Research Letters*, *43*(5), 2135-2143. https://doi.org/https://doi.org/10.1002/2015GL067492

McSaveney, M. J., Graham, I. J., Begg, J. G., Beu, A. G., Hull, A. G., Kim, K., & Zondervan, A. (2006). Late Holocene uplift of beach ridges at Turakirae Head, south Wellington coast, New Zealand. *New Zealand Journal of Geology and Geophysics*, *49*(3), 337-358. https://doi.org/10.1080/00288306.2006.9515172

Meilianda, E., Dohmen-Janssen, C. M., Maathuis, B. H. P., Hulscher, S. J. M. H., & Mulder, J. P. M. (2010). Short-term morphological responses and developments of Banda Aceh coast, Sumatra Island, Indonesia after the tsunami on 26 December 2004. *Marine Geology*, *275*(1), 96-109. https://doi.org/https://doi.org/10.1016/j.margeo.2010.04.012

Melnick, D., Bookhagen, B., Echtler, H., & Strecker, M. (2006a). Coastal deformation and great subduction earthquakes, Isla Santa Mar??a, Chile (37 S). *Geological Society of America Bulletin*, *118*, 1463-1480. https://doi.org/10.1130/B25865

Melnick, D., Bookhagen, B., Echtler, H. P., & Strecker, M. R. (2006b). Coastal deformation and great subduction earthquakes, Isla Santa María, Chile (37°S). *GSA Bulletin*, *118*(11-12), 1463-1480. https://doi.org/10.1130/B25865.1

Melnick, D., Bookhagen, B., Strecker, M. R., & Echtler, H. P. (2009). Segmentation of megathrust rupture zones from fore-arc deformation patterns over hundreds to millions of years, Arauco peninsula, Chile. *Journal of Geophysical Research: Solid Earth*, *114*(B1). https://doi.org/https://doi.org/10.1029/2008JB005788

Melnick, D., Cisternas, M., Moreno, M., & Norambuena, R. (2012a). Estimating coseismic coastal uplift with an intertidal mussel: calibration for the 2010 Maule Chile earthquake (Mw = 8.8). *Quaternary Science Reviews*, *42*, 29-42. https://doi.org/https://doi.org/10.1016/j.quascirev.2012.03.012

Melnick, D., Moreno, M., Motagh, M., Cisternas, M., & Wesson, R. (2012b). Splay fault slip during the Mw 8.8 2010 Maule Chile earthquake: REPLY. *Geology*, *40*, 251-254. https://doi.org/10.1130/G34825Y.1

Melnick, D., Moreno, M., Motagh, M., Cisternas, M., & Wesson, R. L. (2012c). Splay fault slip during the Mw 8.8 2010 Maule Chile earthquake. *Geology*, *40*(3), 251-254. https://doi.org/10.1130/g32712.1

Melnick, D., Moreno, M., Quinteros, J., Baez, J. C., Deng, Z., Li, S., & Oncken, O. (2017). The super-interseismic phase of the megathrust earthquake cycle in Chile [https://doi.org/10.1002/2016GL071845]. *Geophysical Research Letters*, *44*(2), 784-791. https://doi.org/https://doi.org/10.1002/2016GL071845

Mentaschi, L., Vousdoukas, M. I., Pekel, J.-F., Voukouvalas, E., & Feyen, L. (2018). Global long-term observations of coastal erosion and accretion. *Scientific Reports*, *8*(1), 12876. https://doi.org/10.1038/s41598-018-30904-w

Meyers, R. A., Smith, D. G., Jol, H. M., & Peterson, C. D. (1996). Evidence for eight great earthquake-subsidence events detected with ground-penetrating radar, Willapa barrier, Washington. *Geology*, *24*(2), 99-102. https://doi.org/10.1130/0091-7613(1996)024<0099:EFEGES>2.3.CO;2

Moernaut, J. (2020). Time-dependent recurrence of strong earthquake shaking near plate boundaries: A lake sediment perspective. *Earth-Science Reviews*, *210*, 103344. https://doi.org/https://doi.org/10.1016/j.earscirev.2020.103344

Moernaut, J., Van Daele, M., Fontijn, K., Heirman, K., Kempf, P., Pino, M., Valdebenito, G., Urrutia, R., Strasser, M., & De Batist, M. (2018). Larger earthquakes recur more periodically: New insights in the megathrust earthquake cycle from lacustrine turbidite records in south-central Chile. *Earth and Planetary Science Letters*, *481*, 9-19. https://doi.org/https://doi.org/10.1016/j.epsl.2017.10.016

Molina, D., Tassara, A., Abarca-del-Rio, R., Melnick, D., & Madella, A. (2021). Frictional Segmentation of the Chilean Megathrust From a Multivariate Analysis of Geophysical, Geological, and Geodetic Data. *Journal of Geophysical Research: Solid Earth*, *126*. https://doi.org/10.1029/2020JB020647

Monecke, K., Meilianda, E., Walstra, D.-J., Hill, E. M., McAdoo, B. G., Qiu, Q., Storms, J. E. A., Masputri, A. S., Mayasari, C. D., Nasir, M., Riandi, I., Setiawan, A., & Templeton, C. K. (2017). Postseismic coastal development in Aceh, Indonesia - Field observations and numerical modeling. *Marine Geology*, *392*, 94-104. https://doi.org/https://doi.org/10.1016/j.margeo.2017.07.012

Monecke, K., Templeton, C. K., Finger, W., Houston, B., Luthi, S., McAdoo, B. G., Meilianda, E., Storms, J. E. A., Walstra, D.-J., Amna, R., Hood, N., Karmanocky, F. J., Nurjanah, Rusydy, I., & Sudrajat, S. U. (2015). Beach ridge patterns in West Aceh, Indonesia, and their response to large earthquakes along the northern Sunda trench. *Quaternary Science Reviews*, *113*, 159-170. https://doi.org/https://doi.org/10.1016/j.quascirev.2014.10.014

Moore, L. J. (2000). Shoreline Mapping Techniques. *Journal of Coastal Research*, *16*(1), 111-124. http://www.jstor.org/stable/4300016

Moreno, M., Li, S., Melnick, D., Bedford, J. R., Baez, J. C., Motagh, M., Metzger, S., Vajedian, S., Sippl, C., Gutknecht, B. D., Contreras-Reyes, E., Deng, Z., Tassara, A., & Oncken, O. (2018). Chilean megathrust earthquake recurrence linked to frictional contrast at depth. *Nature Geoscience*, *11*(4), 285-290. https://doi.org/10.1038/s41561-018-0089-5

Moreno, M., Melnick, D., Rosenau, M., Baez, J., Klotz, J., Oncken, O., Tassara, A., Chen, J., Bataille, K., Bevis, M., Socquet, A., Bolte, J., Vigny, C., Brooks, B., Ryder, I., Grund, V., Smalley, B., Carrizo, D., Bartsch, M., & Hase, H. (2012). Toward understanding tectonic control on the Mw 8.8 2010 Maule Chile earthquake. *Earth and Planetary Science Letters*, *321-322*, 152-165. https://doi.org/https://doi.org/10.1016/j.epsl.2012.01.006

Moreno, M. S., Bolte, J., Klotz, J., & Melnick, D. (2009). Impact of megathrust geometry on inversion of coseismic slip from geodetic data: Application to the 1960 Chile earthquake. *Geophysical Research Letters*, *36*(16). https://doi.org/https://doi.org/10.1029/2009GL039276

Novack-Gottshall, P., & Wang, S. C. (2019). *KScorrect: Lilliefors-Corrected Kolmogorov-Smirnov Goodness-of-fit Tests. R package version 1.4.0*. https://CRAN.R-project.org/package=KScorrect

Ojeda, J., Ruiz, S., del Campo, F., & Carvajal, M. (2020). The 21 May 1960 Mw 8.1 Concepción Earthquake: A Deep Megathrust Foreshock That Started the 1960 Central-South Chilean Seismic Sequence. *Seismological Research Letters*, *91*(3), 1617-1627. https://doi.org/10.1785/0220190143

Olsen, K. M., Bangs, N. L., Tréhu, A. M., Han, S., Arnulf, A., & Contreras-Reyes, E. (2020). Thick, strong sediment subduction along south-central Chile and its role in great earthquakes. *Earth and Planetary Science Letters*, *538*, 116195. https://doi.org/https://doi.org/10.1016/j.epsl.2020.116195

Pajak, M. J., & Leatherman, S. (2002). The High Water Line as Shoreline Indicator. *Journal of Coastal Research*, *18*(2), 329-337. http://www.jstor.org/stable/4299078

Peltier, W. R., Argus, D. F., & Drummond, R. (2015). Space geodesy constrains ice age terminal deglaciation: The global ICE-6G_C (VM5a) model. *Journal of Geophysical Research: Solid Earth*, *120*(1), 450-487. https://doi.org/https://doi.org/10.1002/2014JB011176

Peterson, C. D., Doyle, D. L., & Barnett, E. T. (2000). Coastal flooding and beach retreat from coseismic subsidence in the central Cascadia margin, USA. *Environmental & Engineering Geoscience*, *6*(3), 255-269. https://doi.org/10.2113/gseegeosci.6.3.255

Peterson, C. D., Jol, H. M., Vanderburgh, S., Phipps, J. B., Percy, D., & Gelfenbaum, G. (2010). Dating of late Holocene beach shoreline positions by regional correlation of coseismic retreat events in the Columbia River littoral cell, USA. *Marine Geology*, *273*(1), 44-61. https://doi.org/https://doi.org/10.1016/j.margeo.2010.02.003

Philibosian, B., & Meltzner, A. J. (2020). Segmentation and supercycles: A catalog of earthquake rupture patterns from the Sumatran Sunda Megathrust and other well-studied faults worldwide. *Quaternary Science Reviews*, *241*, 106390. https://doi.org/https://doi.org/10.1016/j.quascirev.2020.106390

Philibosian, B., Sieh, K., Avouac, J.-P., Natawidjaja, D. H., Chiang, H.-W., Wu, C.-C., Shen, C.-C., Daryono, M. R., Perfettini, H., Suwargadi, B. W., Lu, Y., & Wang, X. (2017). Earthquake supercycles on the Mentawai segment of the Sunda megathrust in the seventeenth century and earlier. *Journal of Geophysical Research: Solid Earth*, *122*(1), 642-676. https://doi.org/https://doi.org/10.1002/2016JB013560

Pinegina, T. K., Bourgeois, J., Bazanova, L. I., Zelenin, E. A., Krasheninnikov, S. P., & Portnyagin, M. V. (2020). Coseismic coastal subsidence associated with unusually wide rupture of prehistoric earthquakes on the Kamchatka subduction zone: A record in buried erosional scarps and tsunami deposits. *Quaternary Science Reviews*, *233*, 106171. https://doi.org/https://doi.org/10.1016/j.quascirev.2020.106171

Pinegina, T. K., Bourgeois, J., Kravchunovskaya, E. A., Lander, A. V., Arcos, M. E. M., Pedoja, K., & MacInnes, B. T. (2013). A nexus of plate interaction: Vertical deformation of Holocene wave-built terraces on the Kamchatsky Peninsula (Kamchatka, Russia). *GSA Bulletin*, *125*(9-10), 1554-1568. https://doi.org/10.1130/B30793.1

Plafker, G. (1972). Alaskan earthquake of 1964 and Chilean earthquake of 1960: Implications for arc tectonics. *Journal of Geophysical Research (1896-1977)*, *77*(5), 901-925. https://doi.org/https://doi.org/10.1029/JB077i005p00901

Plafker, G., & Savage, J. C. (1970). Mechanism of the Chilean Earthquakes of May 21 and 22, 1960. *GSA Bulletin*, *81*(4), 1001-1030. https://doi.org/10.1130/0016-7606(1970)81[1001:MOTCEO]2.0.CO;2

Plafter, G. (1967). *Surface faults on Montague Island associated with the 1964 Alaska earthquake* [Report](543G). (Professional Paper, Issue. U. S. G. P. Office. https://pubs.usgs.gov/publication/pp543G

Prescott, J. R., & Hutton, J. T. (1994). Cosmic ray contributions to dose rates for luminescence and ESR dating: Large depths and long-term time variations. *Radiation Measurements*, *23*(2), 497-500. https://doi.org/https://doi.org/10.1016/1350-4487(94)90086-8

Pucino, N., Kennedy, D. M., Carvalho, R. C., Allan, B., & Ierodiaconou, D. (2021). Citizen science for monitoring seasonal-scale beach erosion and behaviour with aerial drones. *Scientific Reports*, *11*(1), 3935. https://doi.org/10.1038/s41598-021-83477-6

Rabassa, J., & Clapperton, C. M. (1990). Quaternary glaciations of the southern Andes. *Quaternary Science Reviews*, *9*(2), 153-174. https://doi.org/https://doi.org/10.1016/0277-3791(90)90016-4

Rajendran, C. P., Rajendran, K., Anu, R., Earnest, A., Machado, T., Mohan, P. M., & Freymueller, J. (2007). Crustal Deformation and Seismic History Associated with the 2004 Indian Ocean Earthquake: A Perspective from the Andaman–Nicobar Islands. *Bulletin of the Seismological Society of America*, *97*(1A), S174-S191. https://doi.org/10.1785/0120050630

Ranasinghe, R. (2016). Assessing climate change impacts on open sandy coasts: A review. *Earth-Science Reviews*, *160*, 320-332. https://doi.org/https://doi.org/10.1016/j.earscirev.2016.07.011

Rascle, N., & Ardhuin, F. (2013). A global wave parameter database for geophysical applications. Part 2: Model validation with improved source term parameterization.

Ocean Modelling, *70*, 174-188. https://doi.org/https://doi.org/10.1016/j.ocemod.2012.12.001

Rosenau, M., & Oncken, O. (2009). Fore-arc deformation controls frequency-size distribution of megathrust earthquakes in subduction zones. *Journal of Geophysical Research: Solid Earth*, *114*(B10). https://doi.org/https://doi.org/10.1029/2009JB006359

Rubin, C. M., Horton, B. P., Sieh, K., Pilarczyk, J. E., Daly, P., Ismail, N., & Parnell, A. C. (2017). Highly variable recurrence of tsunamis in the 7,400 years before the 2004 Indian Ocean tsunami. *Nature Communications*, *8*(1), 16019. https://doi.org/10.1038/ncomms16019

Saha, S., Moorthi, S., Pan, H.-L., Wu, X., Wang, J., Nadiga, S., Tripp, P., Kistler, R., Woollen, J., Behringer, D., Liu, H., Stokes, D., Grumbine, R., Gayno, G., Wang, J., Hou, Y.-T., Chuang, H.-y., Juang, H.-M. H., Sela, J., . . . Goldberg, M. (2010). The NCEP Climate Forecast System Reanalysis. *Bulletin of the American Meteorological Society*, *91*(8), 1015-1058. https://doi.org/10.1175/2010BAMS3001.1

Salditch, L., Stein, S., Neely, J., Spencer, B. D., Brooks, E. M., Agnon, A., & Liu, M. (2020). Earthquake supercycles and Long-Term Fault Memory. *Tectonophysics*, *774*, 228289. https://doi.org/https://doi.org/10.1016/j.tecto.2019.228289

Sallarès, V., & Ranero, C. R. (2019). Upper-plate rigidity determines depth-varying rupture behaviour of megathrust earthquakes. *Nature*, *576*(7785), 96-101. https://doi.org/10.1038/s41586-019-1784-0

Sallenger, A. H. J. (2000). Storm Impact Scale for Barrier Islands. *Journal of Coastal Research*, *16*(3), 890-895. http://www.jstor.org/stable/4300099

Satake, K. (2015). Geological and historical evidence of irregular recurrent earthquakes in Japan. *Philosophical Transactions of the Royal Society A: Mathematical, Physical and Engineering Sciences*, *373*(2053), 20140375. https://doi.org/doi:10.1098/rsta.2014.0375

Satake, K., & Atwater, B. F. (2007). Long-Term Perspectives on Giant Earthquakes and Tsunamis at Subduction Zones. *Annual Review of Earth and Planetary Sciences*, *35*(1), 349-374. https://doi.org/10.1146/annurev.earth.35.031306.140302

Schmidt, J., Evans, I. S., & Brinkmann, J. (2003). Comparison of polynomial models for land surface curvature calculation. *International Journal of Geographical Information Science*, *17*(8), 797-814. https://doi.org/10.1080/13658810310001596058

Schwanghart, W., & Scherler, D. (2014). Short Communication: TopoToolbox 2 – MATLAB-based software for topographic analysis and modeling in Earth surface sciences. *Earth Surface Dynamics*, *2*, 1-7. https://doi.org/10.5194/esurf-2-1-2014

Shennan, I. (2015). Handbook of sea-level research. In *Handbook of Sea-Level Research* (pp. 3-25). https://doi.org/https://doi.org/10.1002/9781118452547.ch2

SHOA. (2020). *Catálogo de Cartas Y Publicaciones Náuticas. Pub. 3000*

Shyu, J. B. H., Wang, C.-C., Wang, Y., Shen, C.-C., Chiang, H.-W., Liu, S.-C., Min, S., Aung, L. T., Than, O., & Tun, S. T. (2018). Upper-plate splay fault earthquakes along the Arakan subduction belt recorded by uplifted coral microatolls on northern Ramree Island, western Myanmar (Burma). *Earth and Planetary Science Letters*, *484*, 241-252. https://doi.org/https://doi.org/10.1016/j.epsl.2017.12.033

Sieh, K., Natawidjaja, D. H., Meltzner, A. J., Shen, C.-C., Cheng, H., Li, K.-S., Suwargadi, B. W., Galetzka, J., Philibosian, B., & Edwards, R. L. (2008). Earthquake Supercycles Inferred from Sea-Level Changes Recorded in the Corals of West Sumatra. *Science*, *322*(5908), 1674-1678. https://doi.org/doi:10.1126/science.1163589

Smith, J. M. (2001). Modeling Nearshore Wave Transformation With STWAVE.

Stein, S., Geller, R. J., & Liu, M. (2012). Why earthquake hazard maps often fail and what to do about it. *Tectonophysics*, *562-563*, 1-25. https://doi.org/https://doi.org/10.1016/j.tecto.2012.06.047

Stockdon, H. F., Holman, R. A., Howd, P. A., & Sallenger, A. H. (2006). Empirical parameterization of setup, swash, and runup. *Coastal Engineering*, *53*(7), 573-588. https://doi.org/https://doi.org/10.1016/j.coastaleng.2005.12.005

Tappin, D. R., Evans, H. M., Jordan, C. J., Richmond, B., Sugawara, D., & Goto, K. (2012). Coastal changes in the Sendai area from the impact of the 2011 Tōhoku-oki tsunami: Interpretations of time series satellite images, helicopter-borne video footage and field

observations. *Sedimentary Geology*, *282*, 151-174. https://doi.org/https://doi.org/10.1016/j.sedgeo.2012.09.011

Thieler, E. R., Himmelstoss, E. A., Zichichi, J. L., & Ergul, A. (2009). *The Digital Shoreline Analysis System (DSAS) Version 4.0 - An ArcGIS extension for calculating shoreline change* [Report](2008-1278). (Open-File Report, Issue. U. S. G. Survey. http://pubs.er.usgs.gov/publication/ofr20081278

Tolman, H., Accensi, M., Alves, J.-H., Ardhuin, F., Bidlot, J., Booij, N., Bennis, A.-C., Campbell, T., Chalikov, D., Filipot, J.-F., Foreman, M., Janssen, P., Leckler, F., Li, J.-G., Chawla, A., Lind, K., Orzech, M., Padilla-Hernandez, R., Rogers, E., & Zieger, S. (2014). *User manual and system documentation of WAVEWATCH III version 4.18*.

Tzanis, A. (2010a). MATGPR Release 2 : A freeware MATLAB ® package for the analysis & interpretation of common & single offset GPR data.

Tzanis, A. (2010b). matGPR Release 2: A freeware MATLAB® package for the analysis & interpretation of common and single offset GPR data. *FastTimes*, *15*, 17-43.

Vargas, G., Farias, M., Carretier, S., Tassara, A., Baize, S., & Melnick, D. (2011). Coastal uplift and tsunami effects associated to the 2010 M(w)8.8 Maule earthquake in Central Chile. *Andean geology*, *38*(1), 219-238. https://publishup.uni-potsdam.de/frontdoor/index/index/docId/37132

Vos, K., Harley, M. D., Splinter, K. D., Simmons, J. A., & Turner, I. L. (2019a). Sub-annual to multi-decadal shoreline variability from publicly available satellite imagery. *Coastal Engineering*, *150*, 160-174. https://doi.org/https://doi.org/10.1016/j.coastaleng.2019.04.004

Vos, K., Splinter, K. D., Harley, M. D., Simmons, J. A., & Turner, I. L. (2019b). CoastSat: A Google Earth Engine-enabled Python toolkit to extract shorelines from publicly available satellite imagery. *Environmental Modelling & Software*, *122*, 104528. https://doi.org/https://doi.org/10.1016/j.envsoft.2019.104528

Wang, B., Shi, W., & Liu, E. (2015). Robust methods for assessing the accuracy of linear interpolated DEM. *International Journal of Applied Earth Observation and Geoinformation*, *34*, 198-206. https://doi.org/https://doi.org/10.1016/j.jag.2014.08.012

Wang, Q. (2023). *Dynamic Time Warping (DTW)*. https://github.com/wq2012/dynamic_time_warping/releases/tag/v2.2

Wessel, P., & Smith, W. (1996). A global, self-consistent, hierarchical, high-resolution shoreline database. *Journal of Geophysical Research*, *101*, 8741-8743. https://doi.org/10.1029/96JB00104

Wesson, R. (2017). *Darwin's First Theory: Exploring Darwin's Quest for a Theory of Earth*. Pegasus Books.

Wesson, R. L., Melnick, D., Cisternas, M., Moreno, M., & Ely, L. L. (2015). Vertical deformation through a complete seismic cycle at Isla Santa María, Chile. *Nature Geoscience*, *8*(7), 547-551. https://doi.org/10.1038/ngeo2468

Williams, R. T., Goodwin, L. B., Sharp, W. D., & Mozley, P. S. (2017). Reading a 400,000-year record of earthquake frequency for an intraplate fault. *Proceedings of the National Academy of Sciences*, *114*(19), 4893-4898. https://doi.org/doi:10.1073/pnas.1617945114

Winckler, P., Contreras-López, M., Campos-Caba, R., Beyá, J. F., & Molina, M. (2017). El temporal del 8 de agosto de 2015 en las regiones de Valparaíso y Coquimbo, Chile Central. *Latin american journal of aquatic research*, *45*, 622-648. http://www.scielo.cl/scielo.php?script=sci_arttext&pid=S0718-560X2017000400622&nrm=iso

ANEXO 1. Material suplementario para el capítulo II

Supplemental methods for Wave modelling

Wave climate in TCUE was characterized using a combination of a Pacific-wide model implemented in WAVEWATCH III and a nearshore transformation model at STWAVE. The Pacific-wide model was forced by 3-hour surface wind data and daily ice coverage from CFSR dataset. WAVEWATCH III was implemented in a numerical grid between 135°E-65°W and 75°S-60°N, with a spatial resolution of 1°. Bathymetry was extracted from ETOPO2v2′s (NGDC 2020) 2 × 2-minute grid, and the coastline was built from the GHHSGVIII database (Wessel & Smith, 1996). Wave spectra were resolved with 32 frequencies (0.0373–0.78 Hz) and a directional resolution of 15°. Growth and dissipation terms were set with the ST4 parametrization (Ardhuin *et al.*, 2010; Rascle & Ardhuin, 2013), while nonlinear energy transfer was resolved using the Discrete Interaction* Approximation (Hasselmann & Hasselmann, 1985). These parametrizations adequately characterize the multimodal wave spectra offshore Chile (Beya *et al.*, 2017). Time series of 20 years were computed for offshore wave spectra and derived statistical parameters, namely significant wave height; mean period, and mean wave direction. Two-dimensional spectra were extracted at a distance such that waves are affected by the bathymetry. Given the coarse resolution of the global model, such extraction was at approximately 130 km offshore.

The offshore wave climate was downscaled by using the numerical model STWAVE (STeady-state spectral WAVE; Smith, 2001) Transformation of wave spectra from deep water to

numerical nodes at the study sector was conducted using an extended version of Massel's superposition method of elementary spectral components (Massel, 1996; equation 6.16), as we added diffraction to the original expression for refraction and shoaling. Nearshore bathymetry was obtained from navigation charts (SHOA, 2020). A total of 750 unitary wave spectra were used to compute transfer functions from deep waters to local virtual buoys (for this study we used the node at 37.00ºS, 73.50ºW; Figure 2.1d) using STWAVE. Each unitary wave spectrum was built with a resolution of 25 directions and 30 frequencies, covering periods from 2.04 s to 29.07 s and directions between 7.5° and 352.5°. Nearshore wave models were configured using three rectangular nested grids with resolutions of 200 × 200 m in deep waters, 50 × 50 m to cover each bay, and 10 × 10 m at the vicinity of each site, the local bathymetry 20 m resolution was taken from Jara-Muñoz *et al.*, 2017) and from (SHOA, 2020). Sea level was defined as constant (i.e., sea level rise and a coseismic uplift of 2m were used to evaluate changes in wave patterns). Finally, wave spectra obtained in deep waters with WAVEWATCH III were transformed into digital wave gauges using these transfer functions, where time series of statistical parameters were computed (Figure S2).

Supplementary Figures

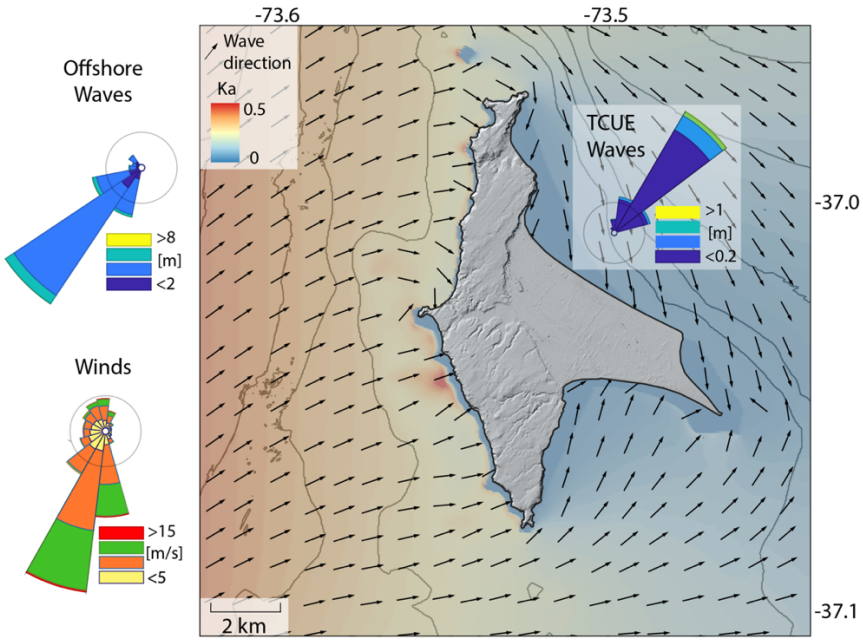

Figure S1. Wind and wave roses estimated using CFSR data (See methods section for details). Offshore waves calculated 150 km west of ISM, TCUE beach wave rose is centered on the node.

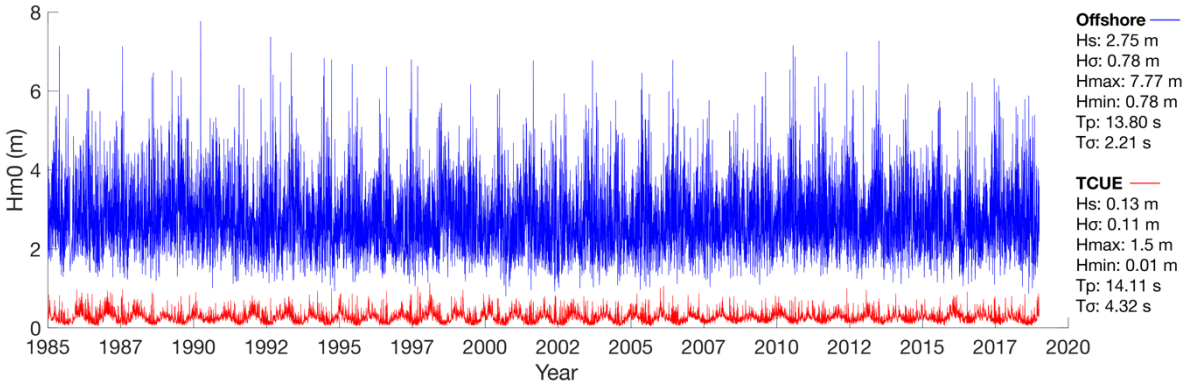

Figure S2. Offshore (150 km W) and TCUE (node in 37.00ºS, 73.50ºW) modeled significant wave height time series with main statistical parameters. Hs: Mean significant wave height, Hσ: Wave height standard deviation, Hmax: Wave height maximum, Hmin: Wave height minimum, Tp: Mean wave period, Tσ: Wave period standard deviation.

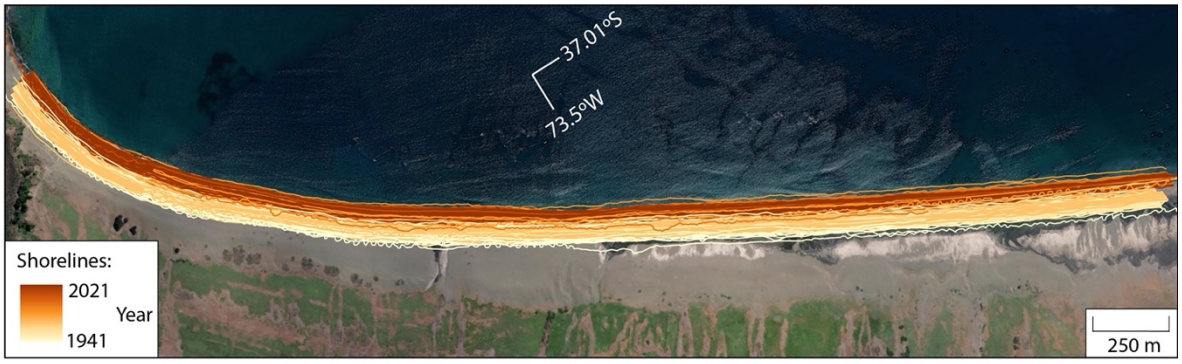

Figure S3. Shorelines position (See methods section for details).

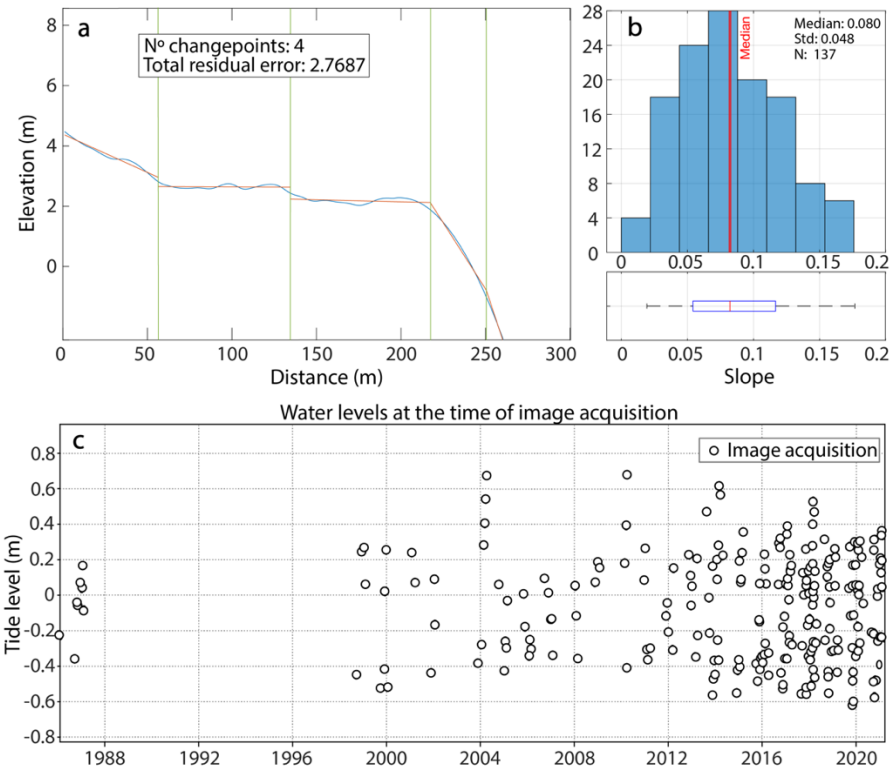

Figure S4. a) Example of beach slope calculation from DEMs using abrupt changes search algorithm ('findchangepts' in Matlab). Inset shows the number of slope changes identified and the horizontal error estimate in meters. b) Histogram of total calculated slopes. c) Calculation of the tide level for each aerial image used.

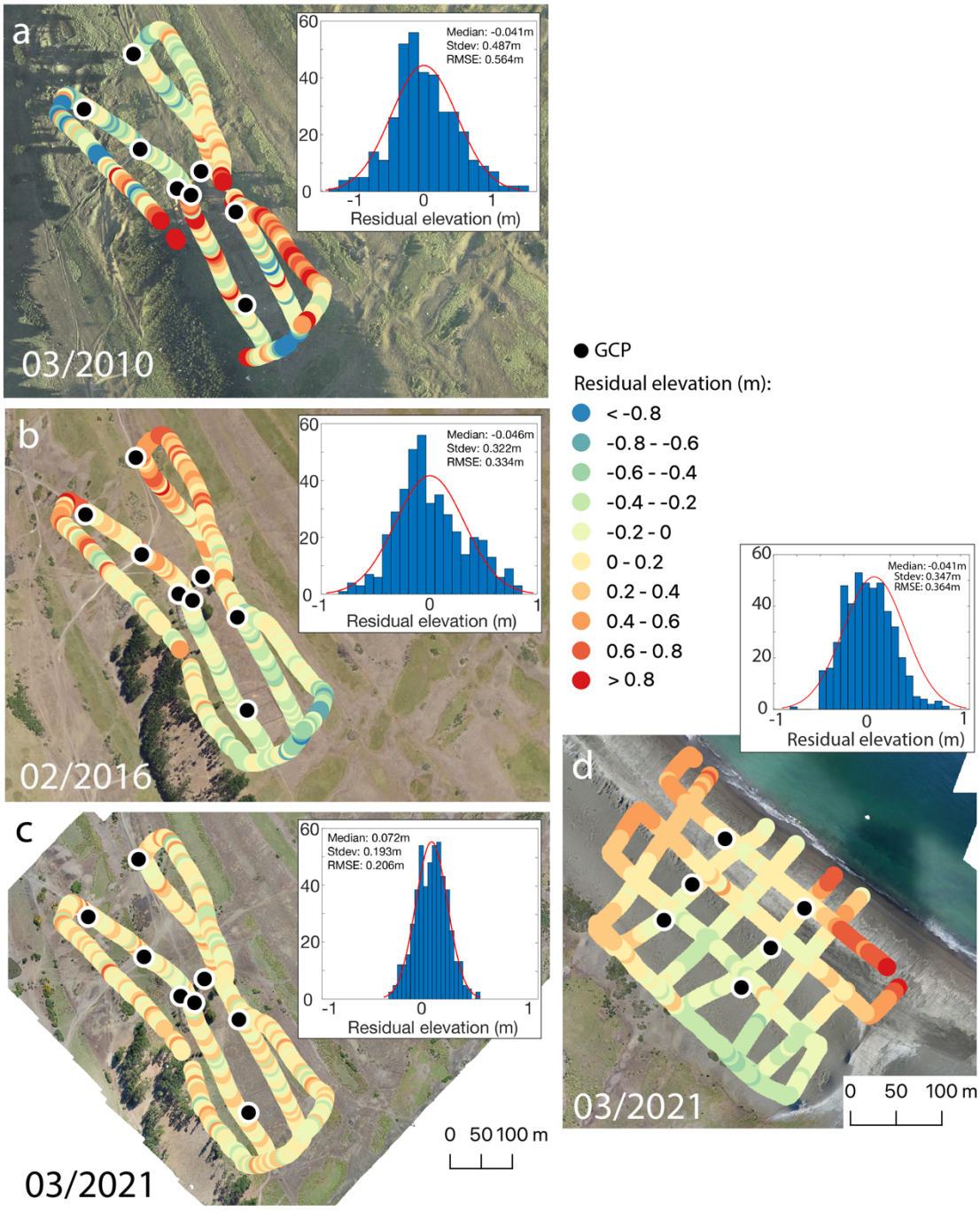
a
03/2010
Median: -0.041m
Stdev: 0.487m
RMSE: 0.564m
Residual elevation (m)
b
02/2016
Median: -0.046m
Stdev: 0.322m
RMSE: 0.334m
Residual elevation (m)
c
03/2021
Median: 0.072m
Stdev: 0.193m
RMSE: 0.206m
Residual elevation (m)
0 50 100 m
GCP
Residual elevation (m):
< -0.8
-0.8 - -0.6
-0.6 - -0.4
-0.4 - -0.2
-0.2 - 0
0 - 0.2
0.2 - 0.4
0.4 - 0.6
0.6 - 0.8
> 0.8
d
03/2021
Median: -0.041m
Stdev: 0.347m
RMSE: 0.364m
Residual elevation (m)
0 50 100 m

Figure S5. Location of ground control points (GCPs) and independent control points (ICPs). The color of the ICPs corresponds to the difference between the elevation of the DEM and the elevation of the ICP. Inset in each figure shows the histogram of the residual elevation.

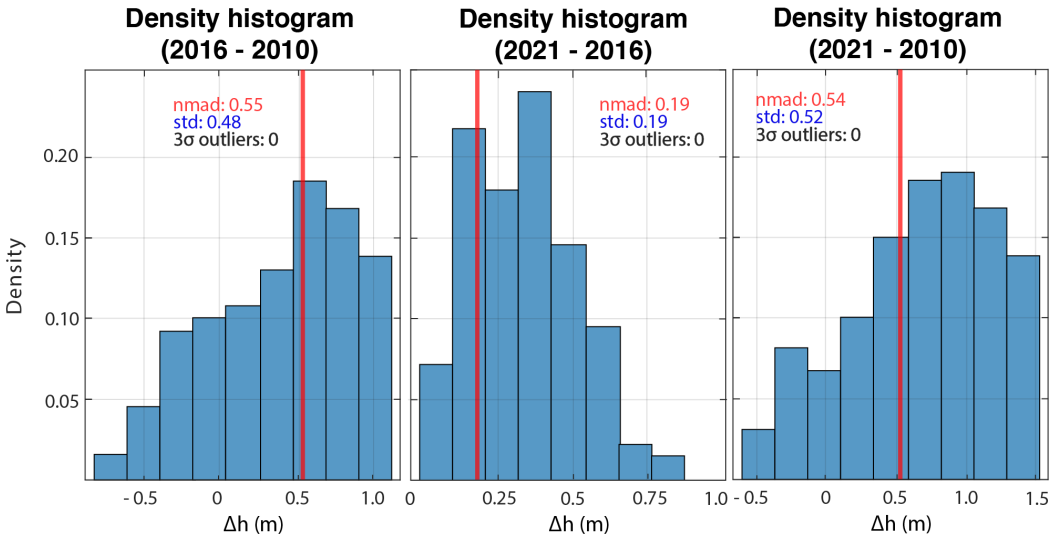

Figure S6. Statistical distribution of errors used to determine LoD (Limit of Detection) for the calculation of each DoD.

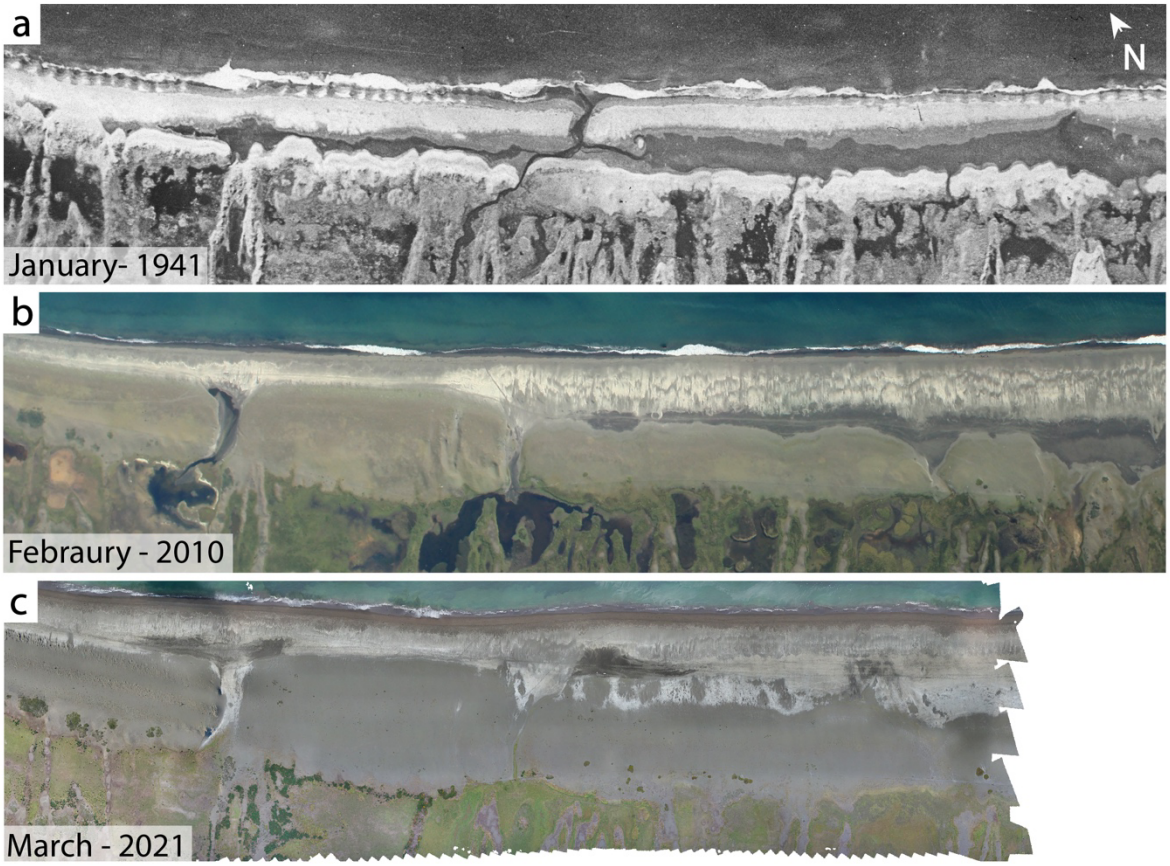

Figure S7. Vertical air photos from 1941, 2010, and 2021 used in Figure 4.

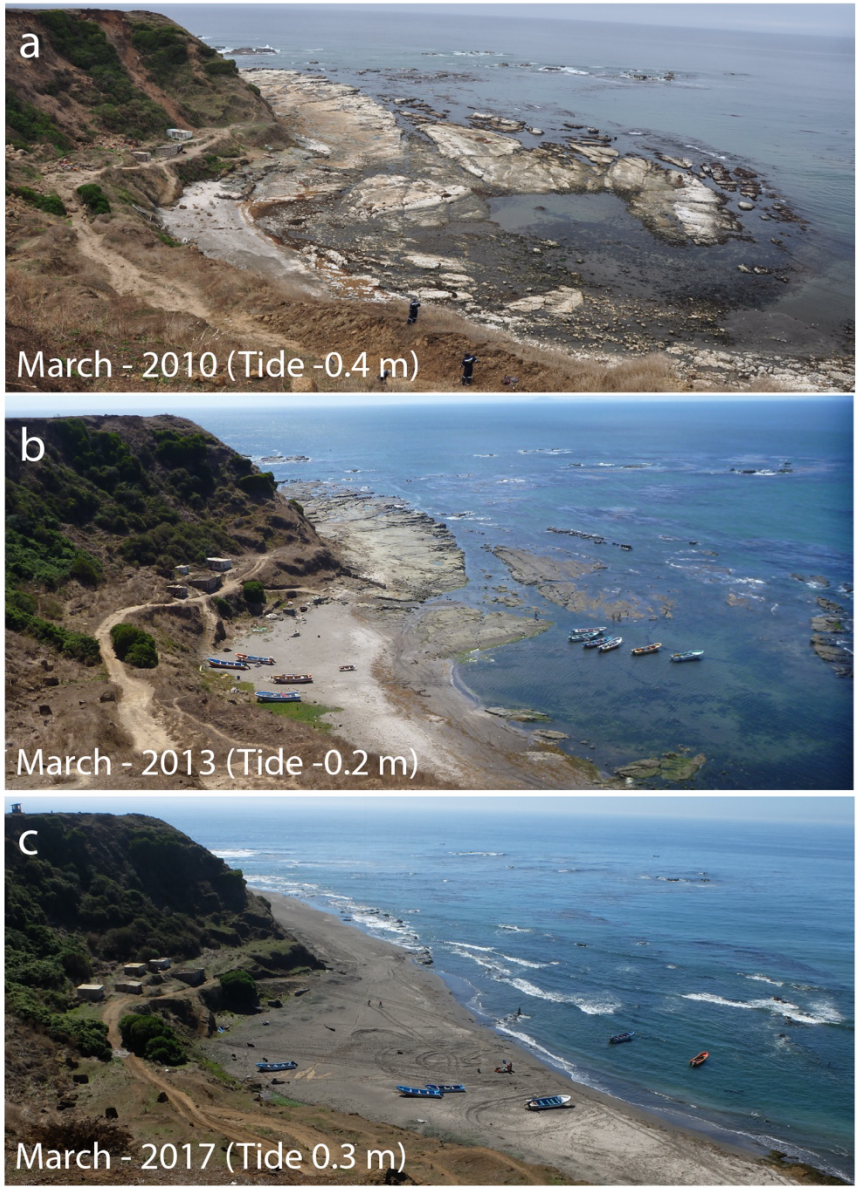

Figure S8. Temporal evolution at Puerto Norte. Note that sand quickly covered the rocky platform that emerged in 2010 forming a sandy beach. See Fig. 1b for location.

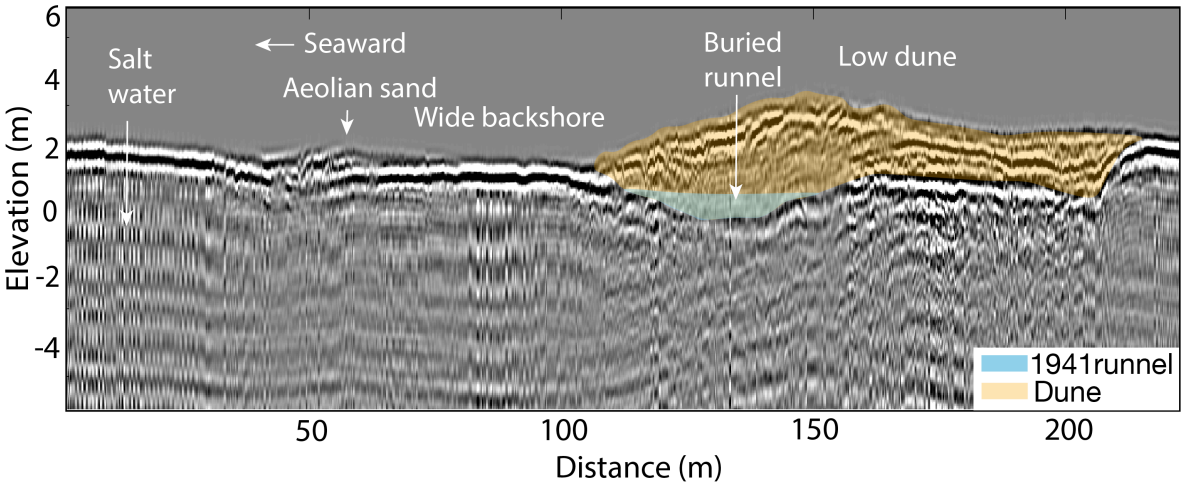

Figure S9. GPR beach profile indicated in Figure 3 and Figure S10. Note the backshore width, low dune elevation, and buried sediments.

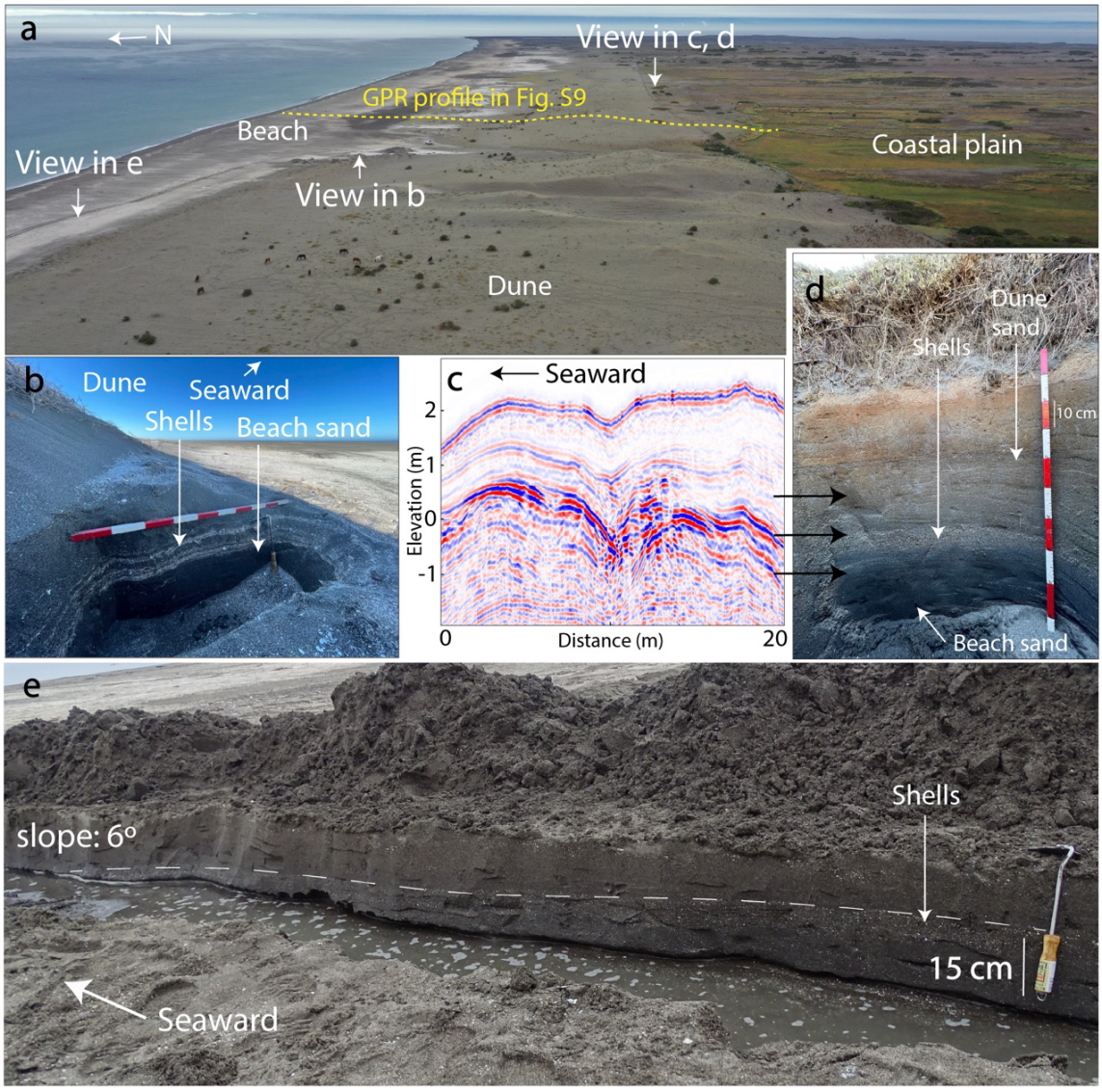

Figure S10. a) Aerial view of the Tres Cuevas beach. b) Sedimentary sequence in the active dune toe. c) GPR profile in the Dune back. d) Stratigraphy of Figure S10c. Note the correlation between the GPR signals and each sediment level. e) Excavation in modern beach. Note the seaward inclined shells layer (progradation signal).

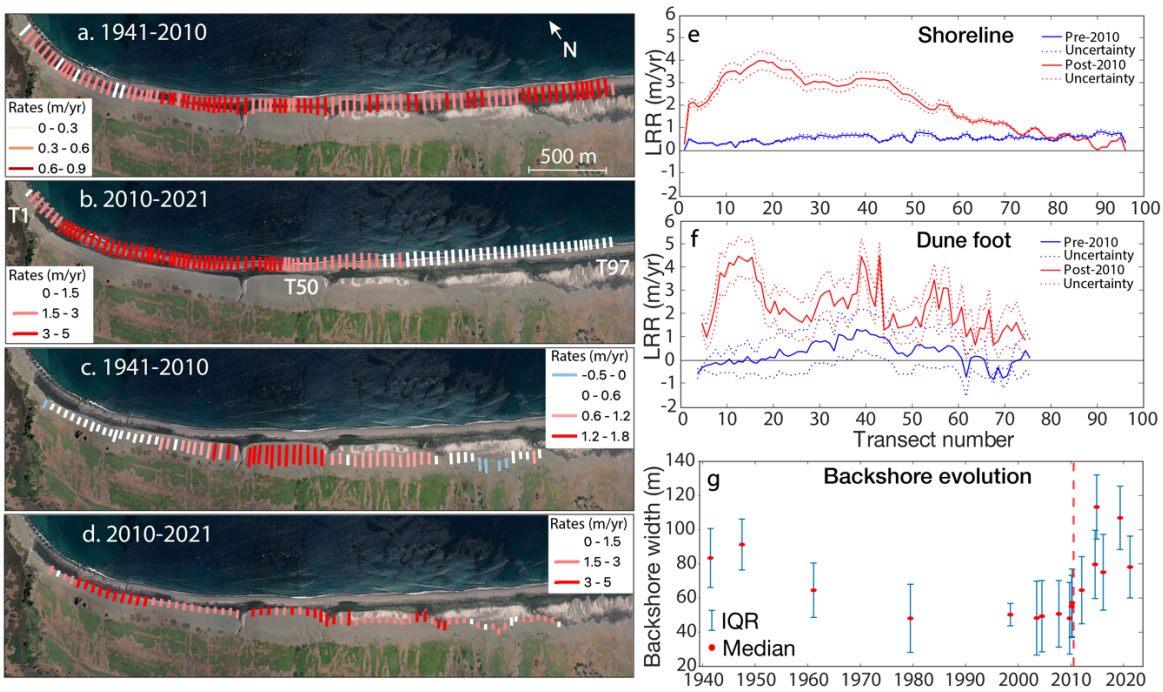

Figure S11. a,b) Shoreline progradation rate measured in each transect pre and post-2010 earthquake. T1, T50, and T97 are the transect number. c,d) Dune toe movement rate measured in each transect pre and post-2010 earthquake. e,f) Measurement of the shoreline and dune movement rate along the beach pre and post-2010 earthquake. g) Backshore width measurement Since 1941. Note the shortening before 2010 and the change in this trend after the earthquake.

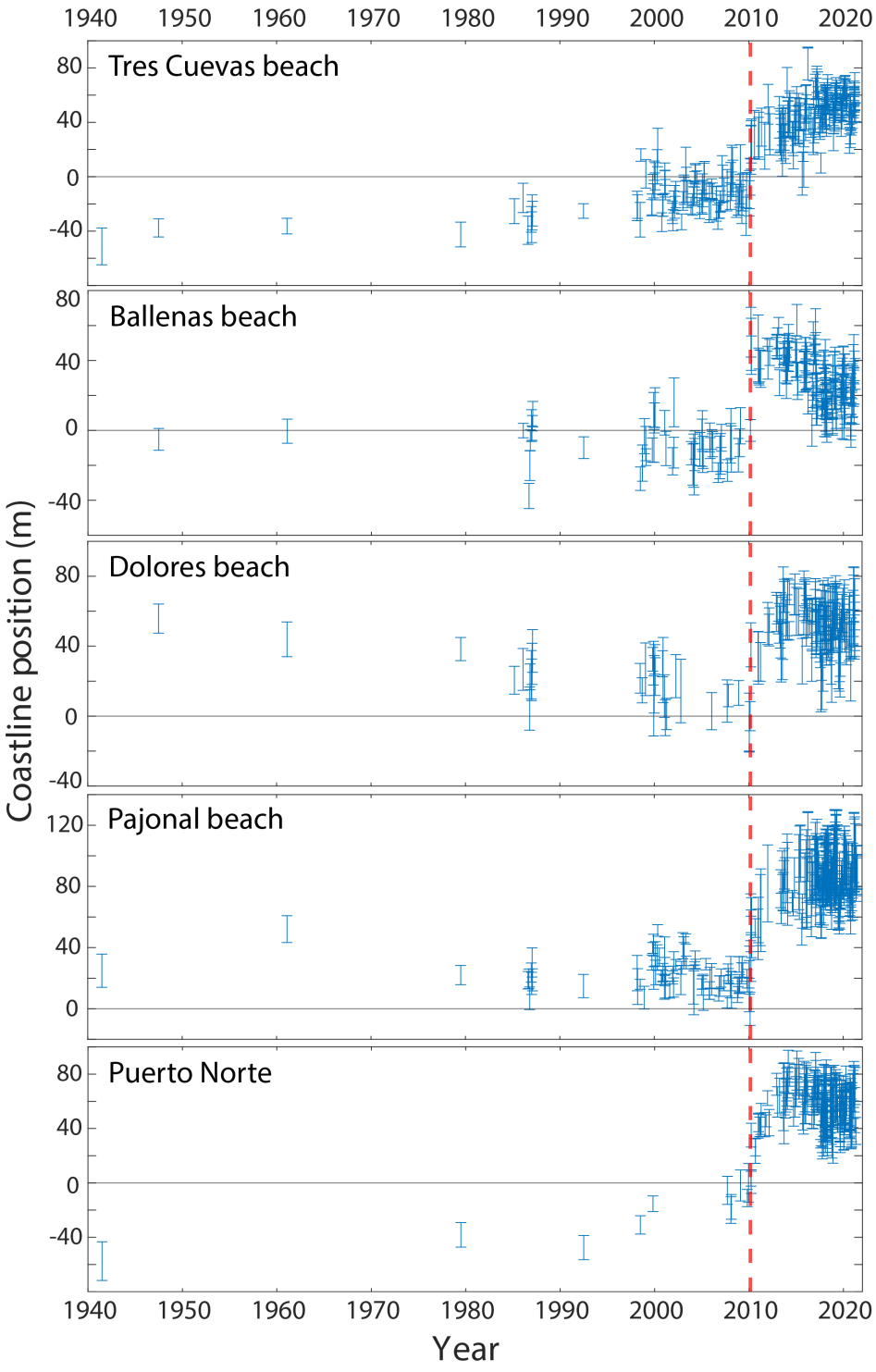
Tres Cuevas beach
Ballenas beach
Dolores beach
Pajonal beach
Puerto Norte
Coastline position (m)
Year
1940
1950
1960
1970
1980
1990
2000
2010
2020

Figure S12. Complete time series for the shoreline position of each beach surveyed on the island.

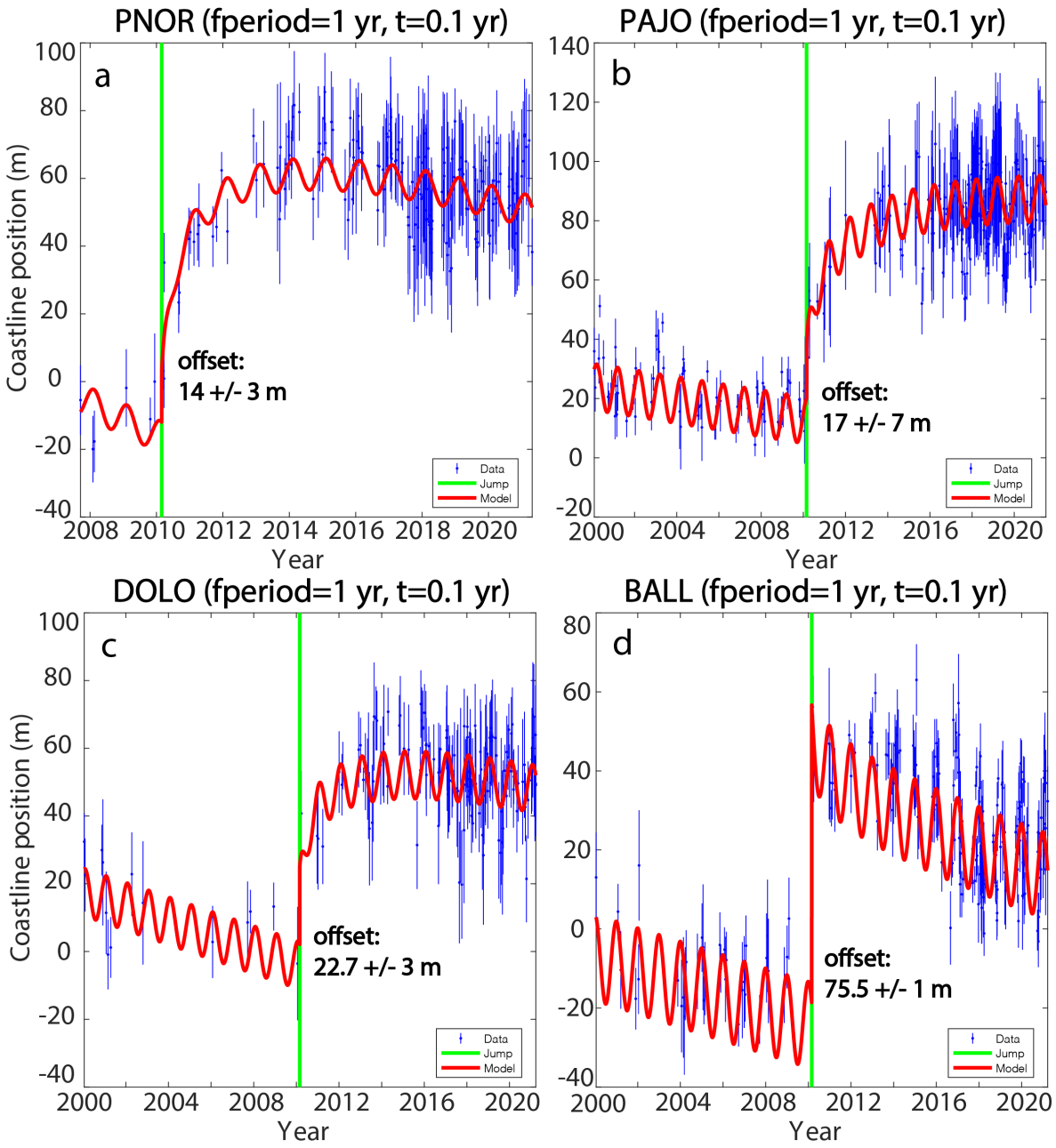

Figure S13. Trajectory model of Puerto Norte, Pajonal, Dolores, and Ballenas shoreline position change showing the 2010 earthquake abrupt offset, the progradation rate change, and the

stational variation. The shoreline position is referenced to 2010 pre-earthquake. NOR: Puerto Norte, DOLO: Dolores, BALL: Ballenas, PAJO: Pajonal.

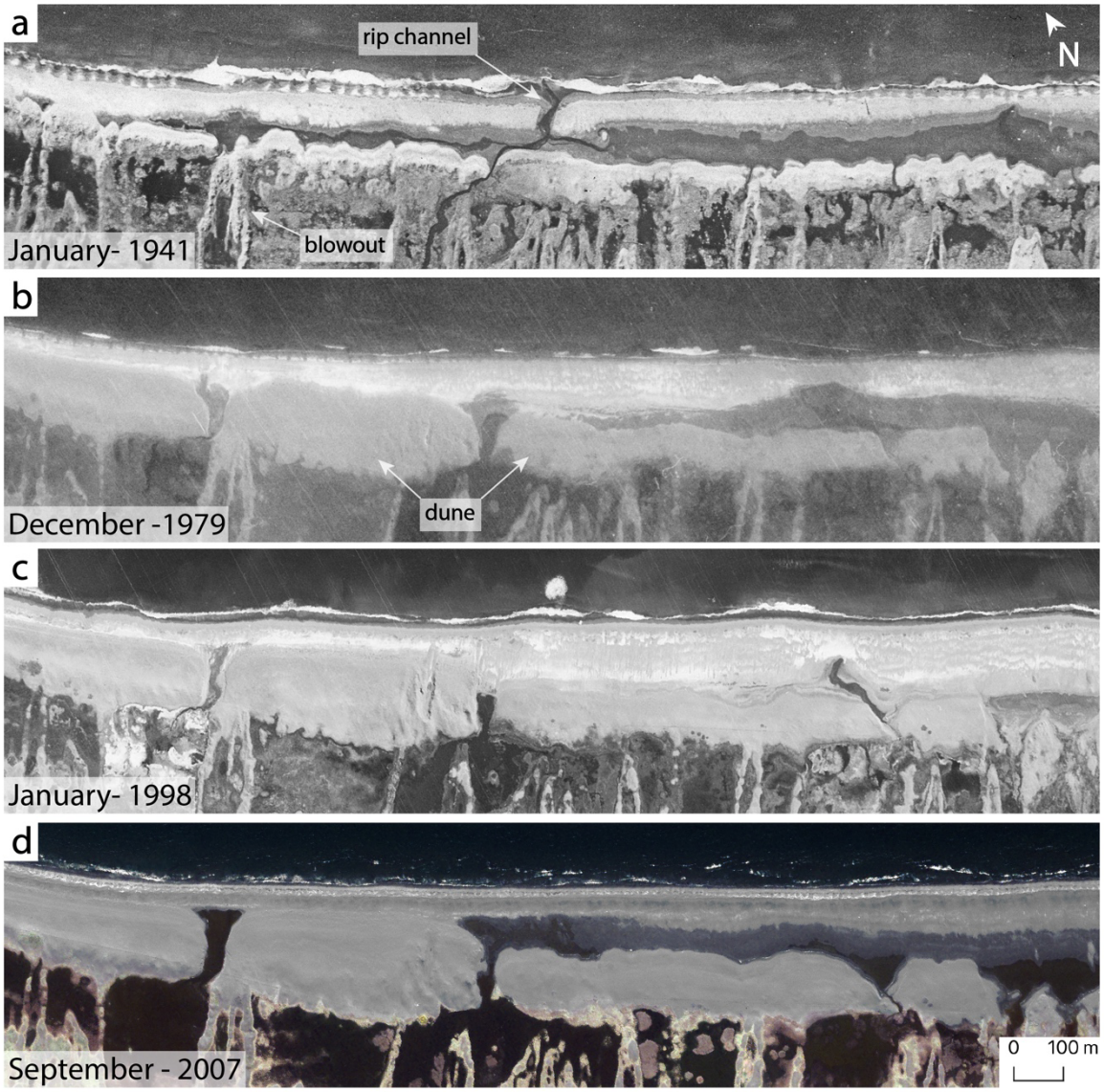

Figure S14. Vertical air photos from 1941 (Tide: -0.4m), 1979 (Tide: 0.2 m), 1998 (IGM; Tide: -0.4m), and 2007 (IKONOS; Tide: -0.1m) showing geomorphic changes during interseismic

time at Tres Cuevas beach. Note the dune construction between 1941 and 1979 and the very narrow backshore in 2007.

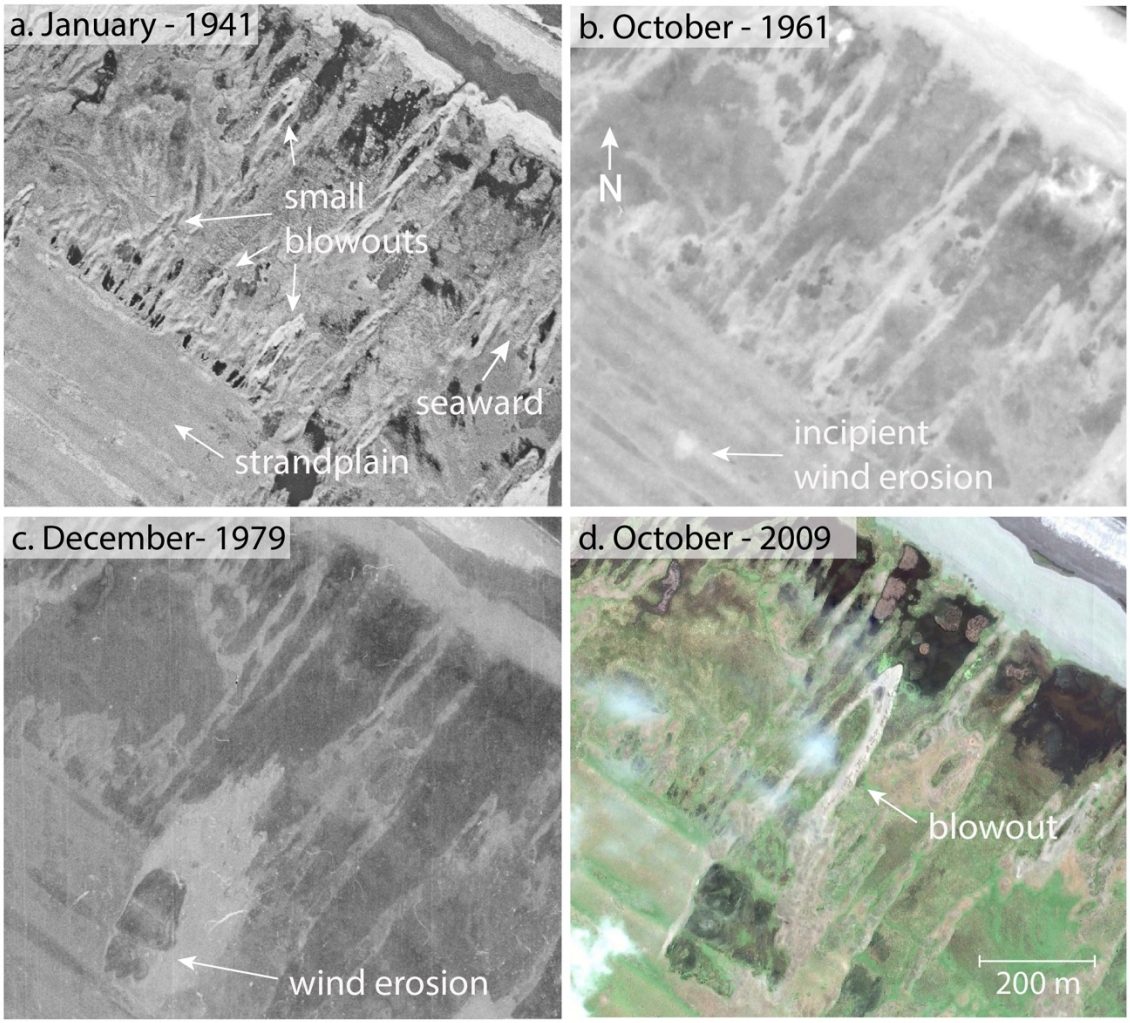

Figure S15. Vertical air photos from 1941, 1961, 1979 (IGM), and 2009 (Google) showing the effects of SW wind erosion on the coastal plain and the development of a large blowout. Note the advance of the sand in the blowouts.

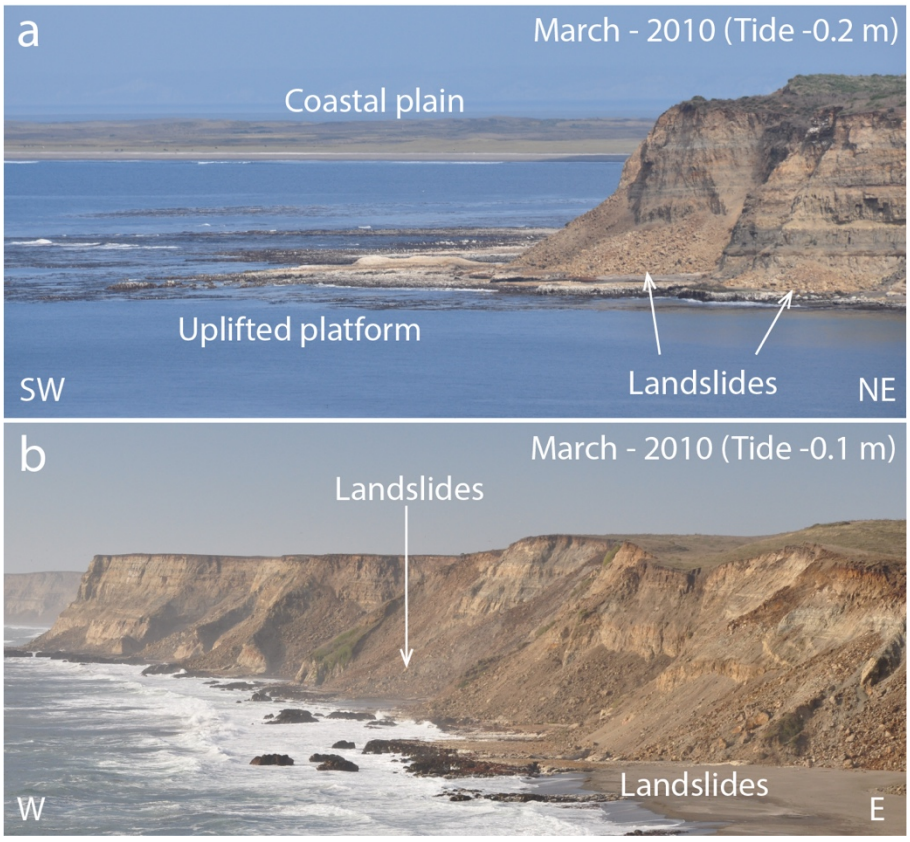

Figure S16. Views of the fresh landslides triggered during the 2010 earthquake. a) Tres Cuevas beach, b) Dolores beach. See Figure 1b for location.

Supplementary Tables

Table S1. Set of error (i.e, elevation change in calibration areas where a theoretical zero change should occur) statistics used to determine LoD (Limit of Detection) for the calculation of each DoD. 'Std': Standard deviation; 'NMAD': Normalised Median Absolute Deviation; 'a_q683': 68.3th quantile of absolute error; 'a_q95': 95th quantile of absolute error; 'RRMSE': Robust Root Mean Squared Error; 'n': Number of total observations; 'n_outliers': n outliers using the 3-sigma method; 'saphiro_stat', 'saphiro_p', 'saphiro_normality': Shapiro–Wilk statistics, p-values, and normality evaluation; 'ago_stat', 'ago_p', 'agoo_normality': D'Agostino–Pearson statistics, p-values, and normality evaluation; 'LoD': Limit of Detection based on normality check.

DEM of Difference	*Mean*	*Median*	*Std*	*NMAD*	*a_q683*	*a_q95*	*RRMSE*	*n*	*n_outliers*	*saphiro_stat*	*saphiro_p*	*ago_stat*	*ago_p*	*saphiro_normality*	*ago_normality*	*LoD*
2016 - 2010	0.3767	0.4617	0.4756	0.5463	0.7007	1.0010	0.7153	130	0	0.9550	0.000282381	13.6976	0.00107	not normal	not normal	0.5463
2021 - 2016	0.3360	0.3217	0.1885	0.1854	0.4072	0.5879	0.3713	130	0	0.8722	3.37E-09	77.9121	1.21E-17	not normal	not normal	0.1854
2021 - 2010	0.7127	0.8241	0.5212	0.5435	1.0347	1.3641	0.9872	130	0	0.9300	4.45E-06	12.7241	0.00172	not normal	not normal	0.5435

ANEXO 2. Material suplementario para el capítulo III

Supporting Information Text

Luminescence and radiocarbon dating of beach ridges

We collected a total of 16 samples for luminescence: 10 from different ridges at depths between 0.4 to 2.1 m; 4 samples from ridge 11 (2 at each flank) to observe the variation according to the dated zone; and 2 samples for luminescence from the modern dune at a depth of 0.1 and 0.4 m (fig. S23 and Table S1). We collected these samples from the clean, straight walls of the pits by pushing plastic (PVC) tubes horizontally into the sand and capping them appropriately before extraction. We collected additional sand samples from each pit in plastic bags to determine dose rates.

We analyzed the beach ridge samples at the Cologne Luminescence Laboratory. Luminescence dating relies on the time-dependent accumulation of latent energy in quartz and feldspar minerals due to ionizing radiation, and the resetting of this energy during sunlight exposure. Sediment ages are inferred by measuring the energy dose accumulated since the last sunlight exposure (burial dose) and the ionizing radiation received by the sediment per unit of time (dose rate). Since quartz, usually, the preferred mineral for dating Holocene sediments, turned out to have thermally unstable luminescence signals (fig S24 and S25) and thus underestimates contextual radiocarbon ages (Table S2) we used potassium feldspar for the chronologies presented in this study.

Minerals for burial dose determination were extracted by sieving to grain sizes of 100–150 μm, and treatment with HCl (10%), H_2O_2 (10%), and sodium oxalate to remove carbonates, organic matter, and clay. Density liquid was used to separate potassium-rich feldspar grains (<2.58 g/cm^3). For luminescence measurements, feldspar grains were fixed on steel discs using 2-mm patches of silicon spray. All samples were measured on an automated Risø TL/OSL reader with $^{90}Sr/^{90}Y$ beta source delivering ~0.075 Gy/s at the sample position. Luminescence signals were stimulated with infrared LEDs centered at 870±40 nm and detected through an interference filter with peak transmission at 410 nm.

Equivalent dose (De) measurements followed a low-temperature post-infrared-infrared protocol with an IR signal measured at 50°C (IR_{50}) followed by an IR signal at 150 °C (pIR_{150}); $pIRIR_{150}$ protocol (Madsen *et al.*, 2011) (Table S3). For the samples investigated in this study, the selected protocol presents the best compromise between low laboratory residual doses and low fading rates for both signals (fig. S26). While generally both signals measured within the $pIRIR_{150}$ protocol may be used for dating (Brill & Cisternas, 2020), ages based on the pIR_{150} signal tend to overestimate associated radiocarbon ages for samples from Isla Santa Maria (Table S2). The chronology used for all further discussion in this paper is therefore solely based on ages derived from the IR_{50} signal. For each sample, between 17 and 27 aliquots were accepted for burial dose calculation. Due to the ~gaussian shape (fig. S27) and the low scatter of equivalent dose distributions (<20% over-dispersion for all samples older ~200 yrs) the IR_{50} signals of all samples were assumed to be completely rest prior to burial and the central age model (Galbraith *et al.*, 1999) was applied to calculate burial doses.

Dose rates (see Table S4 for a summary) were obtained from radionuclide concentrations of uranium (^{238}U), thorium (^{232}Th), and potassium (K) determined with high-resolution gamma spectrometry (Ortec HPGe gamma-ray detector). Based on radionuclide concentrations and in-situ water contents, dose rates were derived using the DRAC software (Durcan *et al.*, 2015). The reduced efficiency of alpha particles in generating feldspar luminescence signals was corrected using a-values of 0.07 ± 0.02 (Kreutzer *et al.*, 2014). The internal potassium content of feldspar grains was assumed as 12.5 ± 0.5% (Huntley & Baril, 1997). Cosmic dose rates were calculated according to Prescott and Hutton (Prescott & Hutton, 1994) by accounting for geographical position, altitude, and sediment cover. Finally, all ages were corrected for signal loss due to anomalous fading using a mean g-value of 4.2 ± 0.1 %/decade and the approach of Huntely and Lamothe (Huntley & Lamothe, 2001).

Finally, to test luminescence dating, we dated ridges 11, 17 and 24 using radiocarbon from remains of calcareous tubes from *polychaete* worms, left as drift debris on the ancient beaches.

These samples were collected from pits in each of these ridges (fig. S15). Because the tubes are only ~ 0.2 mm thick and very delicate, we assumed very little transport, and that their age should be close than the deposition time, i.e. close to beach abandonment and ridge formation. The tubes contain enough organic carbon (chitin) for radiocarbon dation (fig. S10 and Table S5). Radiocarbon measurements were performed at the DirectAMS laboratory, USA, and calibrated to years BP using Oxcal v.4.4 (Bronk Ramsey, 2021) with the Marine 20 calibration curve (Heaton *et al.*, 2020). We used the marine reservoir age offset of 43 ± 52 yr (Ingram & Southon, 1996) included in the Global marine reservoir database (http://calib.org/marine).

Supporting Figures

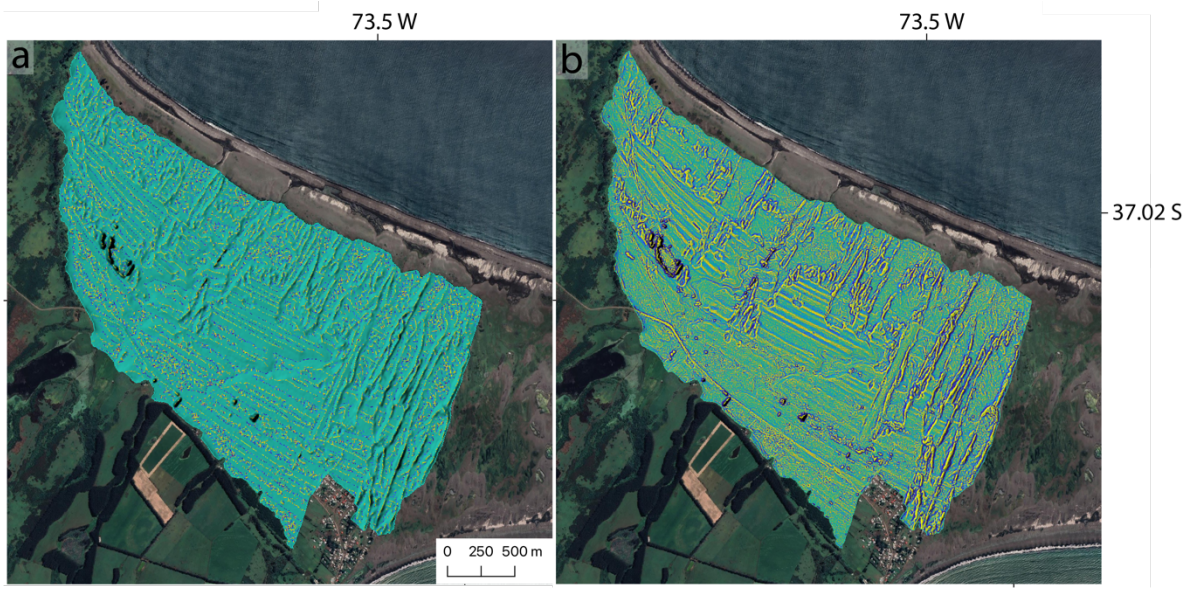

Figure S1. a) Contour curvature of the coastal plain digital elevation model. Note ridge crest in yellow and swales in blue. b) Profile curvature of the coastal plain digital elevation model. Note clear surface geomorphic expression of ridge crests. NNE-SSW oriented crests correspond to elongated dunes.

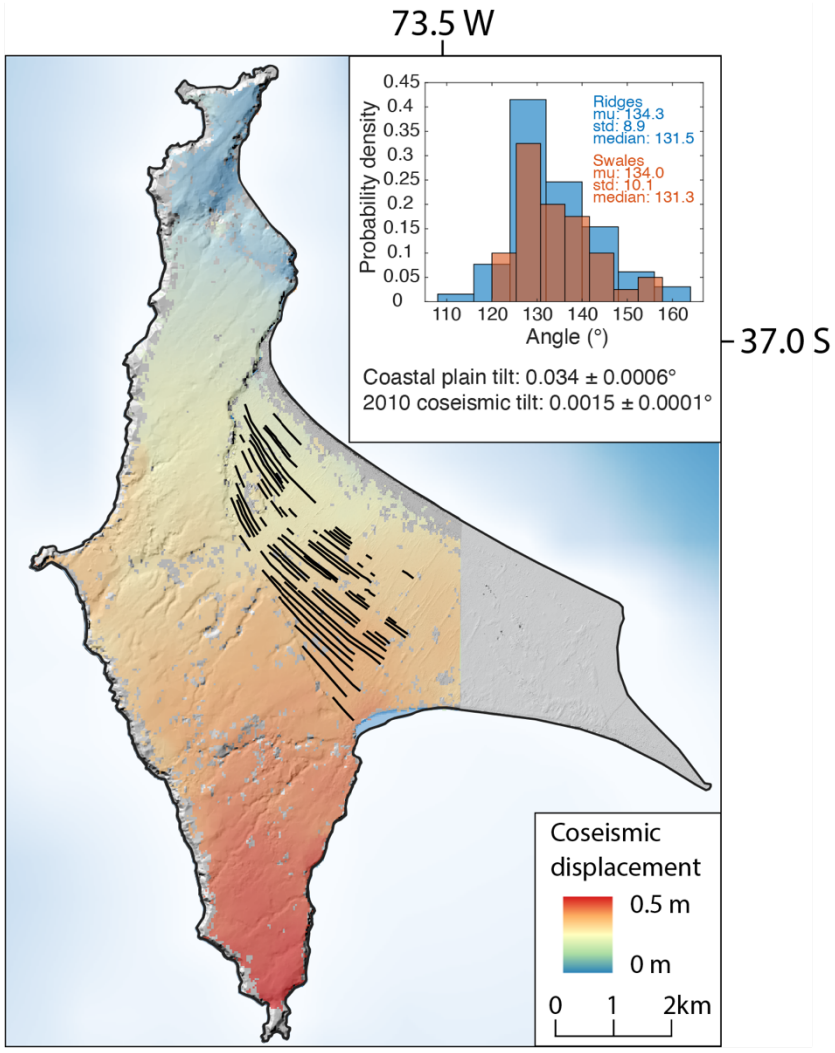

Figure S2. Deformation during the 2010 Maule earthquake at ISM (Melnick *et al.*, 2012b). Color-coded displacement from unwrapped Advanced Land Observing Satellite interferogram. Inset shows histogram of ridge/swale orientations.

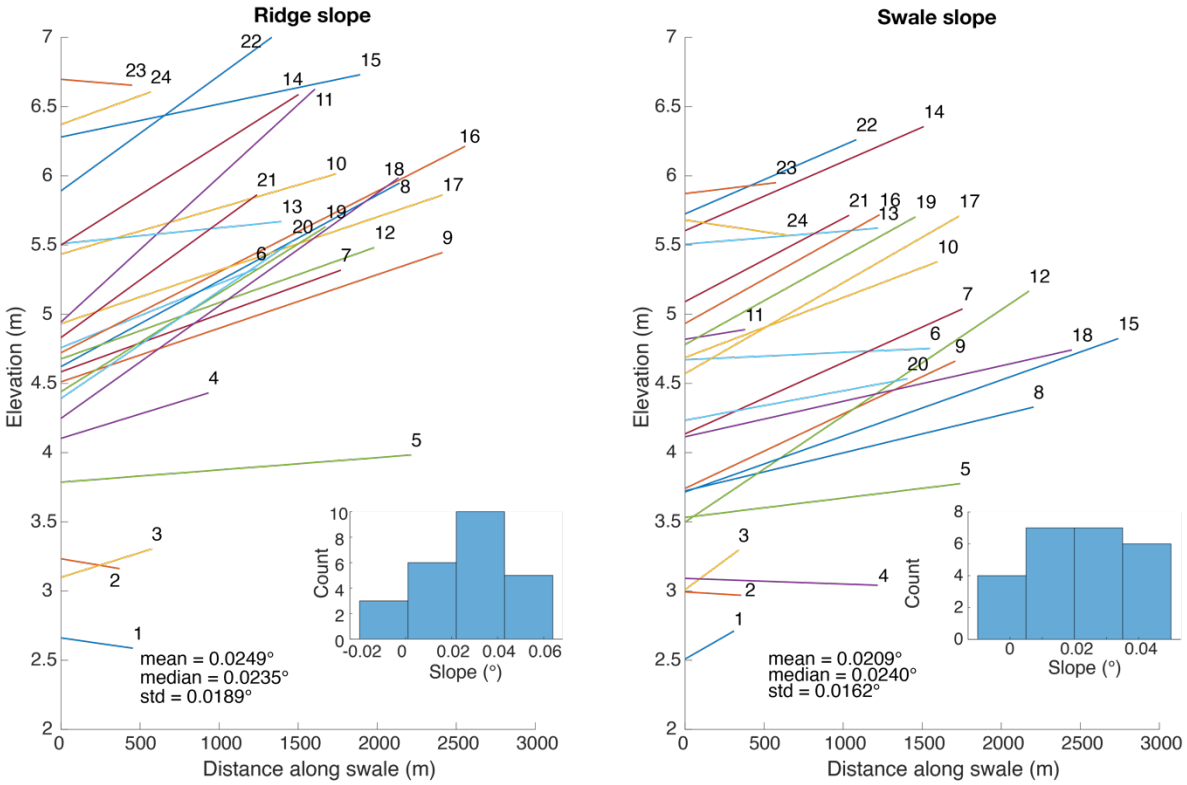

Figure S3. Stacks of ridge (left) and swale (right) tilt estimates using linear regressions. Insets show tilt histograms with labeled statistics.

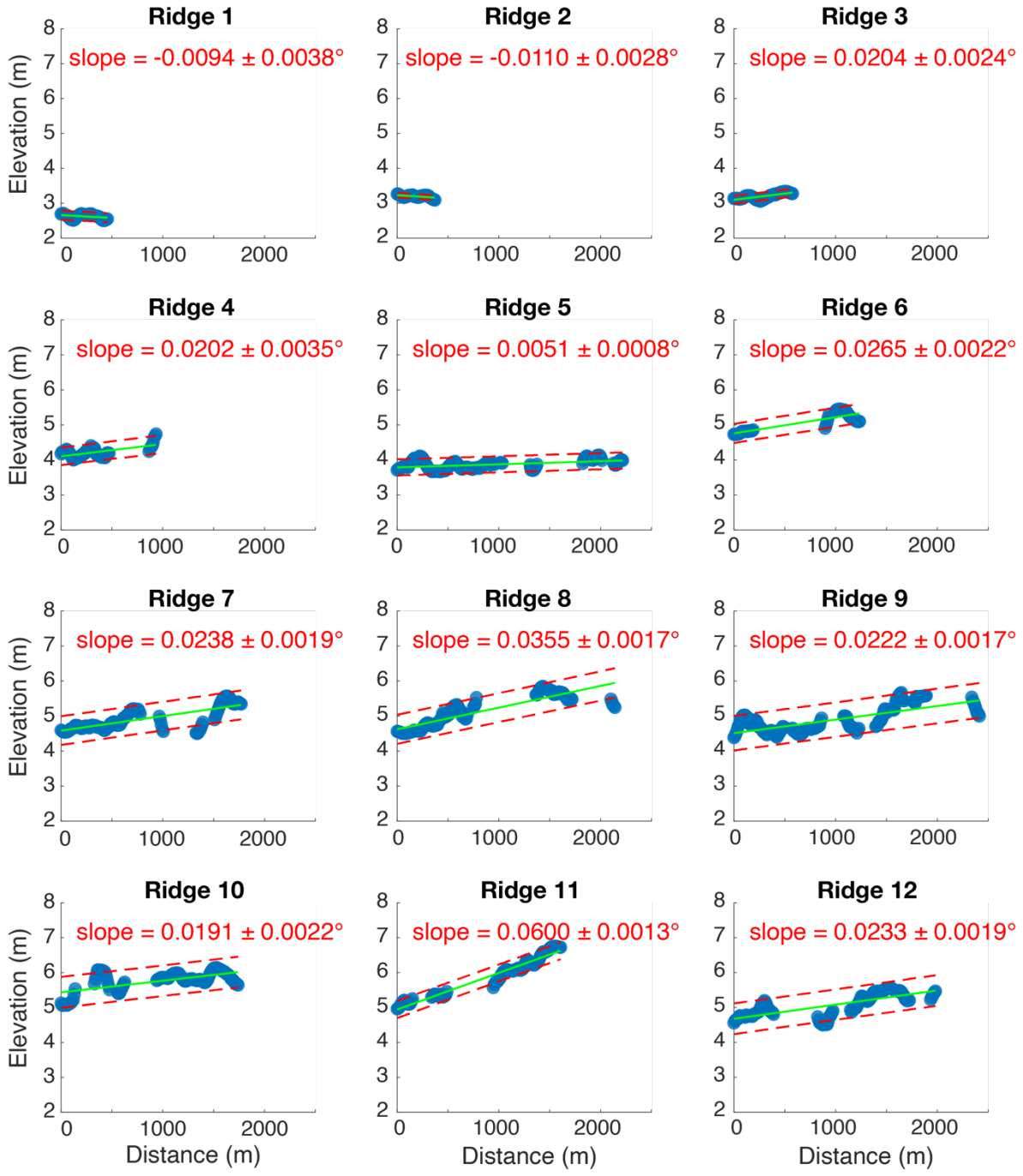

Figure S4. Linear regressions used to estimate tilt angles for individual ridge.

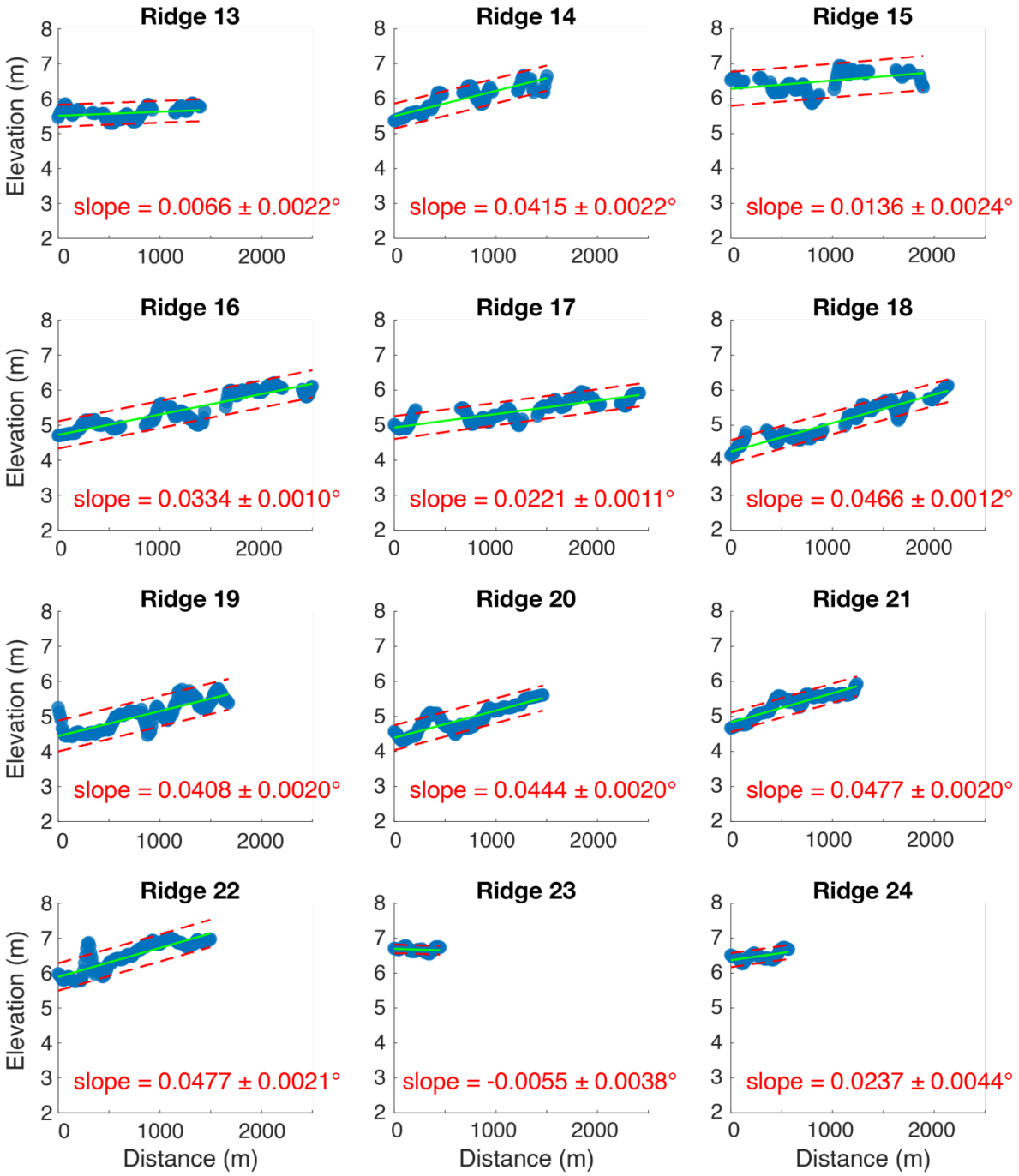

Figure S4. Linear regressions used to estimate tilt angles for individual ridge (continued).

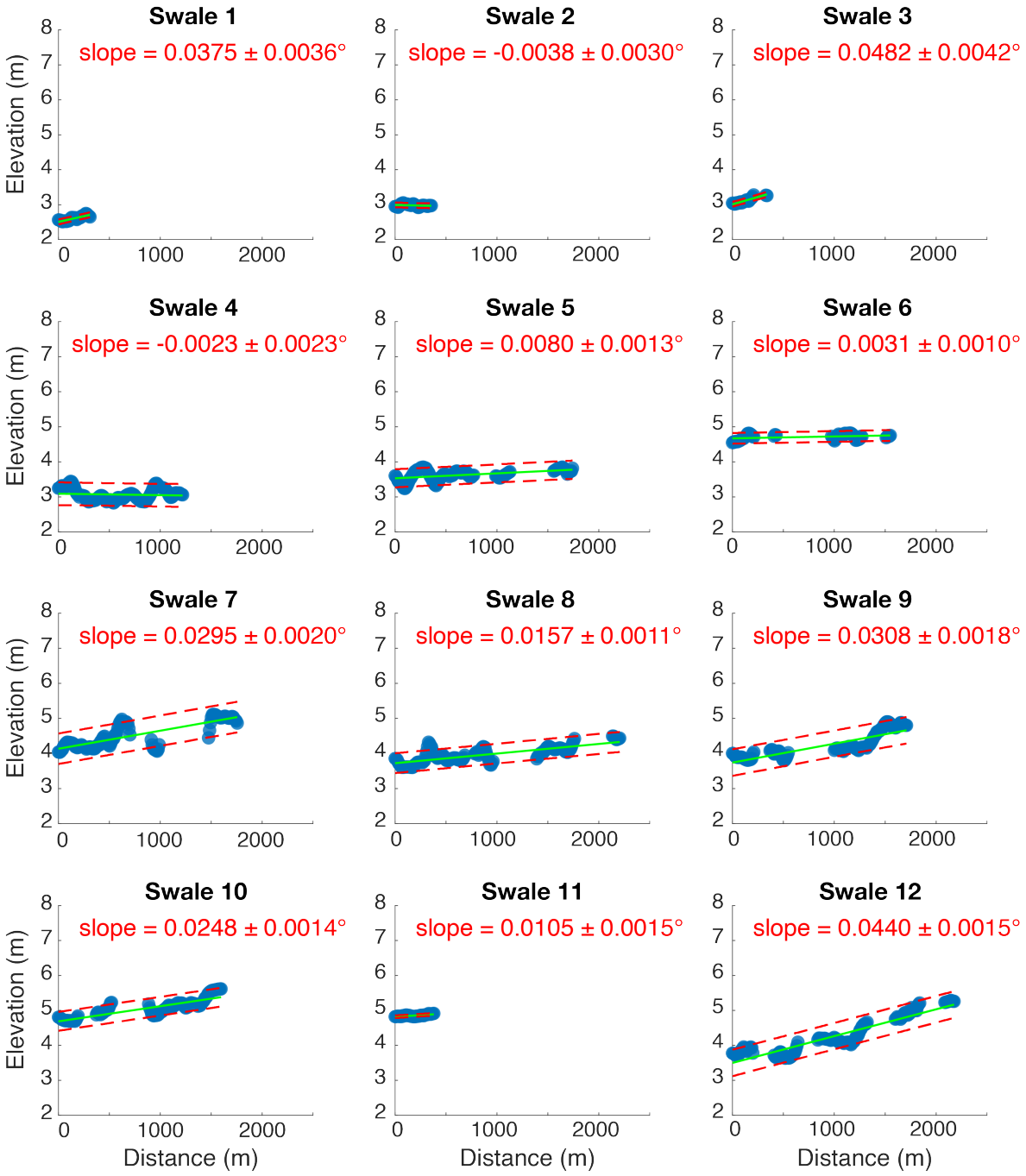

Figure S5. Linear regressions used to estimate tilt angles for individual swale.

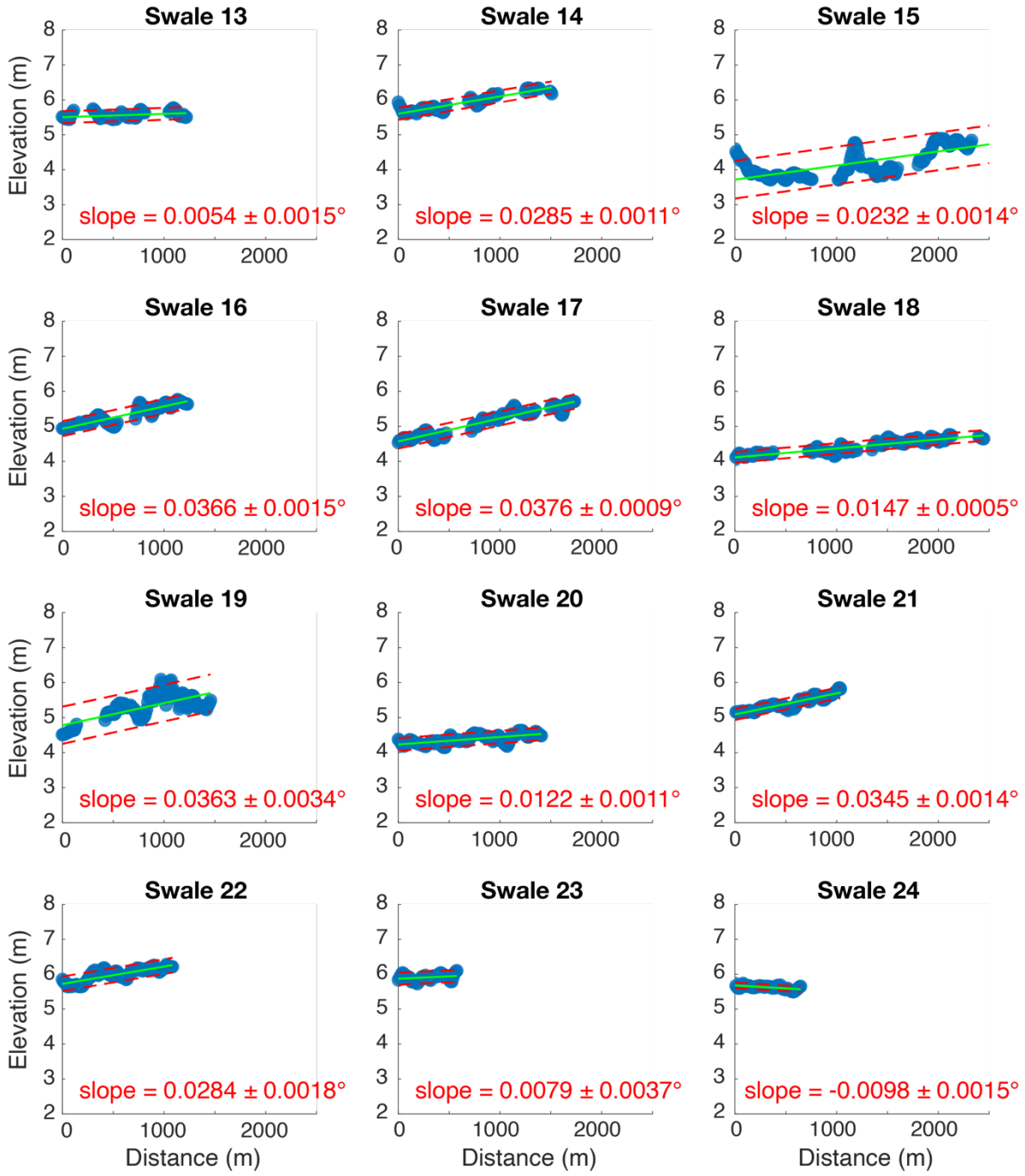

Figure S5. Linear regressions used to estimate tilt angles for individual swale (continued).

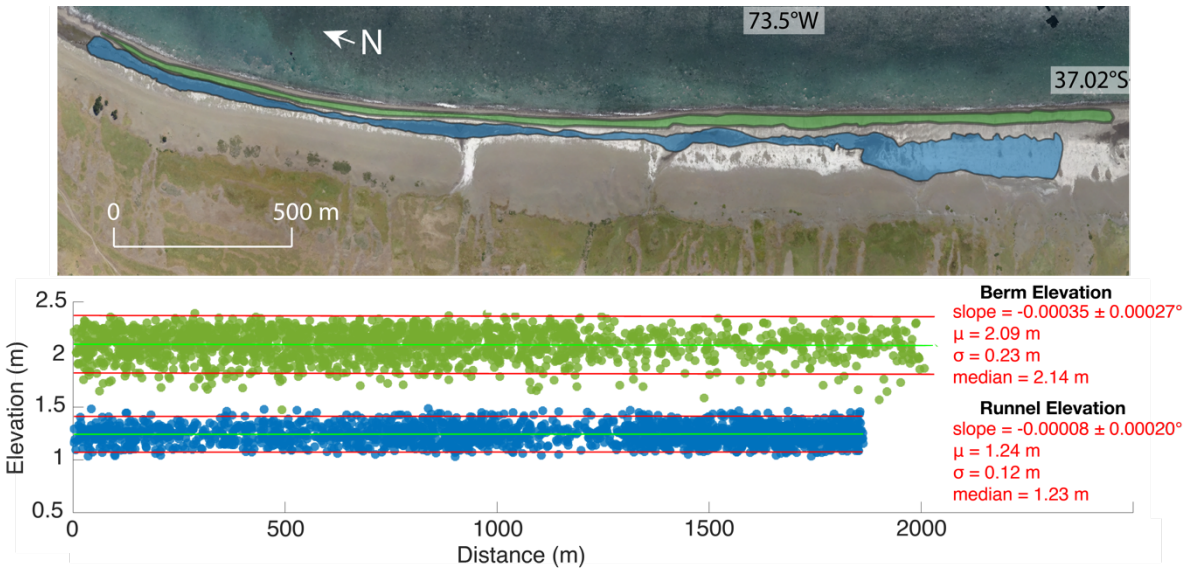

Figure S6. Elevation and extent of the modern berm and runnel calculated from 15-cm drone digital elevation model. Note both are essentially flat.

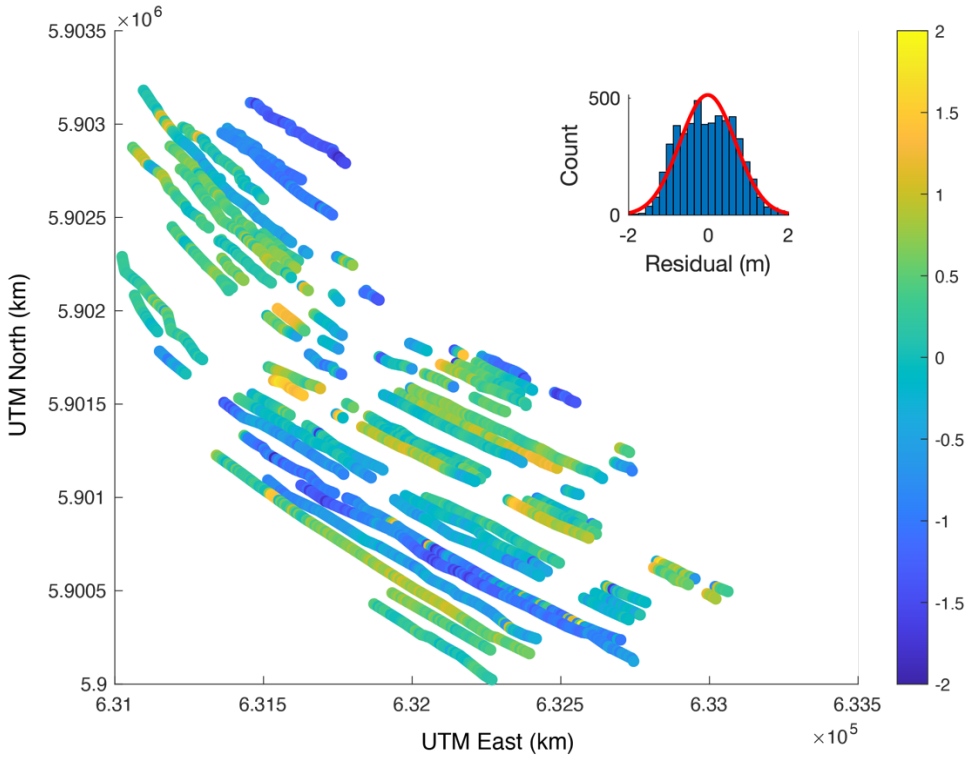

Figure S7. Map of ridge crests color-coded by residual elevation from the adjustment of a plane. Inset shows histogram of residuals and fit to a normal distribution; the X^2/X^{2crit} is below 1 suggesting residuals do not differ at 95% significance from a Gaussian distribution.

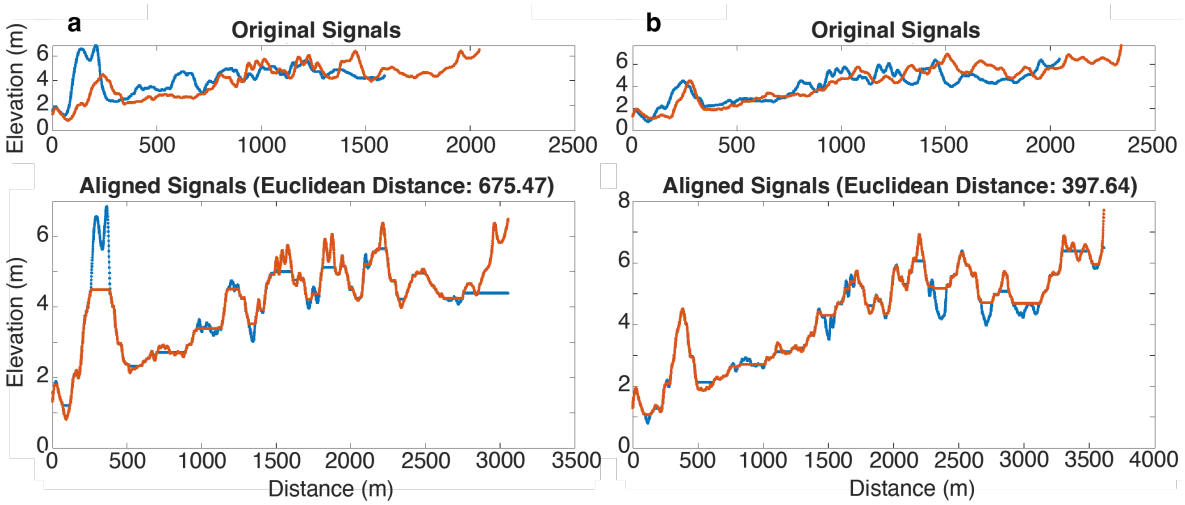

Figure S8. Construction of the composite topographic profile by aligning the three parallel profiles using a Dynamic Time Wrapper algorithm (Wang, 2023). a) Profiles 1 and 2. b) Profiles 2 and 3.

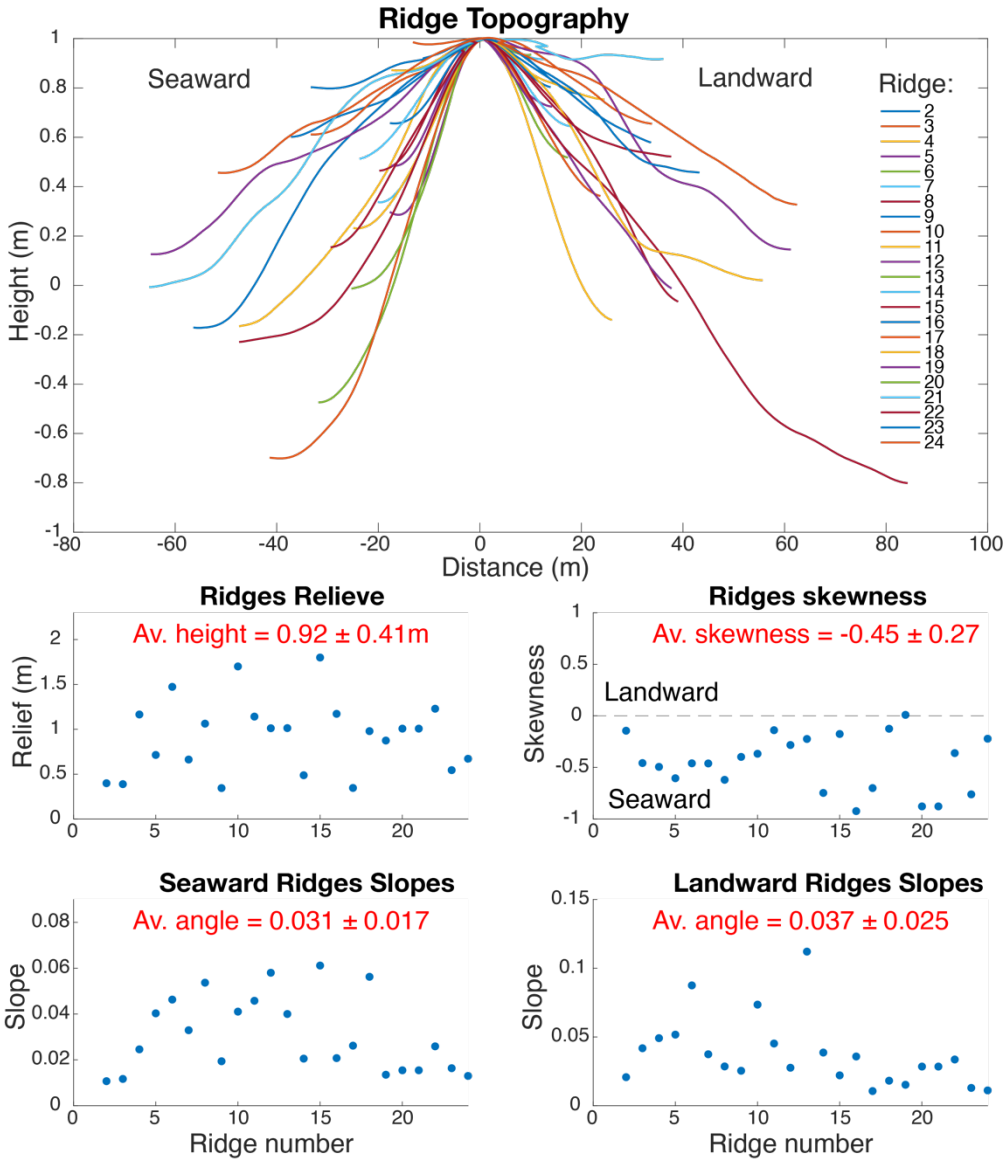

Figure S9. Top panel shows stacked topographic profiles across the 24 ridges. Ridge crests are set to 1 m elevation for stacking and visual comparison purposes. Lower panels show morphometric parameters of the 24 ridges. Note persistent asymmetry and seaward skewness suggesting analogous formation mechanisms.

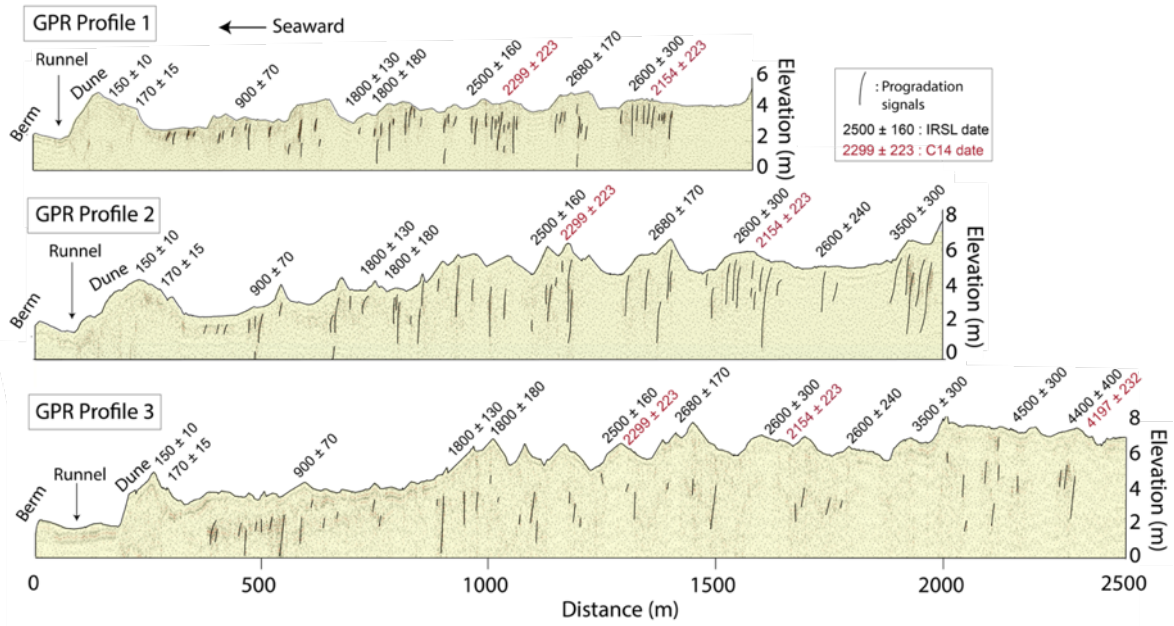

Figure S10. GPR profiles with IRSL and radiocarbon ages. Modern beach to the left with berm, runnel, and dune. Note the progradation signals inclined seaward under the ridges.

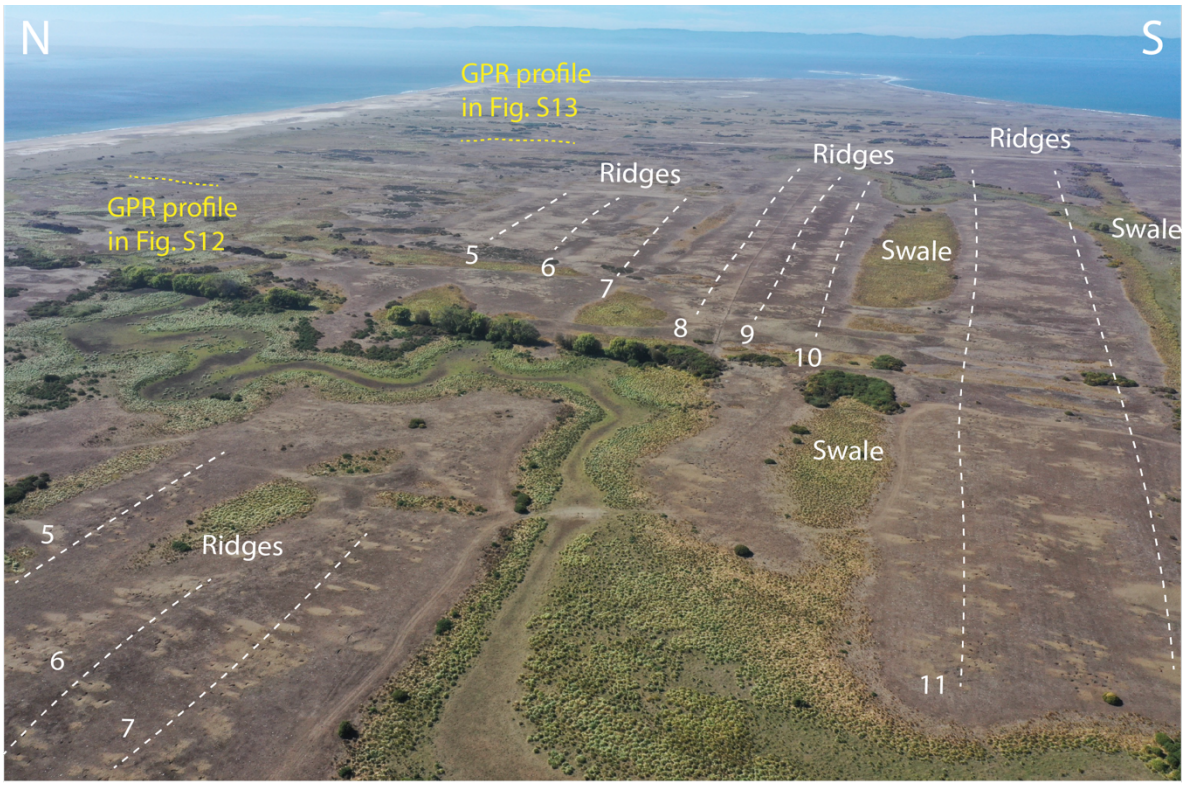

Figure S11. Oblique aerial view of the ISM coastal plain highlighting ridges numbers and swales (drone flight by D. Aedo).

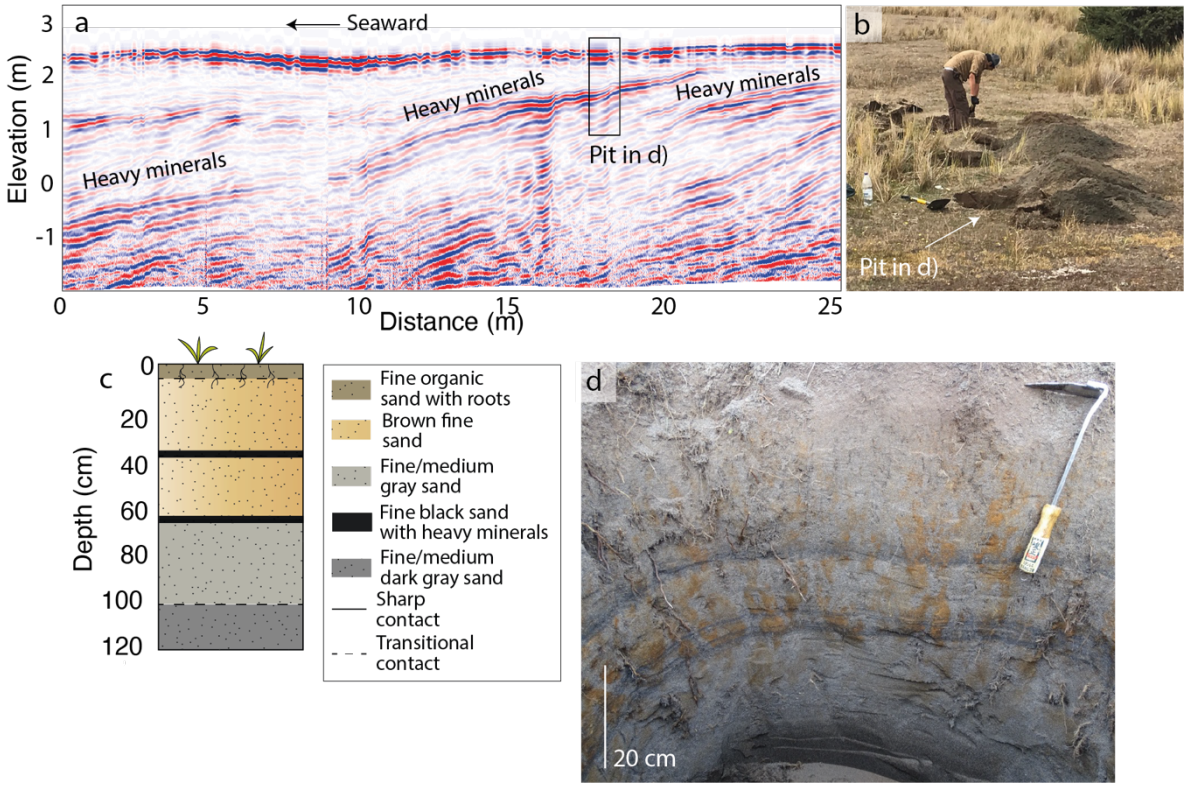

Figure S12. a) GPR profile showing monotonous sequence of progradating beach faces. Location in fig. S11. b) Excavations made in the profile shown in a). c-d) Pit stratigraphy, note the dark heavy mineral layers.

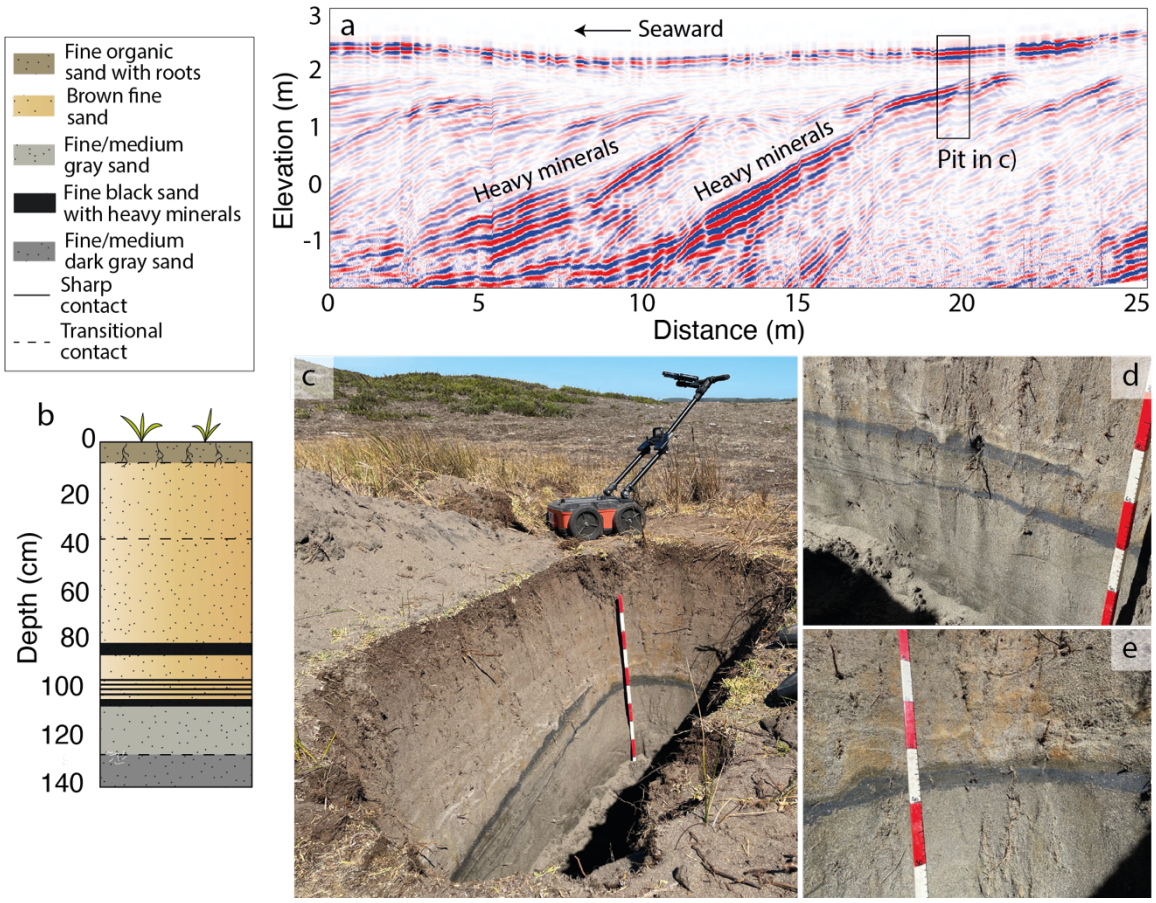

Figure S13. a) GPR profile showing monotonous sequence of progradating beach faces. Location in fig. S11. b) Pit stratigraphy, note the dark heavy mineral layers. c-e). Photos of the pit stratigraphy shown in a). Note the dark heavy mineral layers inclined seaward.

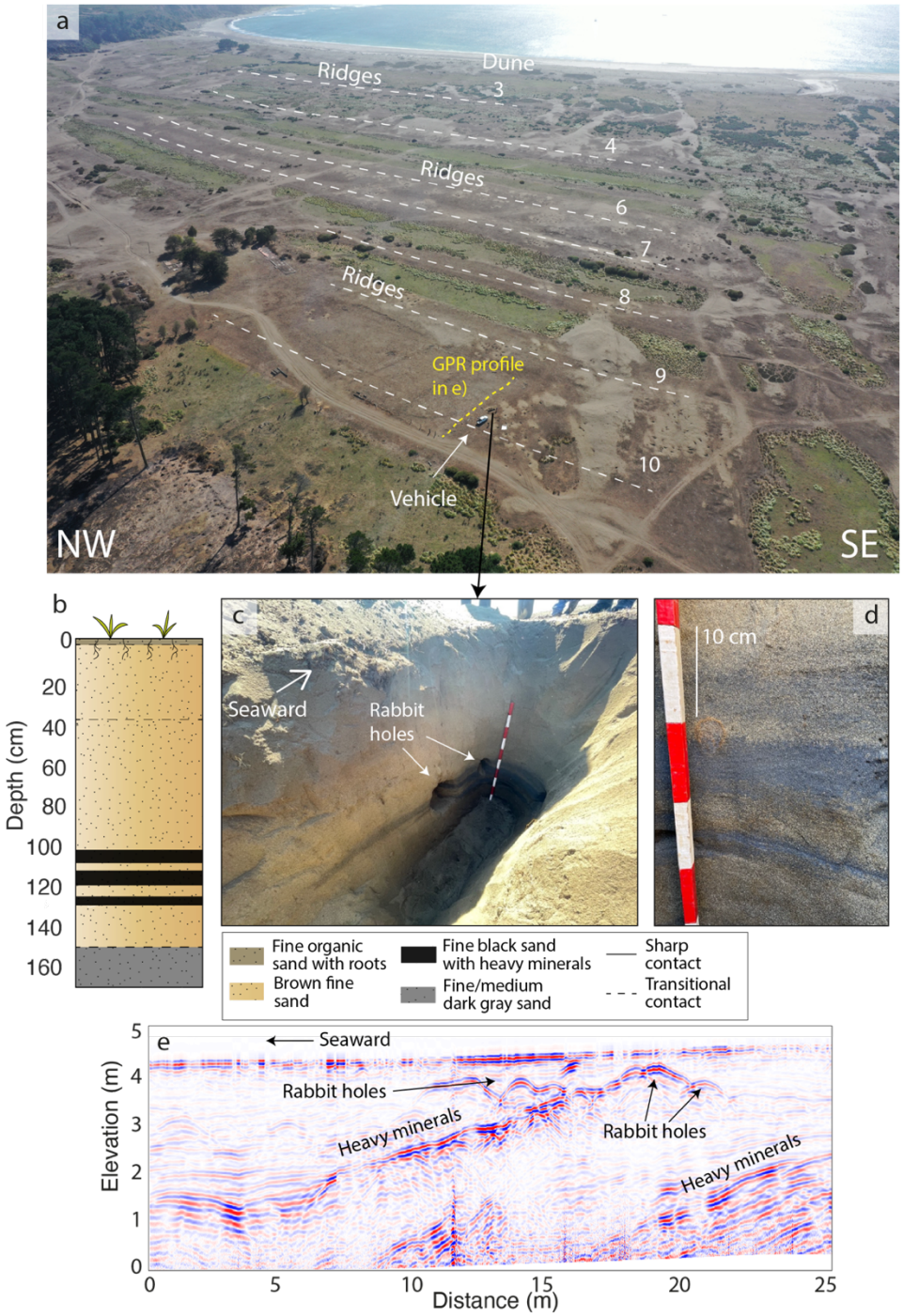

Figure S14. Aerial view of the ISM coastal plain, highlighting numbered ridges and swales (drone flight by D. Aedo), and location of GPR profile in e). b) Pit stratigraphy, note the dark heavy mineral layers. c-e). Images of the pit stratigraphy shown in a). Note the dark heavy mineral layers inclined seaward. e) GPR profile showing progradation signals.

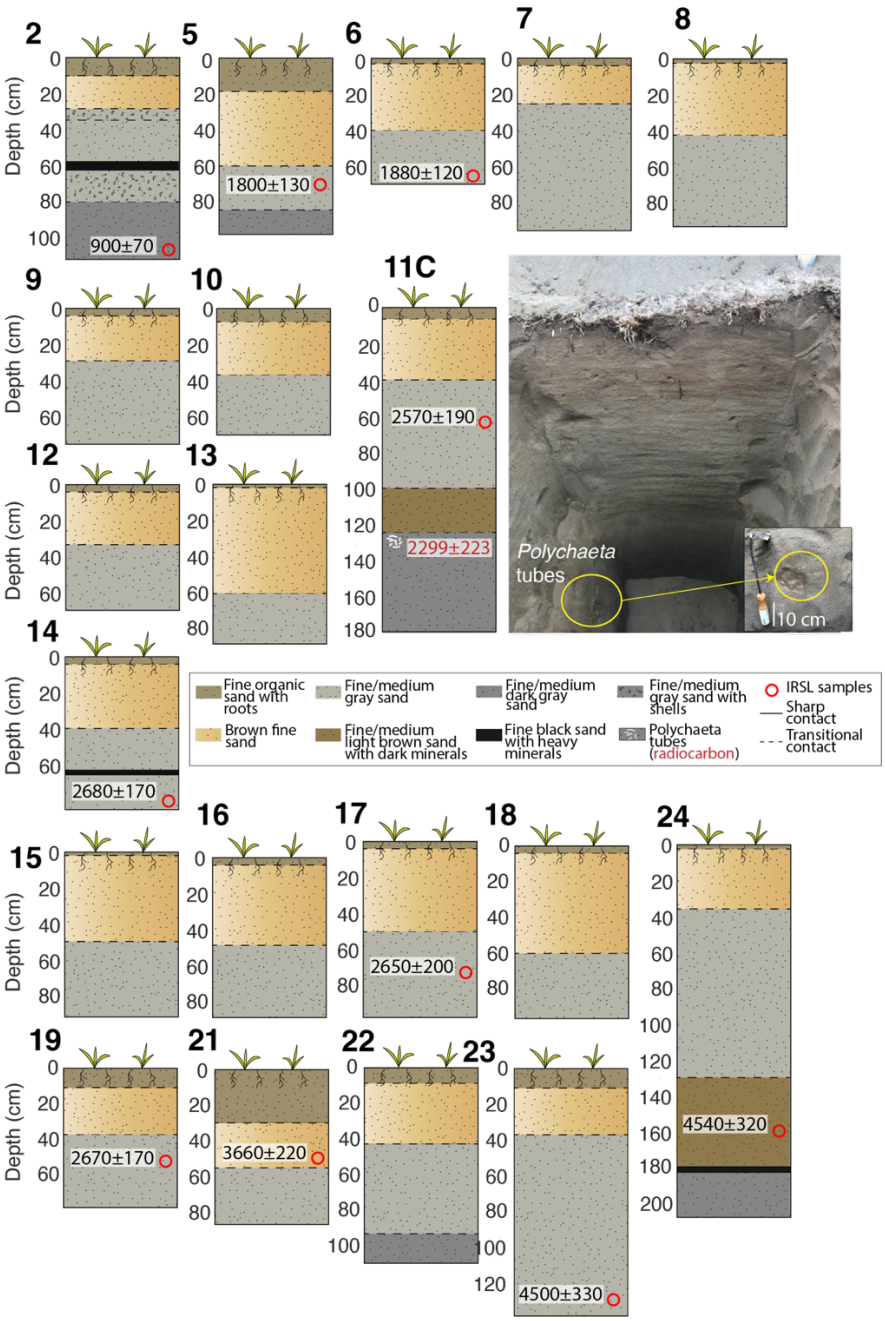

Figure S15. Stratigraphic sections of pits sampled sites for age dating. Pit 5c made on the crest of ridge 11 is highlighted in the center with the granulometry and position where the polychaete sample was taken for radiocarbon dating.

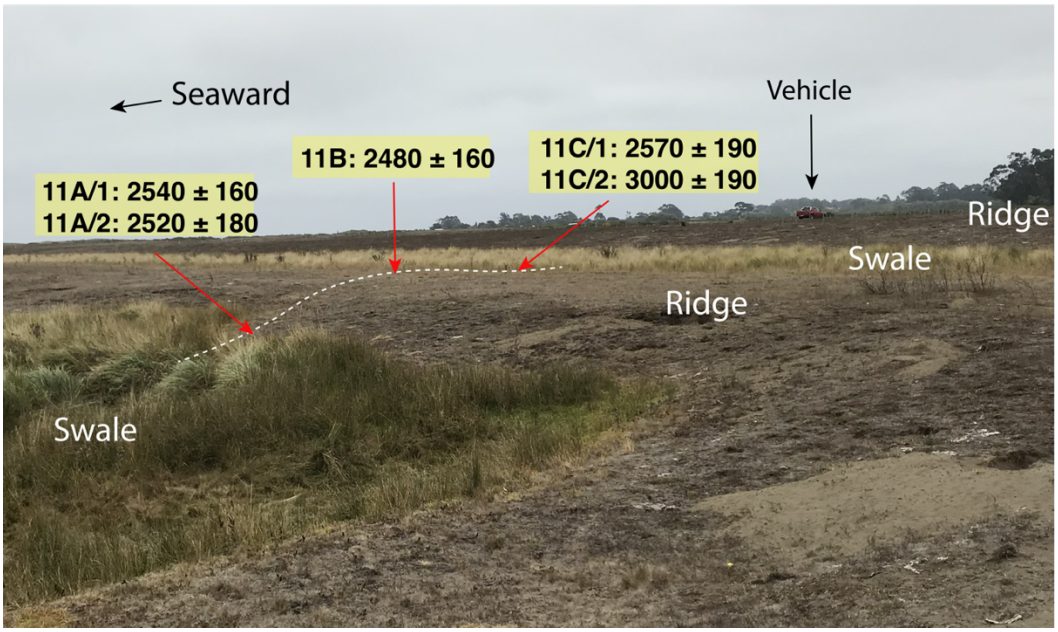

Figure S16. Ridge 11 with all IRSL ages. Note overlap within uncertainties suggesting rapid ridge abandonment.

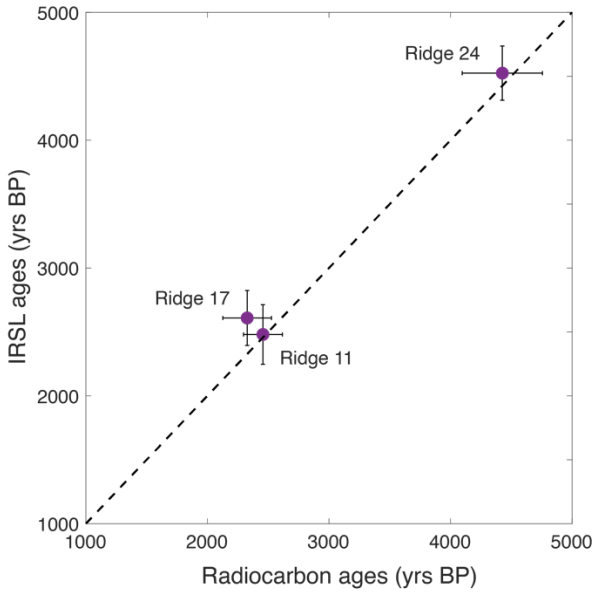

Figure S17. Comparison between IRSL and radiocarbon ages of *polychatea* tubes at ridges 11, 17 and 24. Note that radiocarbon dating of ridge 17 is younger than ridge 11 and is not consistent.

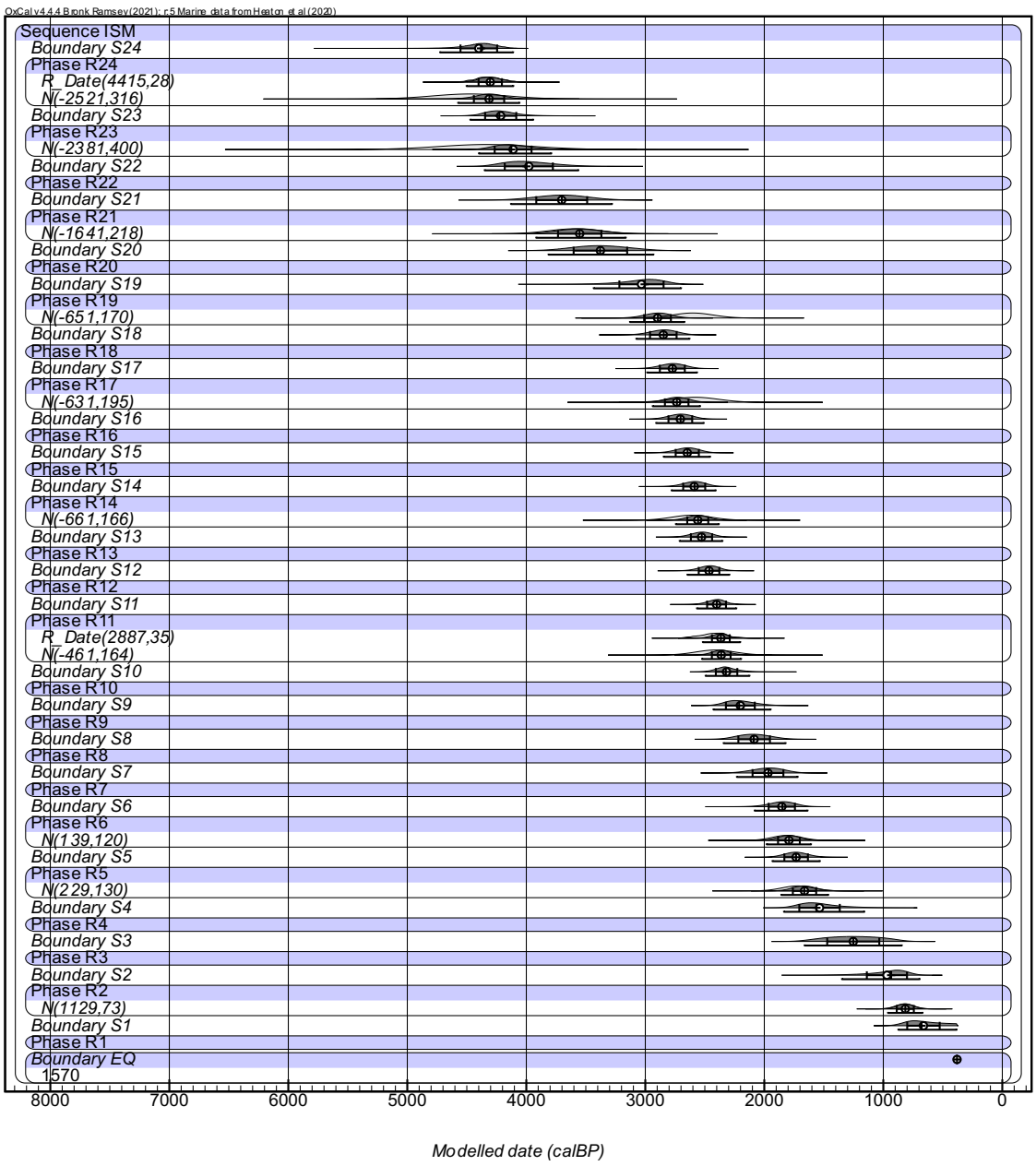

Figure S18. OxCal modeled ages.

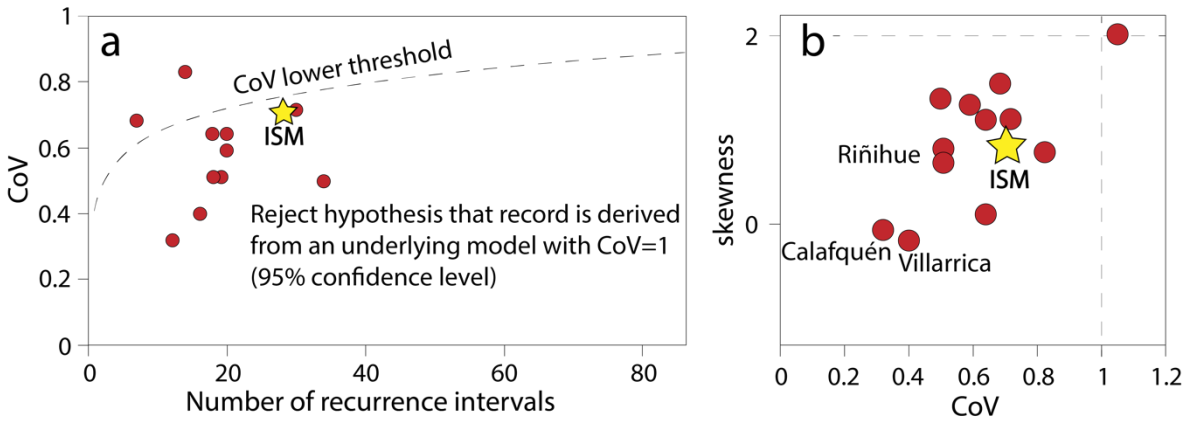

Figure S19. a) CoV and skewness of the ISM record and other subduction zones Moernaut, 2020. b) Test to determine whether the CoV can be the result of an underlying model with CoV = 1 of ISM values compared to other subduction zones (Moernaut, 2020). For records that fall outside the threshold limits, the Poissonian model can be rejected at the 95% confidence level.

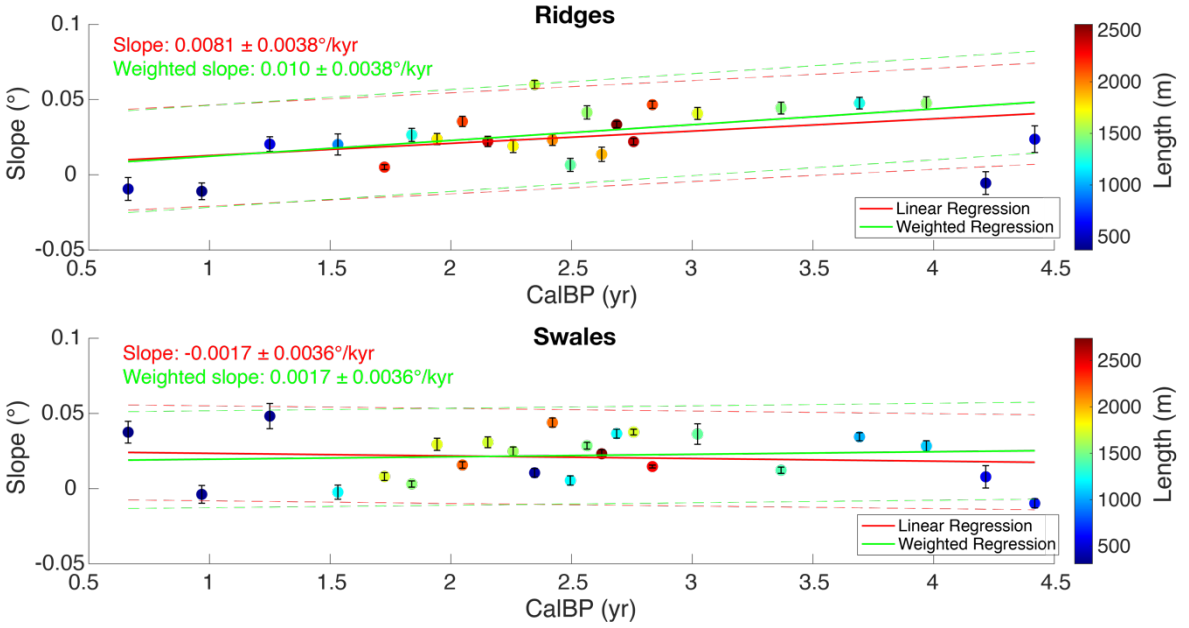

Figure S20. a) Ridges tilting rate using linear regression and weighted linear regression. b) Swale tilting rate using linear regression and weighted linear regression level.

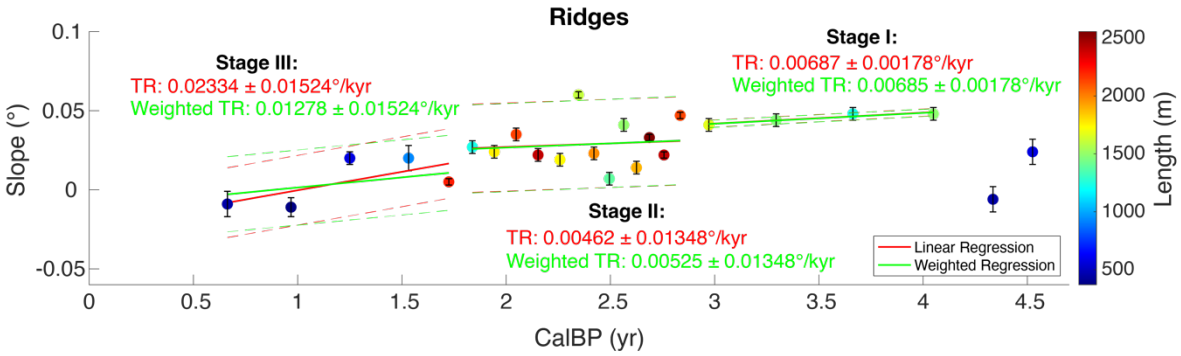

Figure S21. Tilt rate estimated using linear regression and weighted linear regression for the three stages of the beach ridge plain.

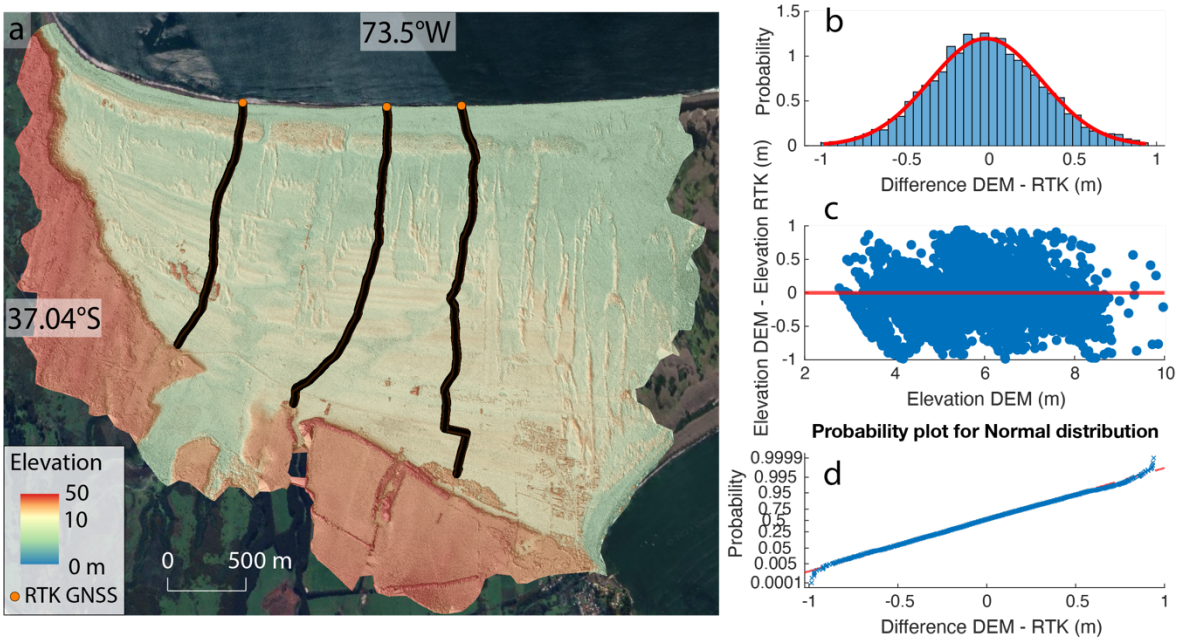

Figure S22. a) ISM coastal plain topography obtained from Ebee drone photogrammetry showing location of the three RTK GNSS control point profiles. b) Histogram with difference between DEM and RTK elevations. c) Comparison between difference between DEM and RTK elevations and DEM elevations. d) Probability plot for Normal distribution of difference between DEM and RTK elevations.

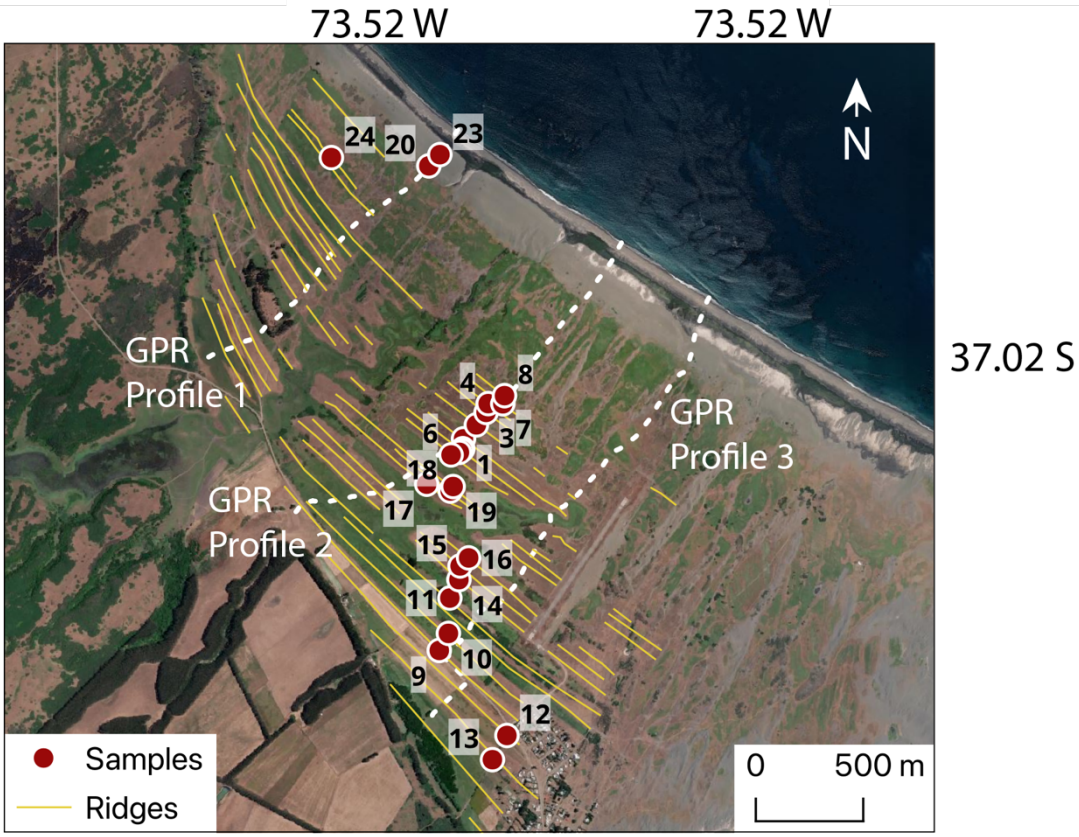

Figure S23. Location of all samples collected for age dating and GPR profiles.

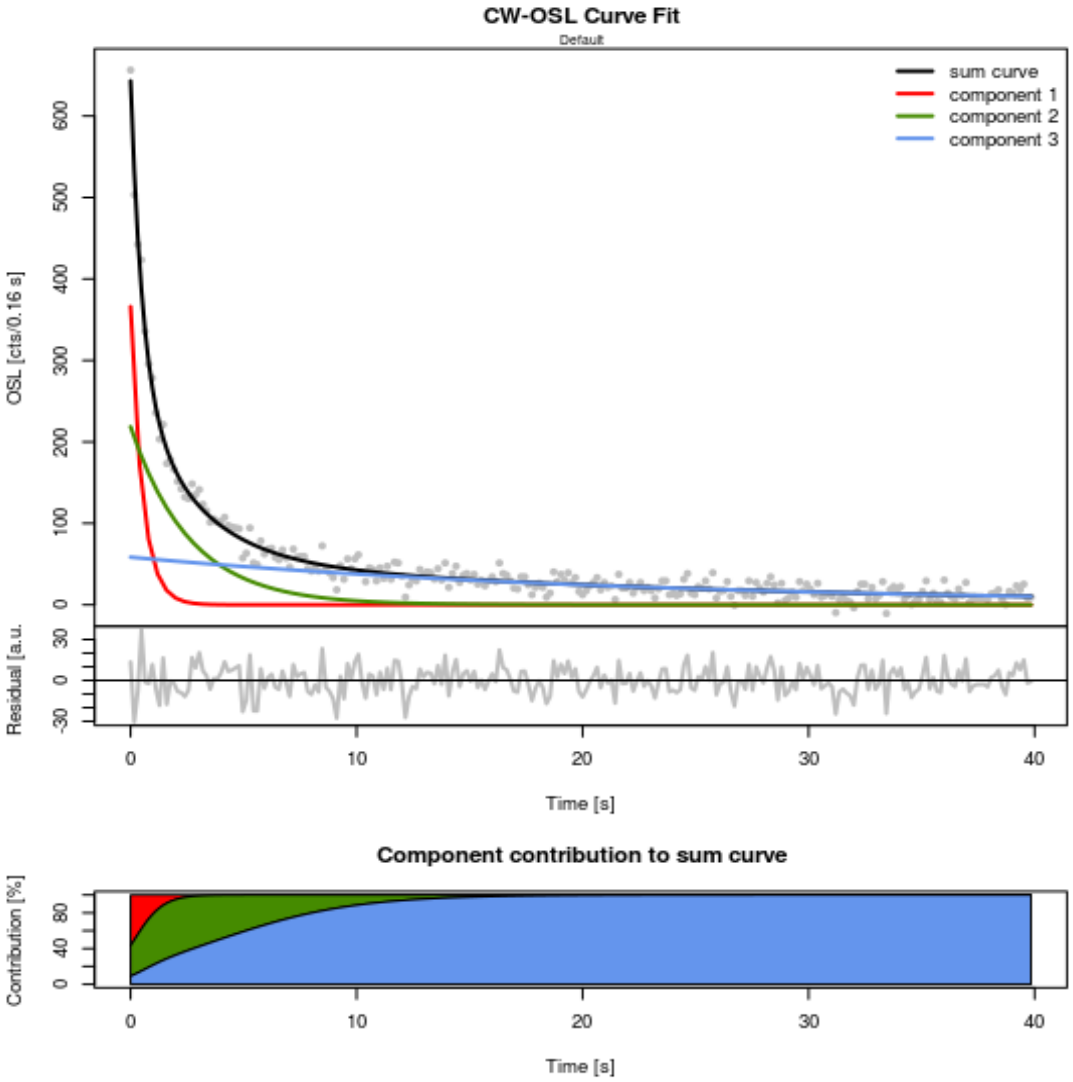

Figure S24. Contributions of signal components to quartz luminescence signals from ISM. A stable fast component (component 1) is present, but there is a strong contribution (~ 20% even when early background subtraction is used) of an unstable medium component (component 2) in all samples. Fitting was performed with the R-package "Luminescence" (Kreutzer *et al.*, 2023).

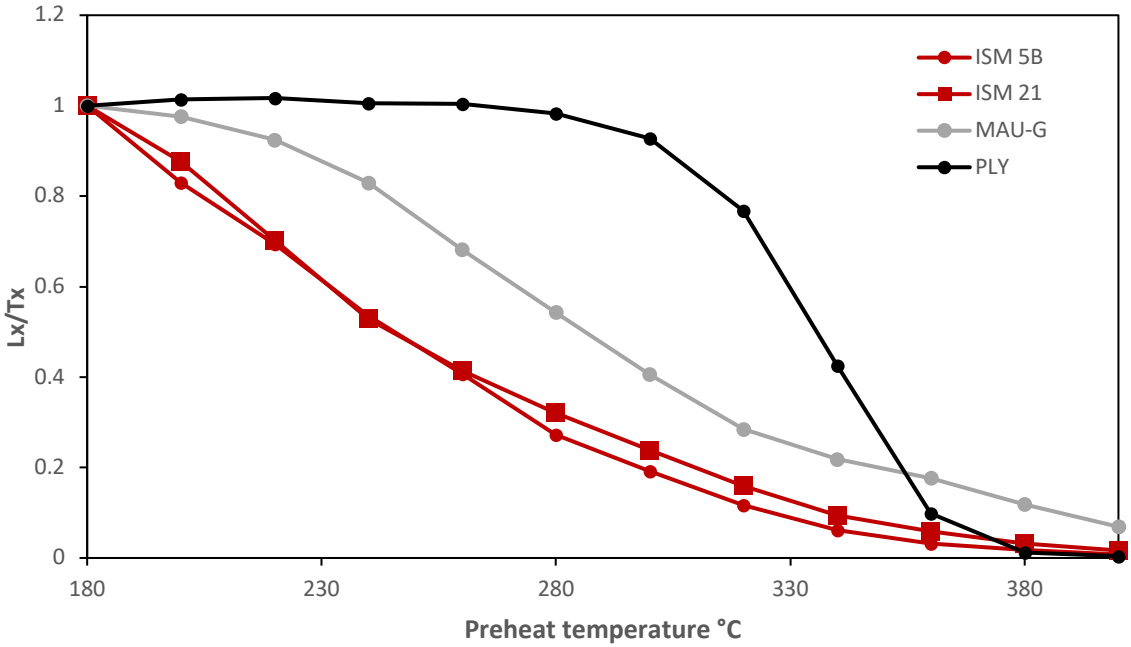

Figure S25. Pulse annealing experiment for two quartz samples from ISM in comparison with an Australian quartz sample with perfect signal behavior (PLY 25-1) and a quartz sample from Maullín, Chile with proven thermal instability (Brill *et al.*, 2017; Brill & Cisternas, 2020).

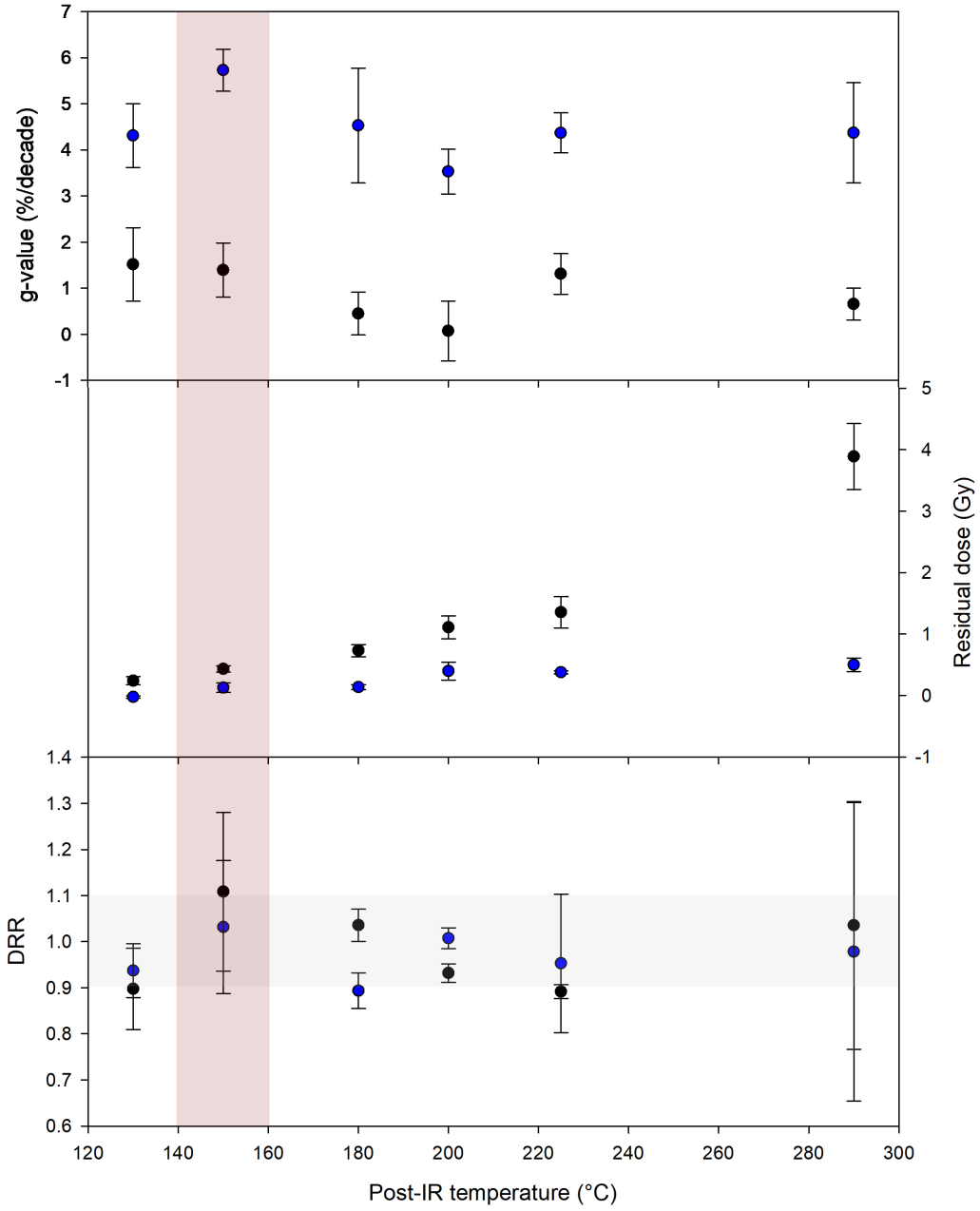

Figure S26. Preheat experiment for selecting suitable post-IRSL-IRSL protocol for the ISM samples. For post-IRSL temperatures of 130, 150, 180, 200, 225 and 290 °C batches of 3 aliquots (2 mm diameter) each were measured to determine temperature-dependent dose recovery ratios (DRR; note: for DRR of post-IRSL signals residuals have been subtracted), residual doses and g-values. IRSL signals within the different post-IRSL protocols are shown with blue, post-IRSL signals with black symbols. The post-IRSL protocol measured at 150 °C (post-$IRSL_{150}$), that was selected for further measurements, is highlighted in red.

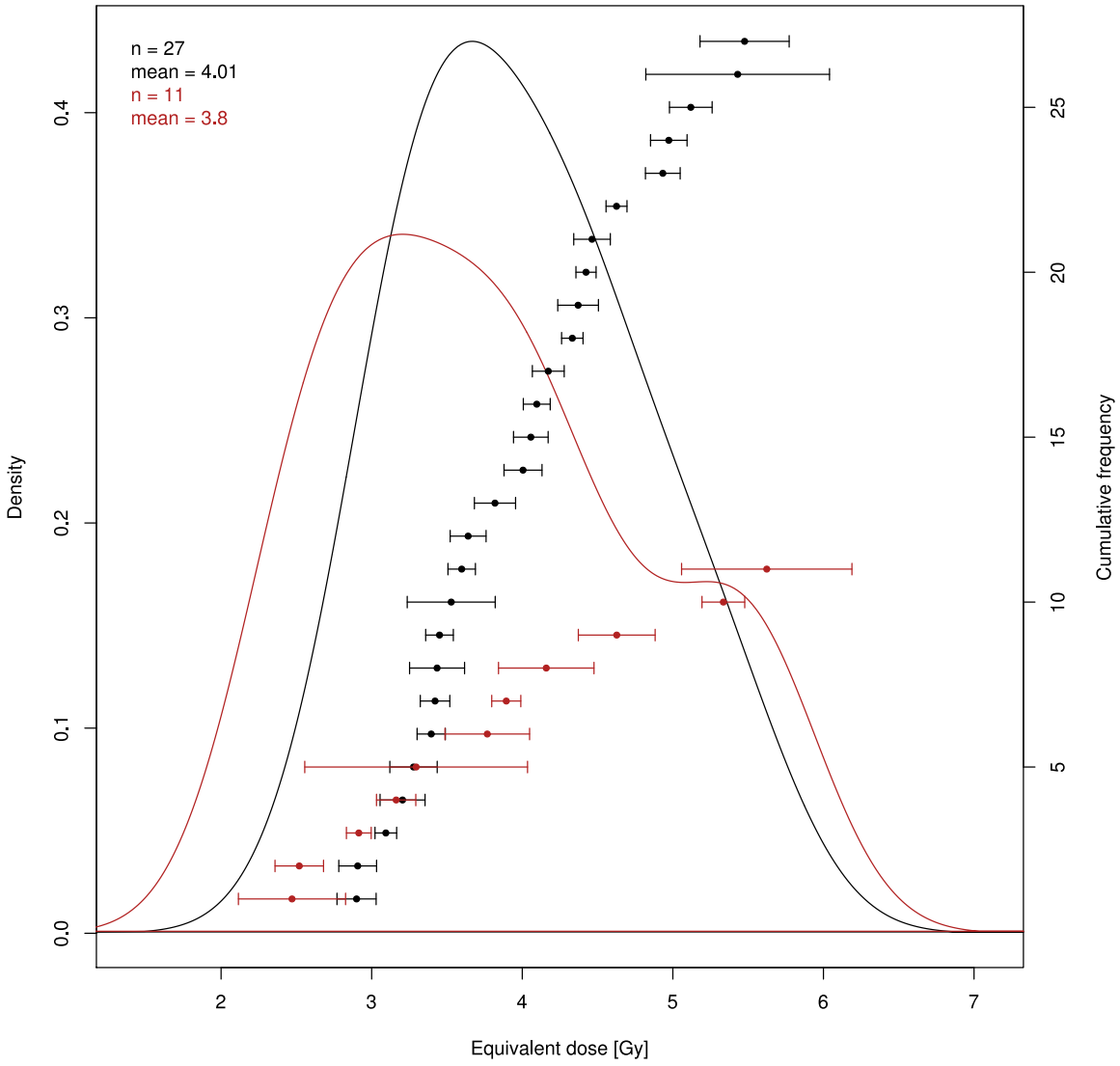

Figure S27. Equivalent dose distribution of IRSL signals from sample ISM 5B. Shape of the distributions (~normal distribution) and agreement between 1-mm aliquots (red) and 2-mm aliquots (black) indicates complete luminescence signal.

Supporting Tables

Table S1. Samples collected for dating in each ridge. The coordinates, depth and type of dating applied to each sample are shown.

Ridge	Sample	X	Y	Sample depth (m)	OSL (yrs)	OSL error (yrs)	C14 (yr BP)	C14 error (yrs)	IRSL (yrs)	IRSL error (yrs)	pIRIR (yrs)	pIRIR error (yrs)
24	24	632306	5899961	1.6			4415	28	4540	320	5200	400
23	23	632373	5900074	1.3					4500	330	5600	350
22	22	632058	5900470	0.75								
21	21	632101	5900549	0.5	2500	300			3660	220	4000	250
20	-	-	-	-								
19	19	632107	5900714	0.55					2670	170	2800	200
18	18	632150	5900799	0.8								
17	17	632155	5900863	0.75			2773	34	2650	200	2900	250
16	16	632195	5900901	0.7								
15	15	632000	5901244	0.7								
14	14	632109	5901212	0.8					2680	170	3000	210
13	13	632123	5901233	0.8								
12	12	632113	5901380	0.57								
11	11A/1 front	632168	5901409	0.7					2540	160		
	11A/2 front	632168	5901409	2.1					2520	180		
	11B top	632163	5901401	0.8	2100	140	2887	35	2480	160	2900	200
	11C/1 back	632152	5901392	0.6					2570	190		
	11C/2 back	632152	5901392	1.3					3000	190		
10	10	632171	5901455	0.55								
9	9	632231	5901520	0.65								
8	8	632276	5901578	0.65								
7	7	632286	5901619	0.7								
6	6	632354	5901618	0.7	1900	130			1880	120	2300	230
5	5	632362	5901656	0.7					1800	130	1720	140
4	-	-	-	0.8								
3	-	-	-	1.1								
2	2	631556	5902764	1.1					900	70	1300	90
1	-	-	-	-								
Dune 1	D1	632010	5902726	0.4					170	15	440	50
Dune 2	D2	632061	5902778	0.1					150	10	450	110

Table S2. Summary of dose information for luminescence dating of quartz and feldspar (IRSL and pIR150). OD – over-dispersion, Age unc. – age not corrected for fading, Age cor. – Age corrected for fading using a mean g-value of 4.2 ± 0.1 %/decade. IRSL-based luminescence ages used for chronological interpretations are highlighted.

Sample	*Ridge*	*Lab-ID*	*Signal*	*Size (mm)*	*N*	*OD (%)*	*Dose (Gy)*	*Age unc. (ka)*	*g-value (%/dec)*	*Age cor. (ka)*
ISM 2	2	C-L4853	IRSL	2	20	18.8±3.8	1.36±0.07	0.637±0.048	4.6±0.4	0.89±0.073
			pIR150	2	15	8.3±3.4	2.74±0.1	1.283±0.085	-0.3±0.1	-
ISM 5	5	C-L4837	IRSL	2	20	16.1±2.9	2.76±0.11	1.274±0.087	4.3±0.3	1.79±0.13
			pIR150	2	7	11.7±5.9	3.73±0.23	1.722±0.143	1.2±0.1	-
ISM 6	6	C-L4836	Quartz	8	14	19±4.6	2.98±0.17	1.875±0.132	-	-
			IRSL	2	20	11.3±2.2	2.94±0.08	1.326±0.081	3.2±0.5	1.88±0.12
			pIR150	2	14	29.5±6.3	5.01±0.42	2.26±0.226	0.4±0.6	-
ISM 11A1	11	C-L4830	IRSL	2	21	12.6±2.2	3.91±0.12	1.783±0.112	4.3±0.2	2.54±0.158
			pIR150	2	19	20.1±3.9	6.85±0.35	3.123±0.234	-2±1.2	-
ISM 11A2	11	C-L4831	IRSL	2	21	14.8±2.6	3.82±0.13	1.768±0.115	4.4±0.2	2.52±0.18
			pIR150	2	15	8.9±2.3	6.24±0.18	2.888±0.18	-0.6±1.5	-
ISM 11B	11	C-L4832	Quartz	8	22	24.6±4	3.27±0.18	2.095±0.144	-	-
			IRSL	2	27	15.6±2.5	3.94±0.13	1.737±0.112	4.5±0.4	2.48±0.164
			pIR150	2	21	13.7±3.1	6.5±0.24	2.912±0.191	1.4±0.6	-
ISM 11C1	11	C-L4833	IRSL	2	18	17.5±3.4	3.96±0.18	1.8±0.128	4.2±0.4	2.57±0.19
			pIR150	2	15	31.9±6.6	5.36±0.47	2.436±0.252	0.4±0.6	-
ISM 11C2	11	C-L4834	IRSL	2	20	9.6±1.7	4.55±0.1	2.09±0.124	4.7±0.3	2.99±0.19
			pIR150	2	15	8.3±2	6.78±0.16	3.115±0.186	3.1±1.3	-
ISM 14	14	C-L4847	IRSL	2	19	10.3±2.1	4.25±0.11	1.882±0.113	4.6±0.4	2.68±0.166
			pIR150	2	18	16.7±3.5	6.73±0.3	2.981±0.209	2.7±0.6	-
ISM 17	17	C-L4844	IRSL	2	17	15.2±3	4.04±0.16	1.862±0.126	4.7±0.5	2.65±0.195
			pIR150	2	15	21.7±4.8	6.18±0.38	2.849±0.235	4.8±1.4	-
ISM 19	19	C-L4840	IRSL	2	19	12.1±2.3	4.34±0.13	1.866±0.114	3.9±0.6	2.67±0.17
			pIR150	2	11	14±4.4	6.53±0.34	2.807±0.209	1.6±0.8	-
ISM 21	21	C-L4839	Quartz	8	14	47.4±9	3.91±0.5	2.524±0.339	-	-
			IRSL	2	19	8.5±1.8	5.55±0.13	2.546±0.152	2.7±0.2	3.66±0.218
			pIR150	2	11	4.7±4.1	8.66±0.26	3.969±0.248	0.2±0.6	-
ISM 23	23	C-L4841	IRSL	2	22	14.7±2.5	6.28±0.21	3.097±0.205	4.5±0.5	4.48±0.327
			pIR150	2	14	5.2±4	11.43±0.35	5.637±0.365	0.9±0.8	-
ISM 24	24	C-L4842	IRSL	2	19	15.8±2.8	6.76±0.26	3.139±0.212	3.7±0.7	4.54±0.316
			pIR150	2	8	15.4±4.7	11.14±0.67	5.172±0.423	0.3±0.9	-
ISM D1	Dune/1	C-L4849	Quartz	8	17	23.8±6.3	0.46±0.03	0.292±0.023	-	-
			IRSL	2	17	24.9±7.2	0.29±0.02	0.132±0.012	4.3±0.4	0.174±0.014
			pIR150	2	15	32.2±7.3	0.96±0.09	0.436±0.047	2.1±0.5	-
ISM B1	Beach	C-L4850	Quartz	8	15	19.5±4	1.04±0.06	0.607±0.043	-	-
			IRSL	2	20	58.6±16.6	0.15±0.02	0.064±0.009	4.5±0.3	0.079±0.014
			pIR150	2	13	33±8.6	0.77±0.08	0.329±0.038	-0.7±1.2	-
ISM B2	Beach	C-L4851	IRSL	2	19	46.1±9.6	0.18±0.02	0.081±0.01	4.5±0.5	0.106±0.014
			pIR150	2	16	46.6±10.5	0.7±0.09	0.315±0.044	1.9±0.1	-
ISM D2	Dune/2	C-L4852	IRSL	2	20	35.6±9	0.26±0.03	0.113±0.014	3.4±0.7	0.148±0.014
			pIR150	2	7	57.2±17.1	1.04±0.24	0.451±0.107	1.8±0.5	-

Table S3. Protocols for quartz (a) and feldspar (b) dose determination. R1-x = regeneration doses, RR = recycling dose, DR = depletion ratio, R0 = zero dose (recuperation).

a) Quartz SAR protocol

Step	Treatment	Signal
1	Preheat (180 °C for 10 s)	
2	Blue LEDs (40 s @ 125 °C)	Lx (OSL)
3	Test dose	
4	Cutheat (160 °C)	
5	Blue LEDs (40 s @ 125 °C)	Tx (OSL)
6	Dose (R1-R4, R0, RR, DR)	
7	Return to step 1	

b) pIRIR150 protocol for potassium feldspar

Step	Treatment	Signal
1	Preheat (180 °C for 60 s)	
2	IR LEDs (200 s @ 50 °C) for SA	Lx (IR_{50})
3	IR LEDs (200 s @ 150 °C) for SA	Lx ($pIRIR_{150}$)
4	Test dose	
5	Preheat (180 °C for 60 s)	
6	IR LEDs (200 s @ 50 °C) for SA	Tx (IR_{50})
7	IR LEDs (200 s @ 150 °C) for SA	Tx ($pIRIR_{150}$)
8	IR LEDs (100 s @ 200 °C)	
9	Dose (R1-R4, R0, RR)	
10	Return to step 1	

Table S4. Summary of dose rate (DR) information for IRSL luminescence dating.

Sample	Lab-ID	U (ppm)	Th (ppm)	K (%)	Water (mass-%)	Cosmic DR (Gy/ka)	Internal DR (Gy/ka)	External DR (Gy/ka)	Total DR (Gy/ka)
ISM 2	C-L4853	0.9±0.05	3.07±0.19	0.96±0.01	5±22	0.18±0.02	0.54±0.1	1.6±0.07	2.14±0.12
ISM 5	C-L4837	0.91±0.06	3.48±0.22	0.95±0.01	5±11	0.19±0.02	0.54±0.1	1.63±0.07	2.17±0.12
ISM 6	C-L4836	0.89±0.06	3.32±0.21	1.02±0.01	5±10	0.19±0.02	0.54±0.1	1.68±0.07	2.22±0.12
ISM 11A1	C-L4830	0.91±0.06	3.36±0.21	1±0.01	5±5	0.19±0.02	0.54±0.1	1.67±0.07	2.21±0.12
ISM 11A2	C-L4831	0.92±0.06	3.33±0.21	1.12±0.01	5±6	0.15±0.02	0.54±0.1	1.75±0.08	2.29±0.12
ISM 11B	C-L4832	0.89±0.06	3.27±0.21	1±0.01	5±7	0.18±0.02	0.54±0.1	1.65±0.07	2.19±0.12
ISM 11C1	C-L4833	0.93±0.06	3.39±0.21	1.09±0.01	5±8	0.19±0.02	0.54±0.1	1.77±0.08	2.31±0.12
ISM 11C2	C-L4834	0.94±0.06	3.51±0.22	1.12±0.01	5±9	0.17±0.02	0.54±0.1	1.79±0.08	2.33±0.12
ISM 14	C-L4847	0.94±0.06	3.46±0.22	1.04±0.01	5±17	0.18±0.02	0.54±0.1	1.72±0.08	2.26±0.12
ISM 17	C-L4844	0.88±0.06	3.28±0.21	0.98±0.01	5±16	0.18±0.02	0.54±0.1	1.63±0.07	2.17±0.12
ISM 19	C-L4840	0.95±0.06	3.63±0.23	1.08±0.01	5±13	0.2±0.02	0.54±0.1	1.79±0.08	2.33±0.12
ISM 21	C-L4839	0.91±0.06	3.48±0.22	0.95±0.01	5±12	0.2±0.02	0.54±0.1	1.64±0.07	2.18±0.12
ISM 23	C-L4841	0.89±0.05	3.09±0.19	0.86±0.01	5±14	0.17±0.02	0.54±0.1	1.49±0.07	2.03±0.12
ISM 24	C-L4842	0.97±0.06	3.5±0.22	0.94±0.01	5±15	0.16±0.02	0.54±0.1	1.62±0.07	2.15±0.12
ISM D1	C-L4849	0.86±0.06	3.01±0.19	1.05±0.01	5±18	0.17±0.02	0.54±0.1	1.66±0.07	2.2±0.12
ISM B1	C-L4850	0.92±0.06	2.97±0.19	1.15±0.01	5±19	0.21±0.02	0.54±0.1	1.81±0.08	2.34±0.12
ISM B2	C-L4851	0.86±0.06	3.01±0.19	1.05±0.01	5±20	0.25±0.03	0.54±0.1	1.69±0.07	2.23±0.12
ISM D2	C-L4852	0.91±0.06	3.22±0.2	1.13±0.01	5±21	0.17±0.02	0.54±0.1	1.77±0.08	2.31±0.12

Table S5. Radiocarbon data of *polychaete* tubes collected.

Field number	Ridge number	Laboratory code	Coordinates (UTM)	Material	Sample Deep (m)	δ13C	^{14}C age and error (^{14}C yr BP)	Delta R and error (yr)	Age Cal yr BP (1σ)
F-5c	11	D-AMS 036521	632152-5901392	*Polychaete* tubes	1.30	-10.6	2887 ± 35	43 ± 52	**2210 - 2668**
F-2-3	17	D-AMS 036520	631664-5902406	*Polychaete* tubes	1.5	-17.4	2773 ± 34	43 ± 52	**2046 – 2489***
F-13	24	D-AMS 036523	632305-5899963	*Polychaete* tubes	1.5 – 1.6	-13.7	4415 ± 28	43 ± 52	**4092 - 4530**

*Excluded from the model

Table S6. Average uplift rate calculated for ridges with absolute ages. Indicative meaning (IM) and modeled relative sea level (ICE6G) are also shown.

Ridge	IRSL (yrs BP)	IRSL error (yrs BP)	Modeled age (yrs BP)	Modeled age sigma (yrs BP)	Elevation (m)	Elevation – tilt (m)	IM (m)	ICE6G (m)	ICE6G Uplift rate (m/kyr)
24	4400	400	4399	254	6.48±0.17	4.84±0.20	2.2 ± 0.1	1.82 ± 0.20	0.19 ± 0.07
23	4500	300	4215	131	6.71±0.15	5.13±0.20	2.2 ± 0.1	1.71 ± 0.17	0.29 ± 0.07
21	3500	300	3377	225	5.47±0.23	3.95±0.23	2.2 ± 0.1	1.34 ± 0.28	0.12 ± 0.1
19	2600	240	3032	286	5.06±0.26	3.62±0.35	2.2 ± 0.1	0.99 ± 0.18	0.14 ± 0.13
17	2600	300	2773	105	5.43±0.15	4.23±0.19	2.2 ± 0.1	0.86 ± 0.18	0.42 ± 0.1
14	2680	170	2589	93	5.98±0.26	4.50±0.33	2.2 ± 0.1	0.80 ± 0.15	0.58 ± 0.15
11	2480	160	2401	79	6.03±0.26	4.86±0.38	2.2 ± 0.1	0.76 ± 0.16	0.79 ± 0.18
6	1800	180	1853	111	5.07±0.15	4.23±0.18	2.2 ± 0.1	0.53 ± 0.10	0.81 ± 0.13
5	1800	130	1733	99	3.85±0.20	3.40±0.46	2.2 ± 0.1	0.48 ± 0.08	0.42 ± 0.28
2	900	70	970	169	3.20±0.10	2.92±0.16	2.2 ± 0.1	0.23 ± 0.10	0.51 ± 0.24

Table S7. Average uplift rate calculated for swales with dating. Indicative meaning (IM) and modeled relative sea level (ICE6G) are also shown.

Swale	IRSL (yrs BP)	IRSL error (yrs BP)	Modeled age (yrs BP)	Modeled age sigma (yrs BP)	Elevation (m)	Elevation - tilt (m)	IM (m)	ICE6G (m)	ICE6G Uplift rate (m/kyr)
24	4400	400	4399	254	5.64±0.15	3.98±0.22	1.3 ± 0.1	1.82 ± 0.20	0.20 ± 0.07
23	4500	300	4215	131	5.93±0.18	4.29±0.20	1.3 ± 0.1	1.71 ± 0.17	0.30 ± 0.07
21	3500	300	3377	225	5.37±0.10	3.95±0.14	1.3 ± 0.1	1.34 ± 0.28	0.39 ± 0.09
19	2600	240	3032	286	5.27±0.22	3.64±0.28	1.3 ± 0.1	0.99 ± 0.18	0.45 ± 0.12
17	2600	300	2773	105	5.19±0.15	3.77±0.17	1.3 ± 0.1	0.86 ± 0.18	0.58 ± 0.1
14	2680	170	2589	93	5.88±0.15	4.49±0.17	1.3 ± 0.1	0.80 ± 0.15	0.92 ± 0.1
11	2480	160	2401	79	4.85±0.06	3.68±0.08	1.3 ± 0.1	0.76 ± 0.16	0.67 ± 0.09
6	1800	180	1853	111	4.72±0.15	3.72±0.34	1.3 ± 0.1	0.53 ± 0.10	1.02 ± 0.21
5	1800	130	1733	99	3.64±0.23	3.14±0.32	1.3 ± 0.1	0.48 ± 0.08	0.78 ± 0.20
2	900	70	970	169	2.95±0.10	2.67±0.12	1.3 ± 0.1	0.23 ± 0.10	1.46 ± 0.32

Supporting Code

Oxcal Code:

```
Options()
 {
  SD1=TRUE;
 };
 Plot()
 {
  Curve("Marine20","marine20.14c");
  Delta_R(43,52);
  Sequence("ISM")
  {
   Boundary("S24")
   {
   };
   Phase("R24")
   {
    R_Date(4415,28);
    Date(N(2019-4540,316));
    Interval("I24");
   };
   Boundary("S23")
   {
   };
   Phase("R23")
   {
    Date(N(2019-4400,400));
    Interval("Ridge 23");
   };
   Boundary("S22")
   {
   };
   Phase("R22")
   {
    Interval("I22");
   };
   Boundary("S21")
   {
   };
   Phase("R21")
   {
    Date(N(2019-3660,218));
    Interval("I21");
   };
   Boundary("S20")
   {
   };
   Phase("R20")
   {
```

```
 Interval("I20");
};
Boundary("S19")
{
};
Phase("R19")
{
 Date(N(2019-2670,170));
 Interval("I19");
};
Boundary("S18")
{
};
Phase("R18")
{
 Interval("I18");
};
Boundary("S17")
{
};
Phase("R17")
{
 Date(N(2019-2650,195));
 Interval("I17");
};
Boundary("S16")
{
};
Phase("R16")
{
 Interval(I16);
};
Boundary("S15")
{
};
Phase("R15")
{
 Interval("I15");
};
Boundary("S14")
{
};
Phase("R14")
{
 Date(N(2019-2680,166));
 Interval("I14");
};
Boundary("S13")
{
};
Phase("R13")
{
```

```
 Interval("I13");
};
Boundary("S12")
{
};
Phase("R12")
{
 Interval("I12");
};
Boundary("S11")
{
};
Phase("R11")
{
 R_Date(2887,35);
 Date(N(2019-2480,164));
 Interval("I11");
};
Boundary("S10")
{
};
Phase("R10")
{
 Interval();
};
Boundary("S9")
{
};
Phase("R9")
{
 Interval("I9");
};
Boundary("S8")
{
};
Phase("R8")
{
 Interval("I8");
};
Boundary("S7")
{
};
Phase("R7")
{
 Interval("I7");
};
Boundary("S6")
{
};
Phase("R6")
{
 Date(N(2019-1880,120));
```

```
 Interval("I6");
};
Boundary("S5")
{
};
Phase("R5")
{
 Date(N(2019-1790,130));
 Interval("I5");
};
Boundary("S4")
{
};
Phase("R4")
{
 Interval("I4");
};
Boundary("S3")
{
};
Phase("R3")
{
 Interval("I3");
};
Boundary("S2")
{
};
Phase("R2")
{
 Date(N(2019-890,73));
 Interval("I2");
};
Boundary("S1")
{
};
Phase("R1")
{
 Interval("I1");
};
Boundary("EQ",2019-449);
};
};
```